In Situ Scattering and Modeling Approaches for the Discovery and Optimization of Novel Mineral-Inspired Materials

A Dissertation Presented

by

William Richard Woerner

to

The Graduate School

in Partial Fulfillment of the

Requirements

for the Degree of

Doctor of Philosophy

in

Geosciences

Stony Brook University

August 2015

Stony Brook University
The Graduate School

William Richard Woerner

We, the dissertation committee for the above candidate for the
Doctor of Philosophy degree, hereby recommend
acceptance of this dissertation.

John B. Parise – Dissertation Advisor
Distinguished Professor, Department of Geosciences & Department of Chemistry

Robert C. Liebermann – Chairperson of Defense
Distinguished Service Professor, Department of Geosciences

Lars Ehm
Research Associate Professor, Department of Geosciences

Timothy D. Glotch
Associate Professor, Department of Geosciences

Paul M. Forster
Assistant Professor, Department of Chemistry
University of Nevada Las Vegas

This dissertation is accepted by the Graduate School

Charles Taber
Dean of the Graduate School

Abstract of the Dissertation

In Situ Scattering and Modeling Approaches for the Discovery and Optimization of Novel Mineral-Inspired Materials

by

William Richard Woerner

Doctor of Philosophy

in

Geosciences

Stony Brook University

2015

Exploratory synthesis, discovery of novel materials, and characterization of the structure – property relationship drives new technologies that might mitigate major global issues such as climate change. Central to these endeavors are the design of new approaches, apparatus, and improvements in existing sample environments, which allow one to observe the evolution of changes in atomic arrangements directly. The new techniques and strategies decrease the materials discovery-deployment cycle (DDC), a central goal of the Materials Genome Initiative (MGI). The strategies developed and described in this dissertation, are broadly applicable to the MGI. However, they are particularly powerful when applied to:

The synthesis and optimization of high-pressure materials, where rank ordering of target compositions, predicting possible structure-types, and *in situ* observation of the reactions during synthesis can reduce the DDC from months to hours. Two novel oxynitride phases in the GaN –

Nb_2O_5 system were discovered utilizing this approach and are related to the minerals rutile (TiO_2) and scruntinyite (α-PbO_2).

The rapid evaluation of potential candidate compounds for post-combustion carbon dioxide capture was optimized by combining X-ray diffraction and differential scanning calorimetry (XRD-DSC) with techniques for simulating humid environments. These measurements mimic the process of removing carbon dioxide from wet flue-gas and were used to screen prominent microporous compounds for carbon capture under realistic conditions.

Finally, new strategies for evaluating the atomic arrangements of minerals and their relation to nanoparticles were developed. An extensive crystallographic investigation of the crystalline mineral akdalaite, the presumed structural analog of the nanomineral ferrihydrite, was undertaken to evaluate the shortcomings of the ferrihydrite structural model. The complete akdalaite structure was characterized for the first time using single crystal X-ray diffraction, powder neutron diffraction, and nuclear magnetic resonance. The akdalaite model compiled from the results confirmed the crystal chemical anomalies in the ferrihydrite structure are indeed real, and not sort comings of the model.

Table of Contents

Structural chemistry of akdalaite, $Al_{10}O_{14}(OH)_2$, the aluminum analogue of ferrihydrite, in its single and polycrystalline forms

List of Figures

Chapter 1

Chapter 2

Chapter 3

Chapter 4

List of Tables

Chapter 2

Chapter 3

Chapter 4

Acknowledgments

Firstly, I would like to acknowledge the support and mentorship of my long suffering advisor, John B. Parise. I am forever grateful for the guidance, direction, and freedom he provided me while I pursued my research interests. I am also grateful for the guidance Siddhartha Mitra provided me during my undergraduate research and for helping me develop a passion for scientific research. I’d also like to acknowledge Bob Liebermann, John Parise, Lars Ehm, Tim Glotch, and Paul Forster for serving on my defense committee and helping improve this dissertation.

I would like to thank all of the collaborators who contributed to the content of this dissertation: Anna Plonka, Xianyin Chen, Debasis Banerjee, H. A. Naveen Dharmagunawardhane, Guang-Rui Qian, Artem R. Oganov, Peter W. Stephens, and Alexander Smirnov, and Brian L. Phillips. A special thanks goes to Hanna Nekvasil and Donald H Lindsley for allowing me to use the Petrology Laboratory throughout my research.

My research would not have been possible without the financial support of the Department of Geoscience, The Research Foundation of New York, and Stony Brook University. I am grateful for the funding I received over the years from the Department of Energy and the National Science Foundation. Additionally I would like to acknowledge the use of the National Synchrotron Light Source at Brookhaven National Laboratory, the Advanced Photon Source at Argonne National Laboratory, and the Spallation Neutron Source at Oak Ridge National Laboratory, and the COMPRES facilities at Stony Brook University and the National Synchrotron Light Source. Finally, I would like to acknowledge my family and friends for their patience and support for all those years.

Chapter 1

Introduction

This dissertation describes the development of techniques and their application to science that will benefit in mitigating environmental changes caused by human activity. Industrialization has had a profound effect on the planet, including anthropogenic emissions responsible for global warming and climate change.[1, 2] The year 2014 was the warmest year in recorded history following the upward trend in average global temperatures and concentration of the greenhouse gas carbon dioxide (Figure 1).[3-7] Figure 2 shows the global distribution of temperature anomalies showing a near uniform increase in average temperatures; North America is a notable exception.[3]

In order to mitigate global climate change, we must transition to clean and sustainable energy sources such as solar, wind, hydroelectric, and alternative fuels while also working to reduce the greenhouse gas emissions from established power plants. Chapter 2 of this thesis focuses on developing methods and compounds capable of photocatalytic water splitting so as to convert water to gaseous hydrogen and oxygen using only solar energy. Chapter 3 involves the development of a new technique for evaluating compounds for post-combustion CO_2 capture and investigating the adsorption performance of prominent microporous compounds under realistic conditions.

Obtaining fossil fuels for energy generation has also had an environmental impact as poor coal and ore mining practices have polluted surface waters with acid mine drainage. The acidic water resulting from the weathering of mine tailings is rich in heavy metals and precipitates sulfide and oxyhydroxide nanominerals under hydrolyzing conditions.[8, 9] The most ubiquitous precipitate of acid mine drainage is the ferric oxyhydroxide nanomineral known as ferrihydrite.[10] The atomic structure of ferrihydrite has been debated for nearly half a century due to the difficulty in studying its nanoparticle structure (< 10 nm).[10-13] The atomic structure of ferrihydrite must be resolved in order to fully understand the role and impact ferrihydrite has in geochemical environments. Chapter 4 addresses the study of the ferrihydrite structure with comprehensive crystallographic evaluation of the aluminum analog mineral akdalaite.

Each chapter begins with a comprehensive introduction on the topic at hand. Additionally, this dissertation was completed with the help of many collaborators who contributed aspects to each chapter. In Chapter 2, the reagent synthesis, high-pressure synthesis, X-ray diffraction, and neutron scattering data collection and analysis was performed by W.R.W. The crystal structure prediction calculations were conducted by Guang-Rui Qian and Artem R. Oganov from the Department of Geosciences at Stony Brook University. The optical analysis was conducted by H. A. Naveen Dharmagunawardhane from the Department of Materials Science and Engineering at Stony Brook University. The analysis of the X-ray diffraction patterns of the high-pressure synthesis experiments was assisted by Peter W. Stephens from the Department of Physics and Astronomy at Stony Brook University.

In Chapter 3, the design and construction of the X-ray diffraction – differential scanning calorimetry (XRD-DSC) gas adsorption system as well as all data analysis was conducted by W.R.W. Anna M. Plonka of the Department of Geosciences and Xianyin Chen of the Department of Chemistry at Stony Brook University synthesized the microporous compounds and assisted in collecting XRD-DSC swing data. The adsorption isotherm data was collected by Debasis Banerjee of the Fundamental Chemical Sciences Directorate at Pacific Northwest National Laboratory.

In Chapter 4, the hydrothermal synthesis, powder X-ray diffraction, powder neutron diffraction, and the high energy X-ray total scattering were conducted by W.R.W. The single crystal X-ray diffraction and analysis was conducted by W.R.W. and Anna M. Plonka of the Department of Geosciences at Stony Brook University. The scanning electron microscopy images were collected by W.R.W and Alex Smirnov of the Department of Earth and Marine Sciences at Dowling College. The nuclear magnetic resonance measurements and analysis was conducted by Brian L. Phillips of the Department of Geosciences at Stony Brook University.

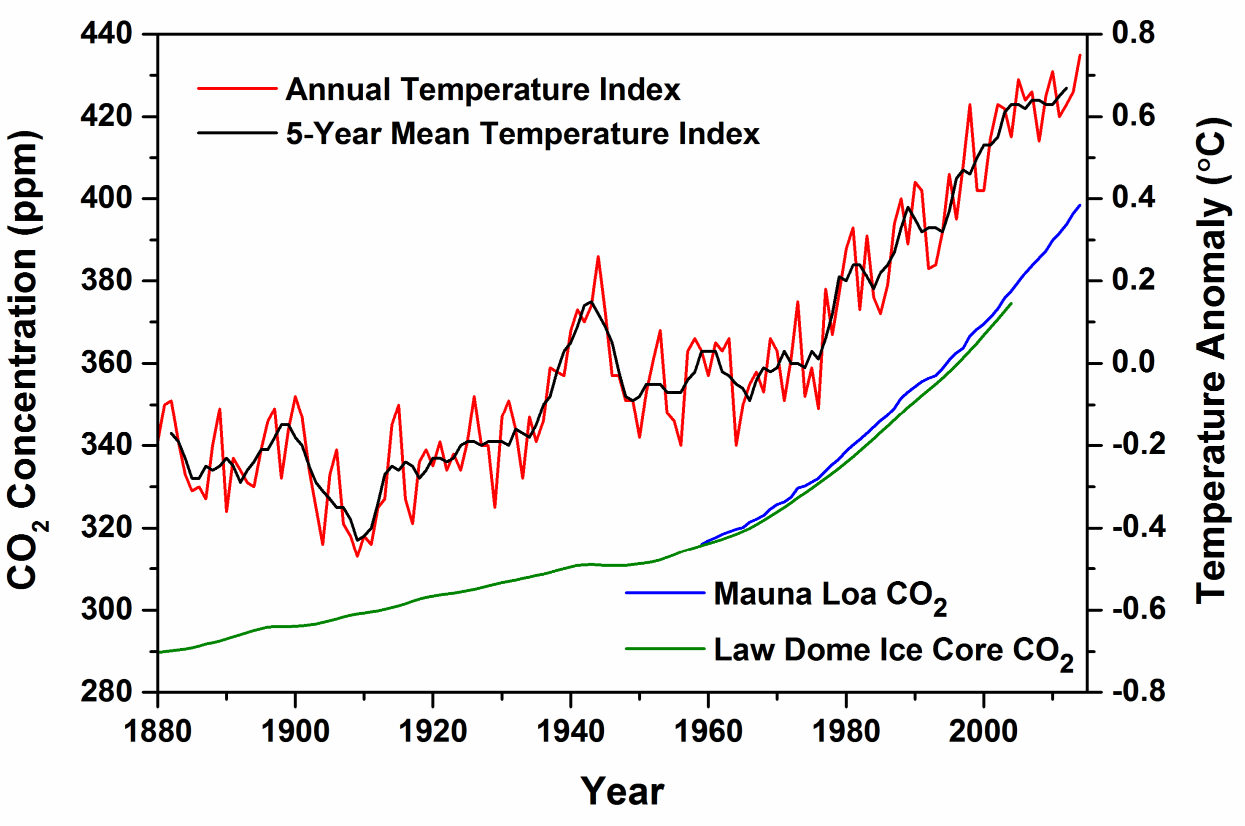

Figure 1. Carbon dioxide concentration measured at the Mauna Loa Observatory (blue) and Law Dome ice core (green) plotted vs. the annual average global temperature (red) and the 5 year running mean of the average global temperature (black). The temperature index is plotted as the deviation from the global average temperature between 1951 and 1980.

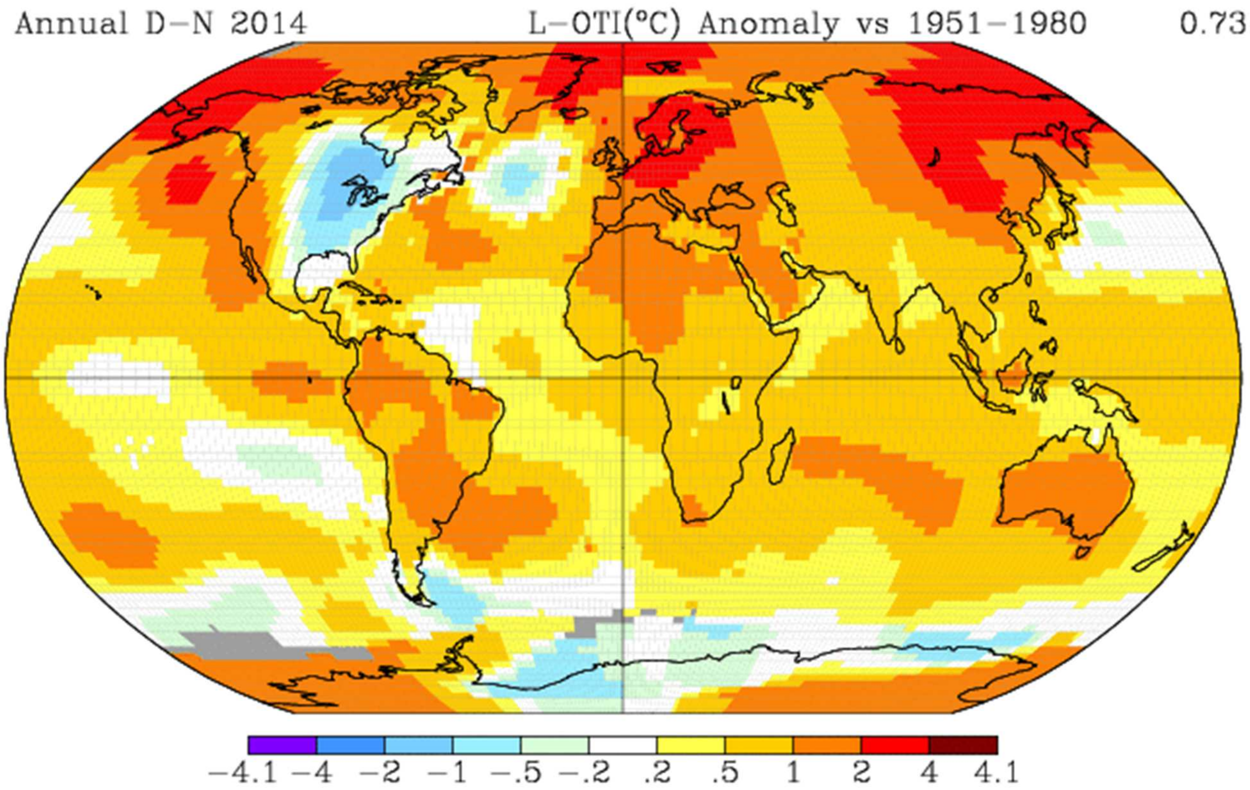

Figure 2. Global temperature anomaly map generated from GISTEMP data. The anomaly temperatures (ºC) are plotted as the deviation from the global average temperature between 1951 and 1980.

References

1. Pachauri, R. K. R., A., IPCC Fourth Assesment Report. In *Intergovernmental Panel on Climate Change*, 2007.

2. Sumida, K.; Rogow, D. L.; Mason, J. A.; McDonald, T. M.; Bloch, E. D.; Herm, Z. R.; Bae, T. H.; Long, J. R., Carbon Dioxide Capture in Metal-Organic Frameworks. *Chemical Reviews* **2012,** 112, (2), 724-781.

3. GISTEMP Team, GISS Surface Temperature Analysis (GISTEMP). **2015**. NASA Goddard Institute for Space Studies. Dataset accessed 2015-05-01 at http://data.giss.nasa.gov/gistemp/.

4. Earth System Research Laboratory. **2015.** http://www.esrl.noaa.gov.

5. Etheridge, D. M.; Steele, L. P.; Langenfelds, R. L.; Francey, R. J.; Barnola, J. M.; Morgan, V. I., Natural and anthropogenic changes in atmospheric CO2 over the last 1000 years from air in Antarctic ice and firn. *Journal of Geophysical Research-Atmospheres* **1996,** 101, (D2), 4115-4128.

6. Etheridge, D. M.; Steele, L. P.; Francey, R. J.; Langenfelds, R. L., Atmospheric methane between 1000 AD and present: Evidence of anthropogenic emissions and climatic variability. *Journal of Geophysical Research-Atmospheres* **1998,** 103, (D13), 15979-15993.

7. Meure, C. M.; Etheridge, D.; Trudinger, C.; Steele, P.; Langenfelds, R.; van Ommen, T.; Smith, A.; Elkins, J., Law Dome CO2, CH4 and N2O ice core records extended to 2000 years BP. *Geophysical Research Letters* **2006,** 33, (14).

8. Furrer, G.; Phillips, B. L.; Ulrich, K. U.; Pothig, R.; Casey, W. H., The origin of aluminum flocs in polluted streams. *Science* **2002,** 297, (5590), 2245-2247.

9. Dold, B., Evolution of Acid Mine Drainage Formation in Sulphidic Mine Tailings. *Minerals* **2014,** 4, (3), 20.

10. Jambor, J. L.; Dutrizac, J. E., Occurrence and constitution of natural and synthetic ferrihydrite, a widespread iron oxyhydroxide. *Chemical Reviews* **1998,** 98, (7), 2549-2585.

11. Michel, F. M.; Barron, V.; Torrent, J.; Morales, M. P.; Serna, C. J.; Boily, J. F.; Liu, Q. S.; Ambrosini, A.; Cismasu, A. C.; Brown, G. E., Ordered ferrimagnetic form of ferrihydrite reveals links among structure, composition, and magnetism. *Proceedings of the National Academy of Sciences of the United States of America* **2010,** 107, (7), 2787-2792.

12. Drits, V. A.; Sakharov, B. A.; Salyn, A. L.; Manceau, A., Structural Model for Ferrihydrite. *Clay Minerals* **1993,** 28, (2), 185-207.

13. Manceau, A.; Skanthakumar, S.; Soderholm, L., PDF analysis of ferrihydrite: Critical assessment of the under-constrained akdalaite model. *American Mineralogist* **2014,** 99, (1), 102-108.

Chapter 2

Combined theoretical and *in situ* scattering strategies for optimized discovery and recovery of high-pressure phases: A case study of the GaN – Nb_2O_5 system

Abstract

The application of pressure in solid-state synthesis provides a route for the creation of new and exciting materials. However, the onerous nature of high-pressure techniques limits their utility in materials discovery. Although, in selected cases high-pressure synthesis has distinct advantages, especially when pressure confinement is used to control stoichiometry and to stabilize reactants prior to reaction, and to prevent decomposition of mixed anion compounds. The systematic search for novel oxynitrides - semiconductors with potential for photocatalytic overall water splitting - is a representative case where HP synthesis may be useful. However, the critical bottleneck remains the slow throughput for most high-pressure approaches to synthesis. We utilize state of the art crystal structure prediction theory, and *in situ* synchrotron-based X-ray scattering to speed up the discovery and optimization phases of HP synthesis. Using this approach, two novel oxynitride phases were discovered in the GaN – Nb_2O_5 system. The $Nb_{1.412}Ga_{0.583}O_{3.412}N_{0.588}$ rutile structured phase was formed at 1 GPa and 900°C and gradually transformed to a PbO_2 structure above 2.8 GPa and 1000°C. The low-pressure rutile type phase was found to have a direct optical band gap 0.84 eV of and an indirect gap of 0.51 eV.

Introduction

High-pressure (HP) synthesis is underutilized relative to exploratory solid-state chemical synthesis at ambient pressure.[1, 2, 3] Despite its perceived specialist nature, “pressure tuning”[4] along with serendipitous[5] and theory-guided strategies,[6] provide exciting avenues for the discovery of novel solid-state materials at high pressures. The specialized infrastructure that is required however, along with the slow throughput implied by the need to perform individual quench experiments to explore high-pressure and high-temperature (HPHT) phase space, conspire to limit the use of HPHT exploratory synthesis.[3] Exhaustive coverage of pressure-temperature (P-T) space requires months of work using “cook-and-look” quench recovery tactics. On the other hand, recent successes in producing novel materials inspired by theory[7-12] suggest collaborations employing crystal structure prediction, particularly when combined with *in situ* observation of reactions at synchrotron and neutron sources,[11, 13] will facilitate HP materials discovery in the future.

The problem of crystal structure prediction is central to rational design of functional materials, and is amongst the most complex problems in solid-state inorganic chemistry. Commentary on this problem has ranged from labeling it a "scandal”,[14] to the somewhat more helpful suggestion that, although we cannot not as yet proceed *ab Initio* from desired property to functional material, we can proceed incrementally toward this goal.[15] In the three decades since such commentaries, there has been sustained and fruitful progress in computational materials discovery, which include fully non-empirical global optimization searches, such as employed by the USPEX method,[10, 16] and data mining techniques.[17-19] These two approaches are quite complementary, especially in the case of ambient pressure synthesis. However, strategies relying on database searching and algorithms for substituting anion and cations into known structures are of a more limited utility when applied to potential high-pressure phases as empirical knowledge is sparse and HP chemistry can be very different from that at ambient conditions.[1, 6, 18] The *ab initio* evolutionary algorithm embodied in the USPEX method, on the other hand, is computationally more expensive, but can be applied without depending on the availability of pre-existing empirical knowledge, and therefore is capable of predicting totally new and unexpected crystal structures and chemical compositions.

Oxynitrides: Anticipated Advantages of High-Pressure Synthesis

Oxynitride compounds have shown a wide array of properties and applications, which include pigments, dielectrics, magnetoresitance, and photocatalysis.[20] Oxynitrides of d^{10} and d^0 cations have garnered significant interest in recent years due to their potential to act as overall visible light water splitting photocatalysts.[21] Water splitting photocatalysts need to have conduction and valence band positions that straddle the water reduction and oxidation potentials (1.23 V), a band gap small enough to absorb in the solar spectrum, and be stable during the reaction.[21, 22] Oxynitrides are desirable as photocatalysts since they typically have narrower band gaps than respective oxides while having higher air stability and corrosion resistance as compared to nitrides.[21, 22] The most notable and efficient system being the GaN – ZnO solid solution, which has shown the ability split water under visible light irradiation with a quantum efficiency of 5.9%.[23] But as the efficiency of known photocatalysts have yet to reach levels of commercial viability, research is focused on discovering new materials.

Typically, oxynitrides are synthesized via the ammonolysis of oxides at ambient pressure; but not all oxides will react at the moderate temperatures used during ammonolysis. The application of HP provides a route for direct solid-state oxynitride synthesis using oxide and nitride reagents as pressure suppresses the decomposition of the nitride at high temperatures. Surprisingly, there are few examples of oxynitrides synthesized using HP methods. Examples of successful recovery experiments include $BaNbO_2N$, La_2AO_3N (A = Al, Nb, Ti, V) oxynitrides synthesized at 5 GPa[24], $RZrO_2N$ (R = Pr, Nd, Sm) synthesized at 2-3 GPa,[25] the spinel structured Ga_3O_3N at pressures between 1 and 5 GPa [26], [27], [28], [29], the wurtzite structured GaN – ZnO solid solution at pressures between 1.7 and 6.2 GPa,[30] moganite-type PON prepared at 2.5 GPa[31] and δ-PON prepared at 12.5 GPa.[32] High-pressure synthesis is an underutilized tool in oxynitride synthesis and maybe an important complement to the accessible ammonolysis route.

Using Crystal Structure Prediction to Guide Oxynitride Synthesis

The USPEX approach has had great success in predicting HP phases that were subsequently confirmed experimentally.[11, 12, 33-35] The current version (9.4.2) of USPEX features HP variable composition structure prediction that utilizes the mixing of end member chemistries.[9] This approach has been used to investigate the stability of new stoichiometries in the systems of Fe - C, Fe – H, [36] Hf – C, [37] Na – Cl,[6] Xe – O,[38] Mg – O,[39] W –B,[40, 41] and HfO_2 – SiO_2.[42] Experimental results confirmed the existence of the predicted $NaCl_3$ and Na_3Cl phases[6] as well as WB_3 and WB_{3+x} phases.[40]

Accurate structure prediction using USPEX presents some challenges for HP oxynitride compounds. As nitrogen and oxygen have similar ionic size, coordination numbers, polarizability, and electronegativity, these anions can disorder across anion sites.[20] While some oxynitride compounds exhibit partial ordering,[43, 44-47] ideally ordered oxynitrides are rarely encountered and include the only natural mineral oxynitride sinoite (Si_2N_2O) [48, 49] and the TaON photocatalyst.[50] UPSEX performs 0 K calculations only on ordered structures as occupational disorder would increase computation cost by several orders of magnitude. As a consequence, if performing calculations using atoms that can easily disorder (i.e. N^{3-} and O^{2-}), disordered stable compounds will likely have a lower enthalpy of formation than any ordered compound that could be predicted by USPEX. With calculations preformed at 0 K to reduce computational cost, a consequence is the lower pressure stability limit can be significantly overestimated, often by > 10 GPa. USPEX does however provide a useful guide, identifying compositions likely to lead to thermodynamically stable structures.

Herein, we describe a method combining theoretical and experimental techniques to allow for more efficient discovery of novel materials at high-pressures. In order to ameliorate the major problems with HP-materials discovery and sample optimization, we developed new approaches that combine modern computational tools, *in situ* observation of reactions with X-ray diffraction while varying P-T, and structural characterization. To test these approaches, we choose to focus on the formation of novel d^0/d^{10} mixed oxynitrides in the GaN – Nb_2O_5 system as the system has the potential to form compounds with photocatalytic properties.

Experimental

USPEX Calculations

Using the evolutionary algorithm as implemented in USPEX[51-53] a variable composition search was implemented to generate a range of compounds with chemical compositions chosen at random from a mixing of GaN and Nb_2O_5 endmembers. The underlying *ab initio* structure relaxation and electronic structure calculations were carried out using the all electron projected augmented wave (PAW) method[54] as implemented in the Vienna ab-initio simulation package (VASP)[55]. The Perdew-Burke-Ernzerhof (PBE) functional was used to treat the exchange-correlation energy.[56] A plane-wave kinetic cutoff energy of 600 eV was used in addition to reciprocal space sampling with dense Monkhorst-Pack k-point meshes[57] at a resolution of 2π x

0.05 $Å^{-1}$ in order to provide sufficient accuracy during enthalpy calculations.

GaN Synthesis

The GaN used for this investigation was synthesized in house via the ammonolysis of Ga_2O_3 to ensure phase purity. A 2 g sample of Ga_2O_3 (99.99%, Sigma-Aldrich) was loaded into a quartz boat and placed in a sealed 1 inch diameter tube furnace. The atmosphere was evacuated to rough vacuum and then filled to 1 bar of pressure with ammonia gas. The Ga_2O_3 reacted with the ammonia flowing at a rate of 500 mL/min at 950°C for 2 hours. The product was cooled back to room temperature under flowing ammonia and was then removed, ground for 10 min in an agate mortar and pestle, and then subjected to the reactions conditions described above for a second time. X-ray diffraction (XRD) of the recovered pale yellow powder revealed it consisted of nanocrystalline wurtzite-type GaN with no traces of Ga_2O_3.

In situ HPHT XRD Investigation

The HPHT reaction between GaN – Nb_2O_5 was studied *in situ* at pressures and temperatures up to 3.8 GPa and 1200°C using energy dispersive XRD (EDXRD) at the X17B2 beamline at the National Synchrotron Light Source (NSLS). A 1:1 mix of GaN and Nb_2O_5 (99.99%, Sigma-Aldrich) was mechanically ground in an agate mortar and pestle for 45 minutes and loaded into a BN sleeve. The mix was stacked on top of an MgO internal pressure standard and physically separated with a layer of BN. The sleeve was inserted into a boron epoxy cubic DIA cell with a resistive heating graphite furnace and a W-3%Re/W-28%Re thermocouple (Figure 4). The cell was compressed using a 1000 ton multi-anvil press (BAM11) and the EDXRD patterns were collected using a white beam (14-120 keV X-rays) incident on tungsten slits to produce a 100 μm x 100 μm beam. The cell was first compressed to a press loading of 15 tons (~1 GPa) and the temperature was raised to 1000°C with EDXRD patterns collected every 100°C with 300 s exposure after a 1000 s reaction time. The cell was then cooled to room temperature, followed by an increase in pressure to 25 tons. The temperature was then raised in 100°C increments to 1200°C with the same EDXRD data collection strategy described above employed at the end of each increment with the process again repeated at 35 tons.

HPHT Piston Cylinder Quench Experiments

HPHT reactions between GaN and Nb_2O_5 were carried out *ex situ* using a piston cylinder apparatus at P-T points selected according to the phase stability fields determined from the *in situ* EDXRD results. For the 1 GPa experiment, a 19 mm (0.75 inch) diameter piston cylinder setup was used to maximize the sample volume. Approximately 1 g of the GaN – Nb_2O_5 mix was loaded in a graphite furnace and encapsulated within the cylinder with two BN disks. The sample was centered in the furnace using two pyrophyllite plugs that were previously fired at 1000°C for 20 minutes. The temperature was monitored with a Pt/Pt_{90}-Rh_{10} thermocouple pressed against the BN disk just above the sample in the talc cell assembly (Figure 1). The entire assembly was cold compressed to the desired pressure and ramped up to temperature while holding the pressure constant. The experiments were left to react for 1 hour and then quenched isobarically. For the 3 GPa quench experiment, a 12.7 mm (0.5 inch) diameter piston cylinder assembly was used, as the 19 mm diameter assembly could not reach such high pressures. The 12.7 mm diameter cell assembly is a scaled down version of what is shown in Figure 4, with a substitution of alumina for pyrophyllite plugs. However, only about 50-100 mg of the mix can be loaded in such an assembly. After decompression, the sample pellets were removed from the assembly and physically cleaned to remove any contamination from the cell assembly before grinding.

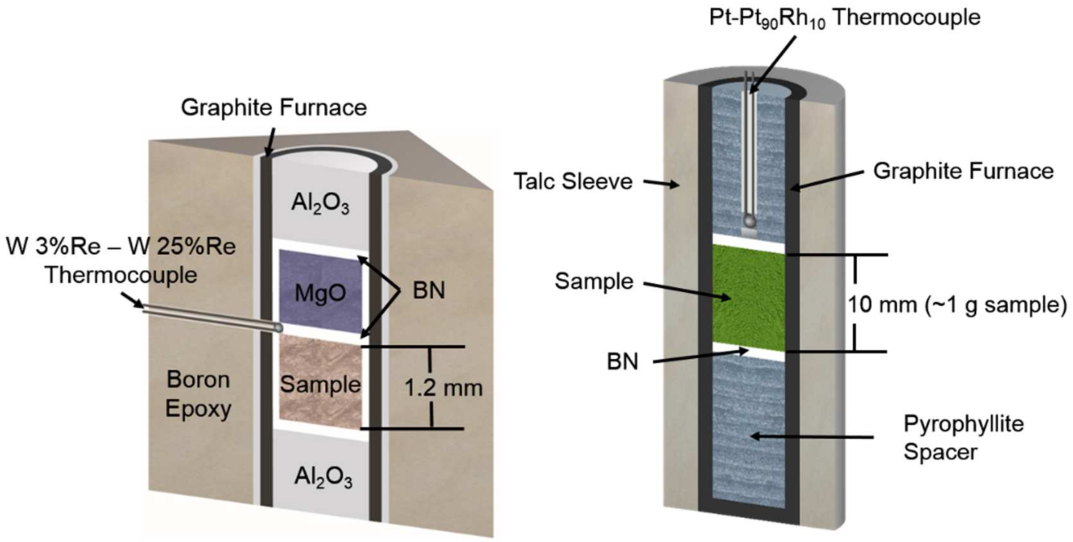

Figure 1. Cross section of the cubic cell assembly (left) used at the X17B2 beamline at NSLS and the 19 mm diameter piston cylinder cell assembly (right). The cubic assembly measures 6.35 mm on each side and the overall length of the piston cylinder assembly is 4.45 cm.

Analytical Methods

The quenched samples were initially characterized with powder XRD using a Rigaku Ultima IV (CuKα) with a D/Tex linear position sensitive detector. After phase identification and comparison with *in situ* EDXRD patterns, the crystalline powders were structurally characterized using synchrotron high resolution XRD and the 1 GPa sample was additionally investigated with time-of-flight (TOF) powder neutron diffraction. High-resolution powder XRD investigations were carried out at the 11-BM beamline at the Advanced Photon Source. The high-resolution XRD patterns were collected with a wavelength of 0.41383(1) Å at room temperature while the samples were spun on a goniometer in a kapton capillary. The patterns were collected over an angular range of $0.8° \leq 2\theta \leq 49.99°$ with a step size of 0.001°. The TOF powder neutron diffraction experiment was conducted using the POWGEN instrument (BL-11) at the Spallation Neutron Source. Approximately 1g of sample was loaded into a 6 mm vanadium can and data were collected using frames 1 and 5 (chopper wavelength centered at 0.533 and 3.731 Å respectively) giving access to a range of $0.25 \text{ Å} \leq d \leq 6 \text{ Å}$. Diffuse reflectance spectra were collected using an ASD Fieldspec3 Mac UV-VIS-NIR spectrometer with an Ocean Optics HL-2000-HP tungsten halogen light source.

Results

$GaN–Nb_2O_5$ USPEX Calculations

Variable composition structure prediction calculations in the $(GaN)_x – (Nb_2O_5)_y$ system were performed at 0 and 20 GPa to evaluate the stability of oxynitride compounds encountered. While the commercial zone of high-pressure is most desirable (<6 GPa) for potential in scale-up production, the calculations need to be conducted at a significant overpressure to compensate for the 0 K temperature of the calculations. At 0 GPa, the calculations indicate all of the predicted compounds are unstable and decomposition into the endmembers wurtzite GaN and R-Nb_2O_5 is energetically favored (Figure 2). However, calculations at 20 GPa indicate a stable oxynitride with a composition of $GaNb_2O_5N$ as the enthalpy of formation is lower than that of the end members wurtzite GaN and Z-Nb_2O_5 (Figure 3). The structure of the predicted ordered $GaNb_2O_5N$ phase is shown in Figure 4. The 20 GPa calculations indicate a high probability of a reaction occurring at HP, although the predicted structure did not match that of either of the oxynitride phases found in the HPHT experiments, described below.

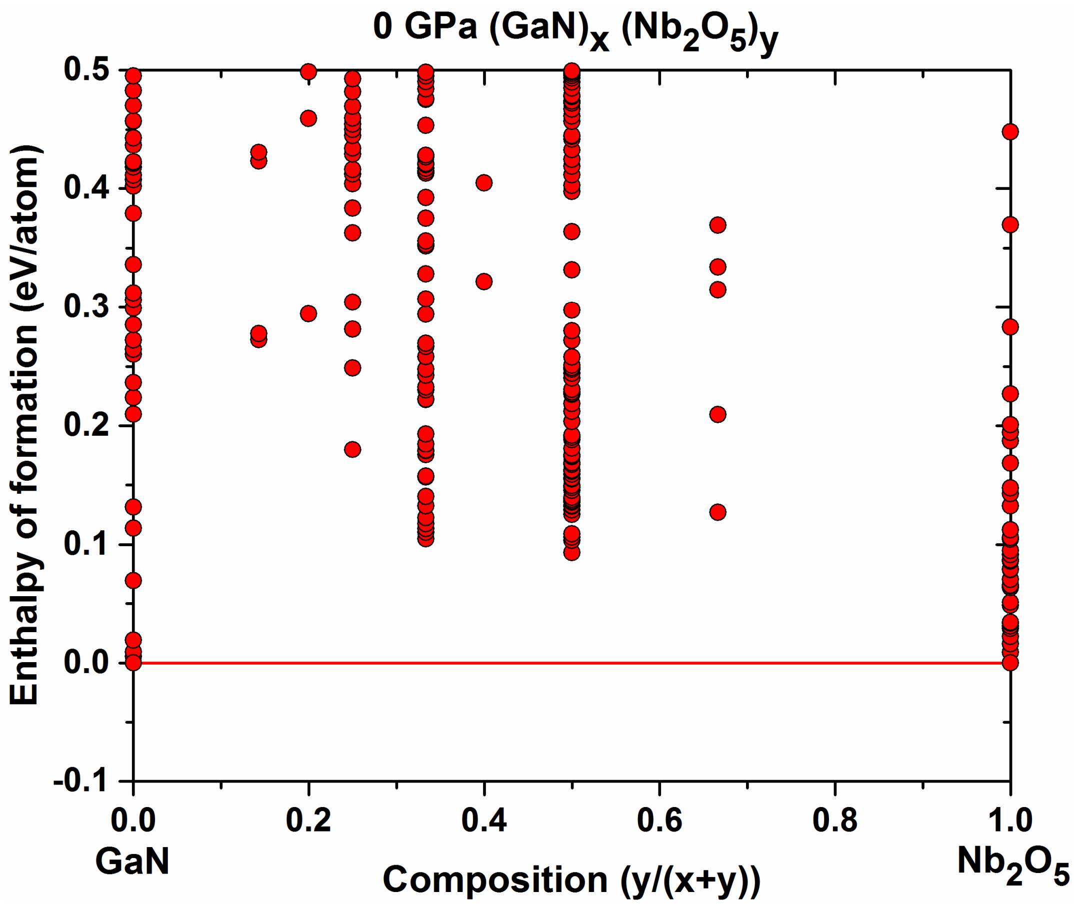

Figure 2. Predicted formation enthalpy diagram for GaN – Nb_2O_5 compounds at ambient pressure. The circles represent individual structures and are plotted as compositions versus enthalpies of formation.

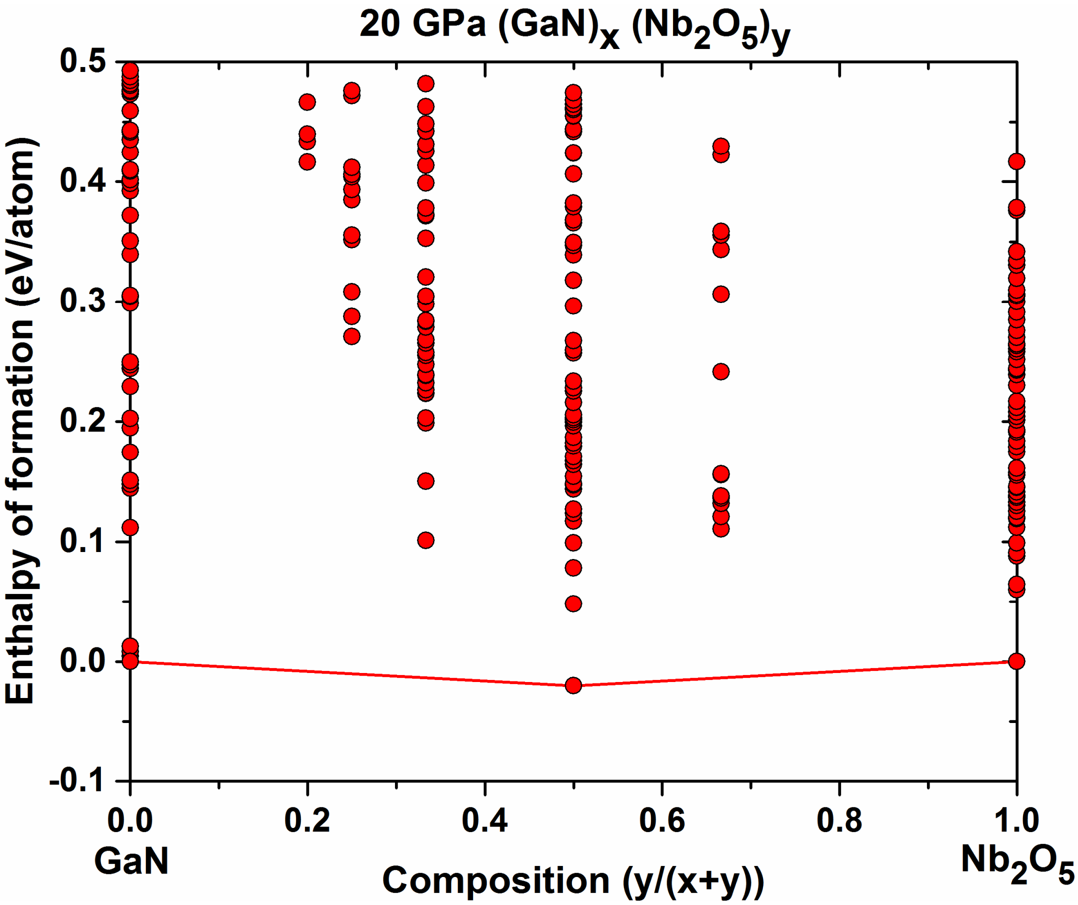

Figure 3. Predicted formation enthalpy diagram for GaN – Nb_2O_5 compounds at 20 GPa. The circles represent individual structures and are plotted as compositions versus enthalpies of formation.

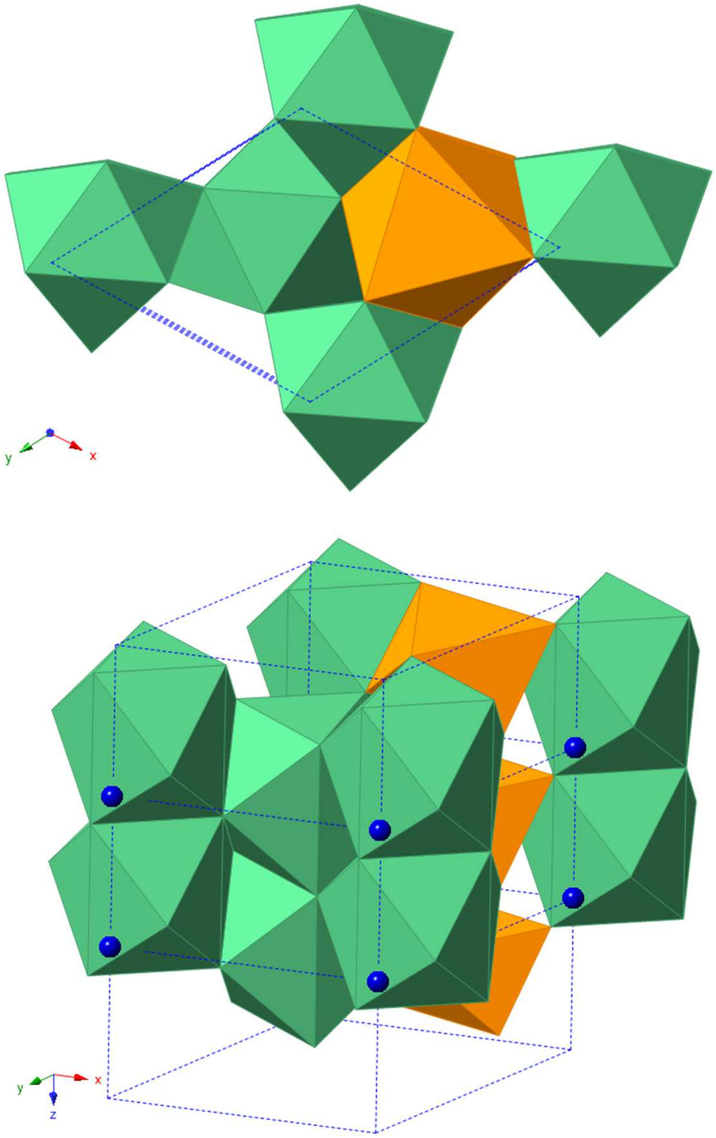

Figure 4. Lowest energy $GaNb_2O_5N$ structure predicted to be stable at 20 GPa. Gallium (orange) is coordinated by 6 oxygen atoms in a distorted octahedra while niobium (green) is coordinated by 7 oxygen atoms and 2 nitrogen atoms in a tricapped trigonal prism geometry. Unit cell is outlined with dashed blue line.

HPHT GaN

The GaN starting material used for the both the HPHT *in situ* XRD and the quench experiments was also subjected to HPHT conditions to understand its behavior under the reaction conditions. The GaN starting material was subjected to all of the same pressures and temperatures as the GaN-Nb_2O_5 quench experiments and in each case, a minor β-Ga_2O_3 phase crystallized in addition to the major wurtzite GaN phase (Figure 5). While not present in the starting pattern of GaN, β-Ga_2O_3 appears as a minor phase after HPHT treatment. It is likely the starting GaN is not chemically pure and contains either structural oxygen or has an amorphous oxide surface coating that crystallizes at HPHT. These quench experiments showed a Ga_2O_3 oxide component would be involved in each oxynitride synthesis experiment as it phase segregates from GaN reagent.

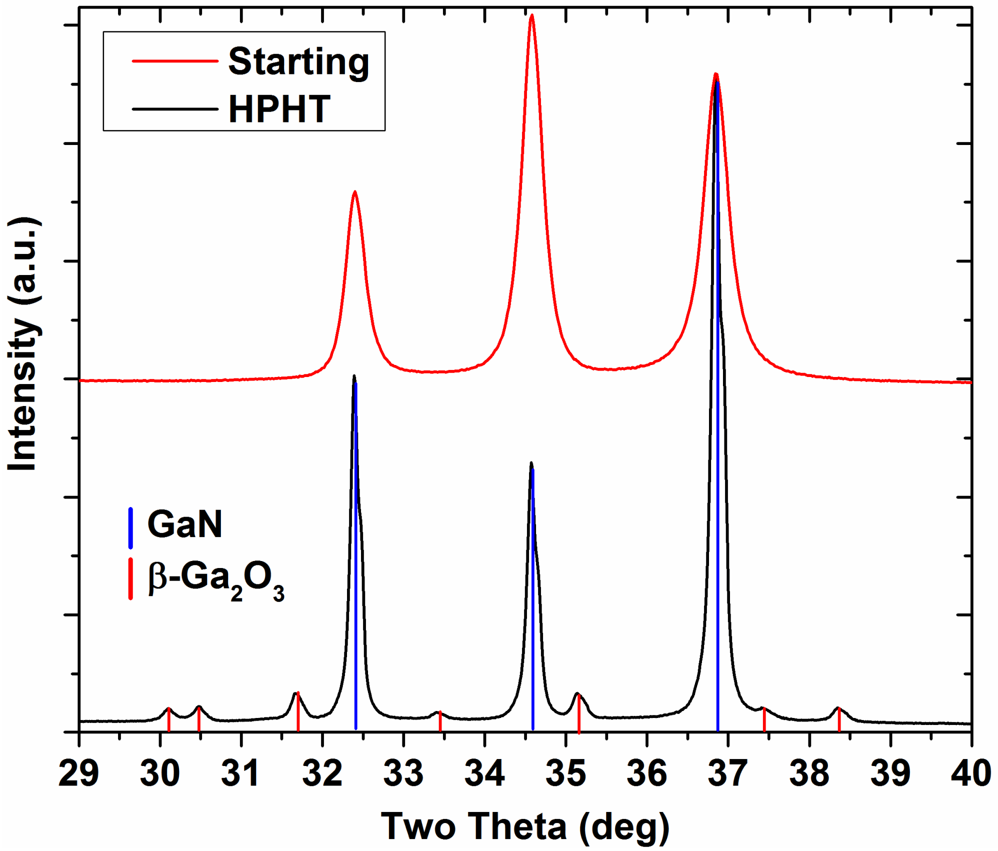

Figure 5. Angle dispersive powder XRD patterns (CuKα) of GaN made via ammonolysis (red pattern) and the same GaN after HPHT treatment at 1 GPa and 1000°C for 1 hour (blue pattern) using the piston cylinder apparatus. Wurtzite GaN reflection markers are in blue and β-Ga_2O_3 are red.

In situ HPHT EDXRD

The EDXRD results of the *in situ* HPHT reaction study conducted at the X17B2 beamline at the National Synchrotron Light Source are summarized in Figures 6, 7, and 8. At approximately 1 GPa, we observe the onset of a reaction between GaN and Nb_2O_5 at 800°C as noted by a complete restructuring of the XRD pattern and a diminishment of the (101) GaN reflection (Figure 6); the reaction is complete by 1000°C. The new Ga – Nb oxynitride observed at ~ 1 GPa has major reflections in the EDXRD patterns at approximately 1.74 and 1.64 Å, consistent with a rutile type (TiO_2) structure (described below). At ~ 2.8 GPa and 900°C, the intensity of peaks attributed to the rutile type phase begin to diminish as new reflections belonging to a PbO_2 type structure appear, indicative of a phase transition (Figure 7). Moreover, as the sample temperature is increased past 800°C at 3 – 4 GPa, the phase transition continues with an increasing intensity of the PbO_2 reflections but without the complete disappearance of reflections attributable to the rutile type phase (Figure 8).

The EDXRD patterns of the *in situ* HPHT investigation revealed two novel oxynitride phases exist in the GaN – Nb_2O_5 system below 3.8 GPa and 1200°C. The EDXRD patterns indicate the optimal conditions for the quench synthesis of the rutile and PbO_2 type phases are 1 GPa and 1000°C, and 3.8 GPa and 1200°C, respectively. As the piston-cylinder apparatus is limited to $P \leq 3$ GPa, the quench experiment targeting the PbO_2 phase was conducted at 3 GPa and 1200°C in order to maximize the amount of this phase in the sample.

The *in situ* studies of the GaN – Nb_2O_5 reaction mapped phase stability in P-T space and provided the optimal reaction temperatures for synthesis, thereby limiting the number of quench experiments required to recover the high-pressure phases to two. This represents a considerably higher success rate than could be realized from the use of single P-T quench exploratory synthesis.

Multi-anvil press assemblies at user facilities offer fast and extensive evaluation of reactions at industrially viable pressures and temperatures. Cell assemblies can also be made to house two different reactions with a pressure calibrant to speed up P-T exploration even further. With this experimental setup, two chemical systems can be evaluated up to modest pressures and temperatures (~5 GPa and 1500°C) in a period of 24 hours. The alternative process of conducting several quench-recovery experiments followed by the characterization of recovered phases to map P-T space could require weeks or months of work.

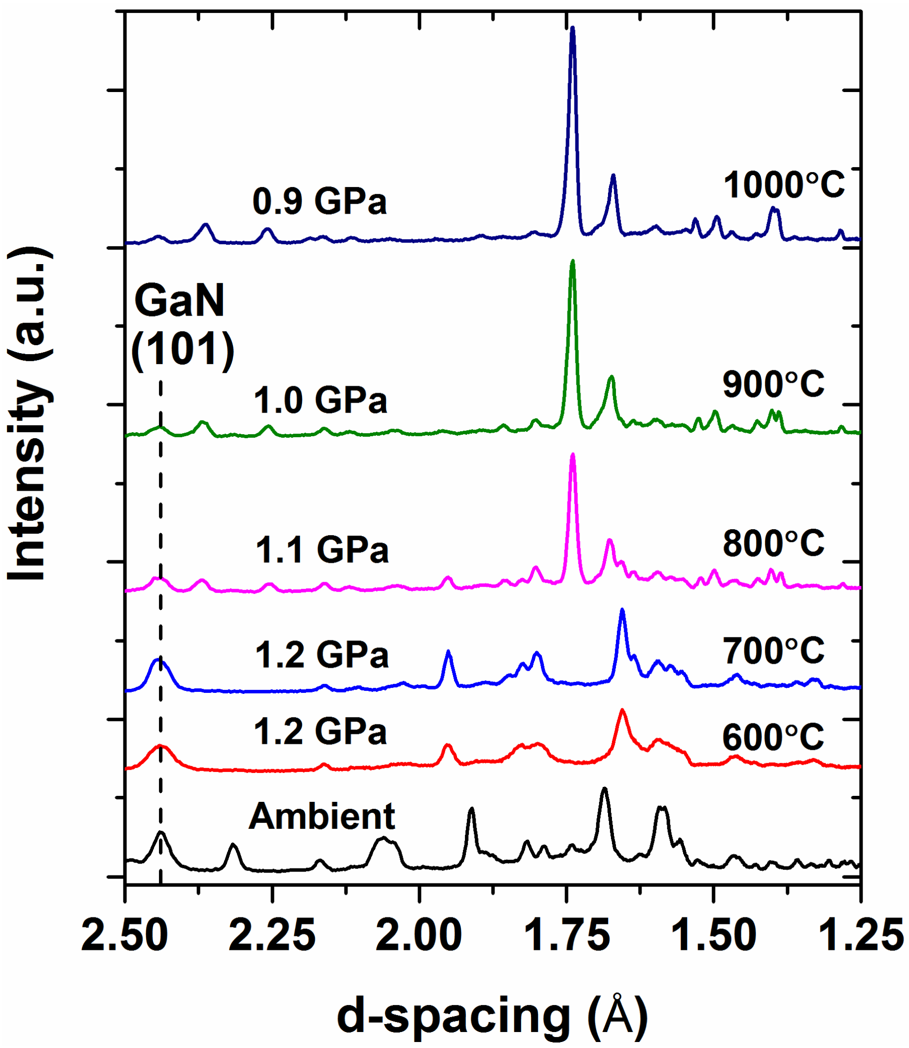

Figure 6. *In situ* EDXRD patterns of a 1:1 mixture of GaN and Nb_2O_5 at a constant press loading of 15 tons. The EDXRD pattern of the initial GaN:Nb_2O_5 mixture at ambient pressure and temperature is at the bottom of the figure in black and contains peaks attributed to only wurtzite-type GaN and monoclinic Nb_2O_5. Upon pressing the sample to 1.2 GPa and heating to 600°C and 700°C, the Nb_2O_5 underwent a phase transformation to the orthorhombic phase but did not react. At ~800°C however, the XRD pattern undergoes a drastic change indicative of a reaction, highlighted by the decrease in intensity for the major GaN (101) refection as the rutile structured oxynitride phase forms. The reaction is essentially complete by 1000°C, with only minor GaN left unreacted.

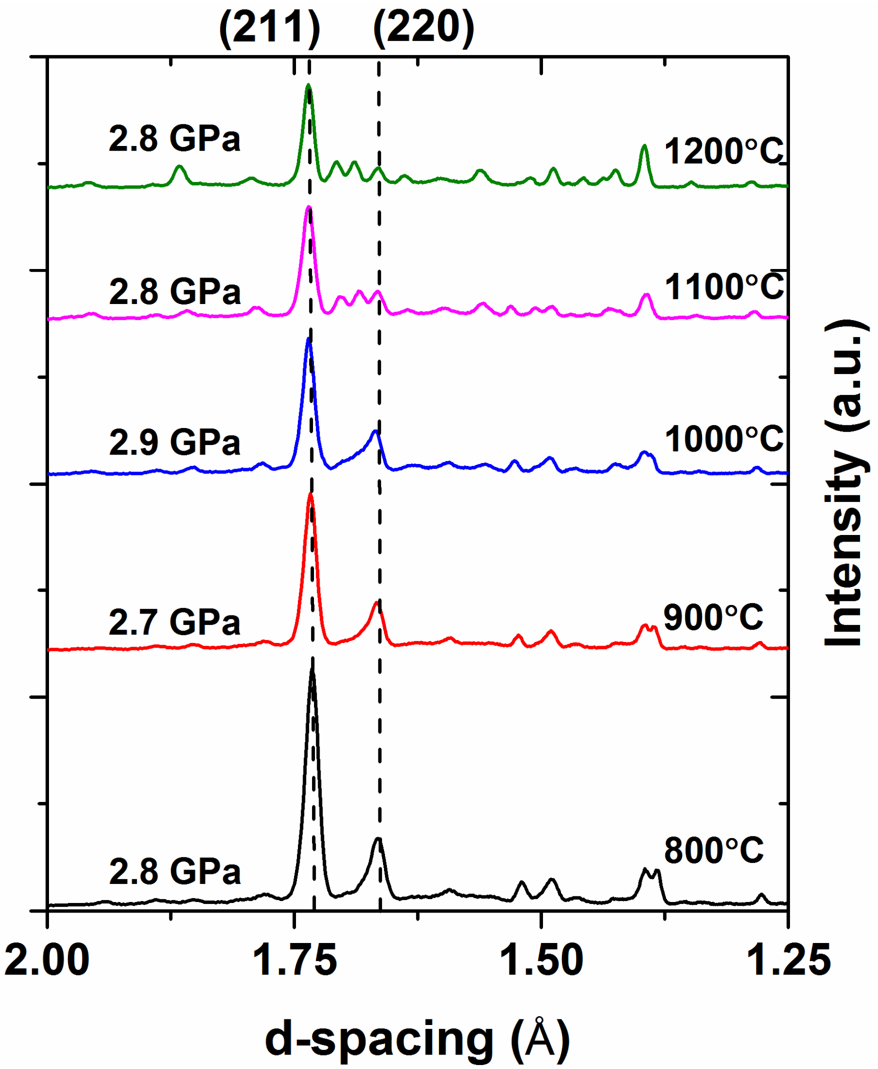

Figure 7. *In situ* EDXRD patterns of GaN – Nb_2O_5 reaction at a constant press loading of 25 tons. The rutile oxynitride phase remains the only Ga-Nb oxynitride phase in the pattern as the sample is heated to 800°C. At 900°C, the intensity of the rutile type (211) and (220) reflections begin decreasing and new peaks in the pattern are apparent by 1200°C, belonging to the new PbO_2 type oxynitride phase.

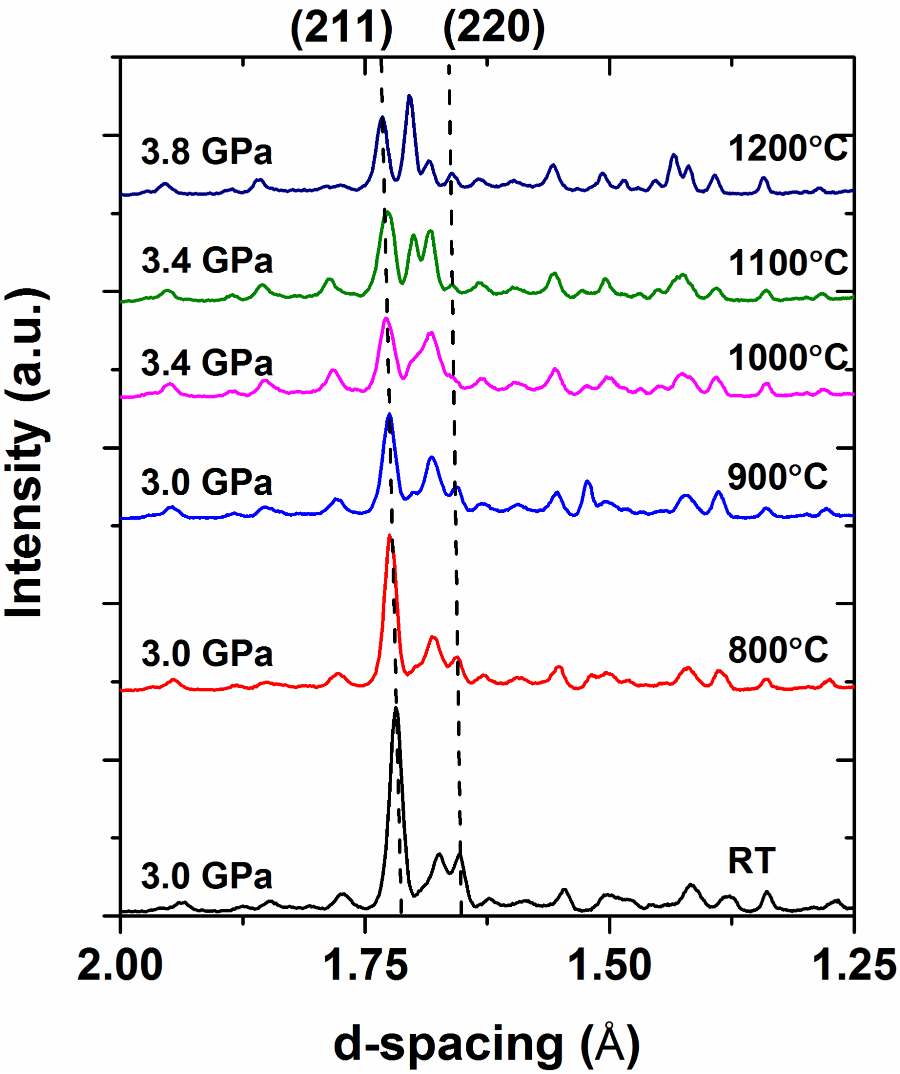

Figure 8. *In situ* EDXRD patterns of GaN – Nb_2O_5 reaction at a constant press loading of 35 tons. Following the trend at 25 tons, as the temperature is increased, we see a decrease in the intensity of the rutile type phase (211) and (220) reflection and the new peaks belonging to the PbO_2 type phase increase in intensity through 1200°C.

Structural Characterization

1 GPa - 1000°C

The product of the 1 GPa - 1000°C quench experiment was evaluated with both high-resolution XRD and TOF powder neutron diffraction. After known phases were identified, the new oxynitride phase in the XRD pattern was indexed, its crystal structure solved, and a Rietveld refinement conducted with the program TOPAS (v4.1, Bruker AXS). The major phase is a new oxynitride found to have the rutile structure with minor GaN, $GaNbO_4$, and T-Nb_2O_5 also identified in the sample (Figure 9). Because of the large X-ray scattering contrast between Nb^{5+} and Ga^{3+}, The occupancies of Nb^{5+} and Ga^{3+} on the single metal site were refined, with the constraint that the total occupancy of the site is 1.0.

The X-ray scattering contrast between O^{2-} and N^{3-} on the other hand is small, and so neutron diffraction data were collected on the same sample as the neutron scattering contrast is high (b_O = 5.803 fm; b_N = 9.36 fm) and can resolve the O/N occupancy and any possible ordering on the anion site. A structure model was refined using two TOF frames and the GSAS/EXPGUI Rietveld software package (Figure 10).[58, 59] As Nb^{5+} and Ga^{3+} have nearly identical neutron scattering lengths (b_{Nb} = 7.054 fm; b_{Ga} = 7.288 fm), the rutile type metal site was fixed to the ratio determined from the XRD refinement. The occupancy of O^{2-} and N^{3-} on the anion site were allowed to freely refine (constrained to add to 1). Using the refined occupancies on both the cation and anion sites, the chemical formula for the rutile related phase is $Nb_{1.412}\ Ga_{0.583}\ O_{3.412}\ N_{0.588}$ which can be nominally represented as $Nb_2O_5(GaN)_{0.83}$. The refinement details and crystallographic data for the rutile relate phase is given in Table 1 (X-ray) and Table 2 (TOF neutron). The content of the Ga^{3+} and N^{3-} show excellent agreement between the two independent X-ray and neutron refinements indicating GaN directly reacts with Nb_2O_5 and the Ga_2O_3 component is ignored. A joint X-ray/neutron refinement was attempted using GSAS/EXPGUI but the X-ray profile parameters could not model the peak shape well enough to carry out a stable refinement. The crystal structure of the rutile type phase is shown in comparison to the PbO_2 type in Figure 12. Structural details and selected bond lengths of both phases can be found in Table 3 and 4, respectively.

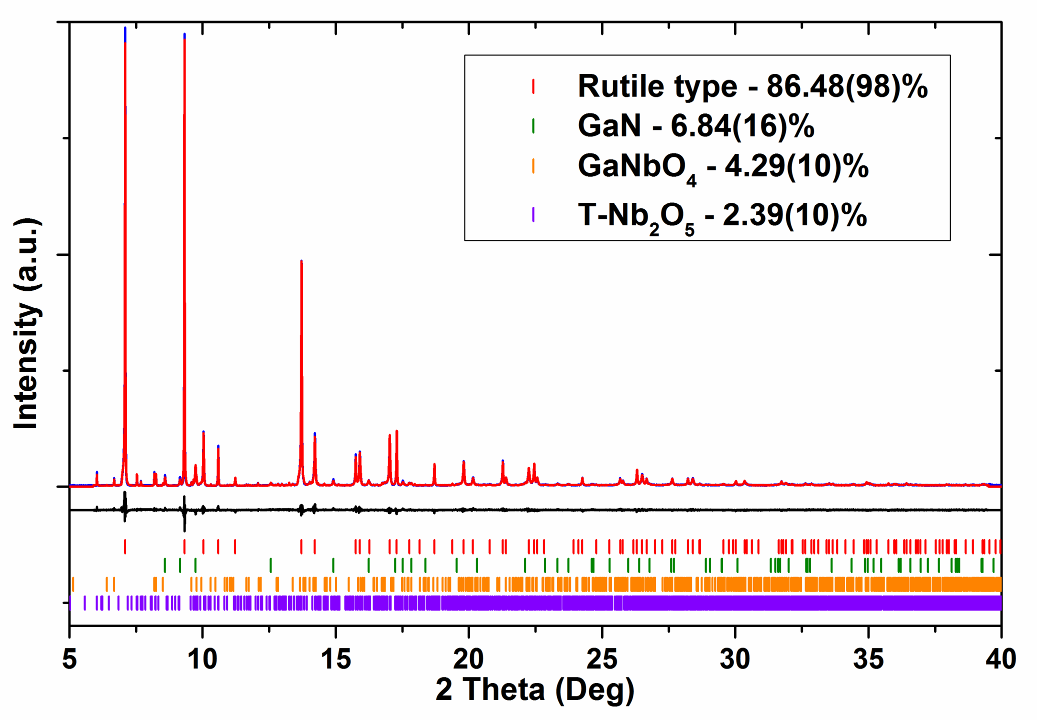

Figure 9. XRD Rietveld refinement result of the 1 GPa - 1000°C synthesis. The collected pattern is shown in blue, the calculated pattern in red, and the difference in black. The tick marks show the positions of reflections of the respective phases. Phase fractions are shown in weight percentages.

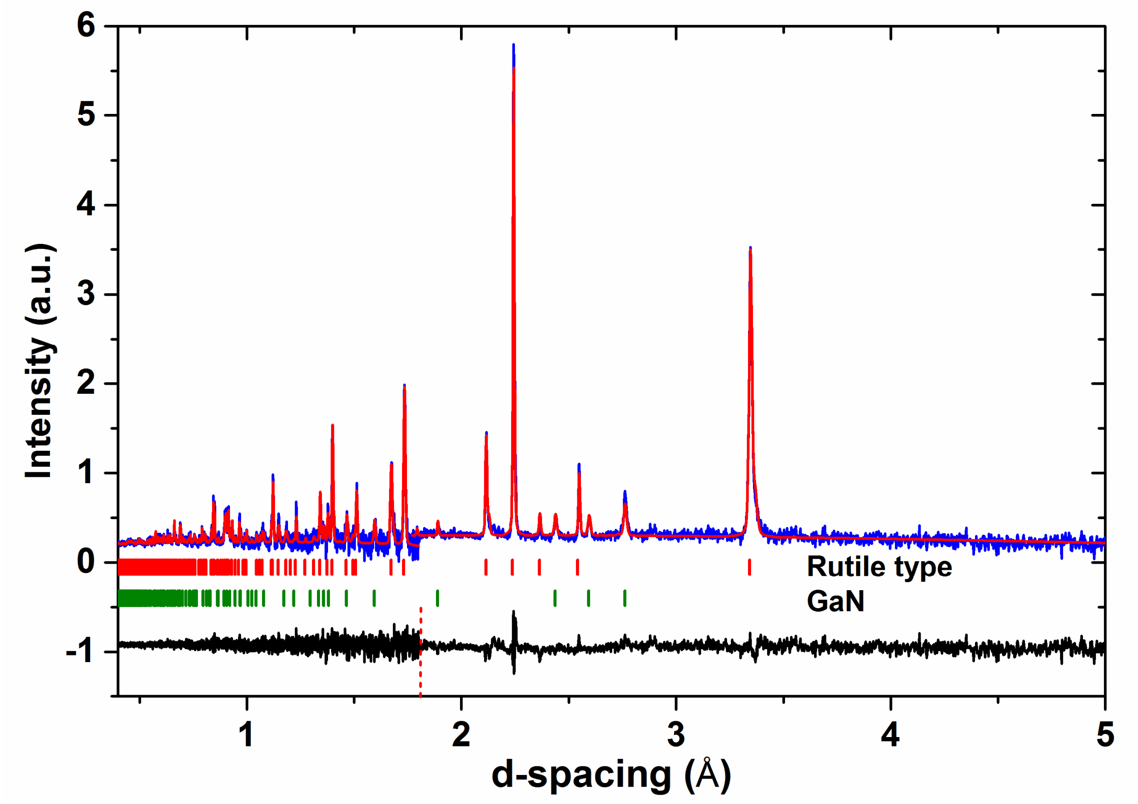

Figure 10. TOF powder neutron Rietveld refinement result of the 1 GPa - 1000°C synthesis. The patterns from both banks 1 (left) and 5 (right) are shown and are separated by the red dashed line in the difference pattern. The collected pattern is shown in blue, the calculated pattern in red, and the difference in black. The tick marks show the positions of reflections of the respective phases. The $GaNbO_4$ and T-Nb_2O_5 reflections were too weak to be incorporated into the refinement.

3 GPa - 1200°C

The synthesis at 3 GPa - 1200°C yielded approximately 50 mg of sample used to collect a high-resolution powder XRD pattern. A Rietveld refinement using TOPAS revealed three phases to be present in sample - major rutile type, and minor PbO_2 type in addition to GaN (Figure 11). The oxide phases of $GaNbO_4$ and Nb_2O_5 that were present at 1 GPa are notably absent and have participated in the reaction at 3 GPa. The rutile type phase in the sample has a large asymmetric peak shape likely due to chemical inhomogeneity during the slow phase transition to PbO_2 type phase. The asymmetric peak shape of the rutile type phase was modeled as a constrained distribution of rutile phases (Figure 11 inset). While the constrained multiphase approach did model the rutile type intensities well, the cation occupancy was globally set for the distribution of phases and allowed to refine. Allowing each rutile type phase to refine the occupancy is unrealistic due to the reflection overlap, so the distribution of chemistries and the actual occupancy of Ga and Nb in these phases cannot be accurately determined. The chemistry of the PbO_2 type phase was set to that of the 1 GPa rutile phase because when the cation occupancy was left to freely refine, it was unstable and would converge at unrealistic ratios of Ga and Nb with no improvement to the refinement. The refinement and crystallographic details of the PbO_2 type phase are shown in Table 1.

The GaN – Nb_2O_5 system presents a worst-case scenario for evaluating crystal structure prediction theory as a guide for synthetic efforts, as not only can the anions disorder, the cations have the potential to disorder as well. In oxides at 6-fold coordination, Ga^{3+} and Nb^{5+} have nearly identical ionic radii (Ga^{3+} = 0.62 and Nb^{5+} = 0.64 Å).[60] In retrospect, it is not surprising the predicted structure does not match the experimental results due to the high probability that configurational entropy would lower the enthalpy of formation of new phases, with occupational disorder being possible between Ga^{3+} and Nb^{5+} as well as N^{3-} and O^{2-}, for which of USPEX cannot take into account.

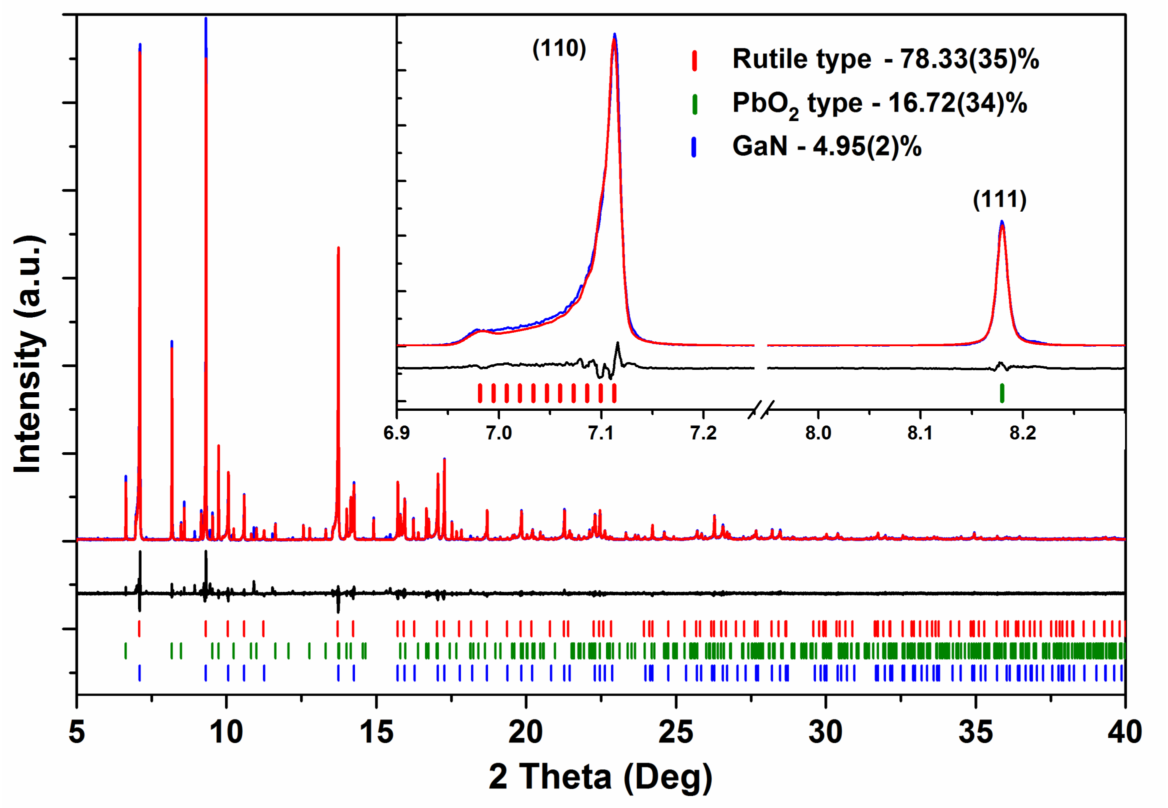

Figure 11. XRD Rietveld refinement result of the 3 GPa - 1200°C synthesis. The collected pattern is shown in blue, the calculated pattern in red, and the difference in black. The tick marks show the positions of reflections of the respective phases. The inset compares the largest reflection of the rutile type (110) with that of the PbO_2 type (111).

Table 1. X-ray Rietveld Refinement Results for $Nb_{1.412}Ga_{0.583}O_{3.412}N_{0.588}$

	TiO_2 type	**PbO_2 type**
Pressure	1 GPa	3 GPa
Temperature	1000°C	1200°C
Space Group	$P4_2/mnm$	Pbcn
a (Å)	4.72939(3)	4.63629(3)
b (Å)	4.72939(3)	5.59467(4)
c (Å)	3.02110(2)	4.97802(3)
Volume (Å^3)	67.573(1)	129.122(1)
Rp	0.9031	0.9468
wRp	0.1188	0.1379
$\chi 2$	1.628	1.513

Table 2. Neutron Rietveld Refinement Results for TiO_2 type Phase

Pressure	1 GPa
Temperature	1000°C
Space Group	$P4_2/mnm$
a (Å)	4.72815(22)
b (Å)	4.72815(22)
c (Å)	3.01373(11)
Volume ($Å^3$)	67.373(5)
Bank 1 R_p	0.1167
Bank 1 wR_p	0.0799
Bank 6 R_p	0.1366
Bank 6 wR_p	0.1062
$\chi 2$	1.621

Table 3. Structure details from neutron and X-ray refinements

Atom	**x**	**y**	**z**	**U_{iso}**
TiO_2-Type (Neutron)				
M	0.0	0.0	0.0	0.0122(4)
A	0.29497(18)	0.29497(18)	0.0	0.01192(28)
PbO_2-Type (X-ray)				
M	0.0	0.17491(18)	0.25	0.0098(25)
A	0.26944(96)	0.38639(74)	0.42006(86)	0.0036(12)

TiO_2-type

M occupancy Nb = 0.709(14)   Ga = 0.290(14)

A occupancy O = 0.856(3)   N = 0.144(3)

Table 4. Selected bond distances of oxynitride phases

TiO_2-type (neutron)		
M-A	1.9723(23)	x4
	2.0372(8)	x2
M-M	3.01372(5)	
PbO_2-type		
M-A	1.9176(45)	x2
	1.9894(43)	x2
	2.1130(43)	x2
M-M	3.1663(13)	

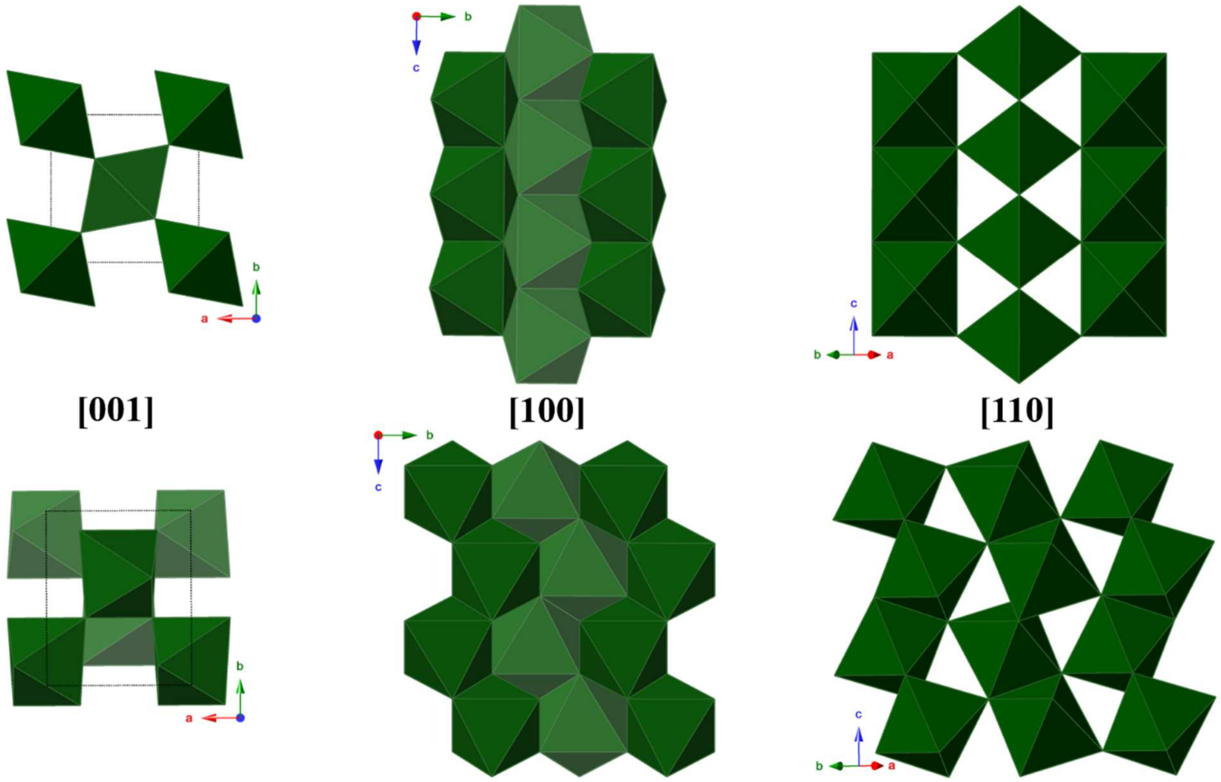

Figure 12. Crystal structure of rutile type (top) and PbO_2 type oxynitride phase (bottom) in polyhedral representation.

HPHT $NbGaO_4$

An additional HPHT $NbGaO_4$ synthesis experiment at 1 GPa and 1000°C was performed to confirm the possible stable minor oxide phases found in the HPHT oxynitride synthesis. The product of the experiment was predominantly Wolframite type $NbGaO_4$ with minor *T*-Nb_2O_5 and β-Ga_2O_3 (Figure 13). While $NbGaO_4$ is a known wide band gap semiconductor the sample was a black color much like the oxynitride phases.[61, 62]

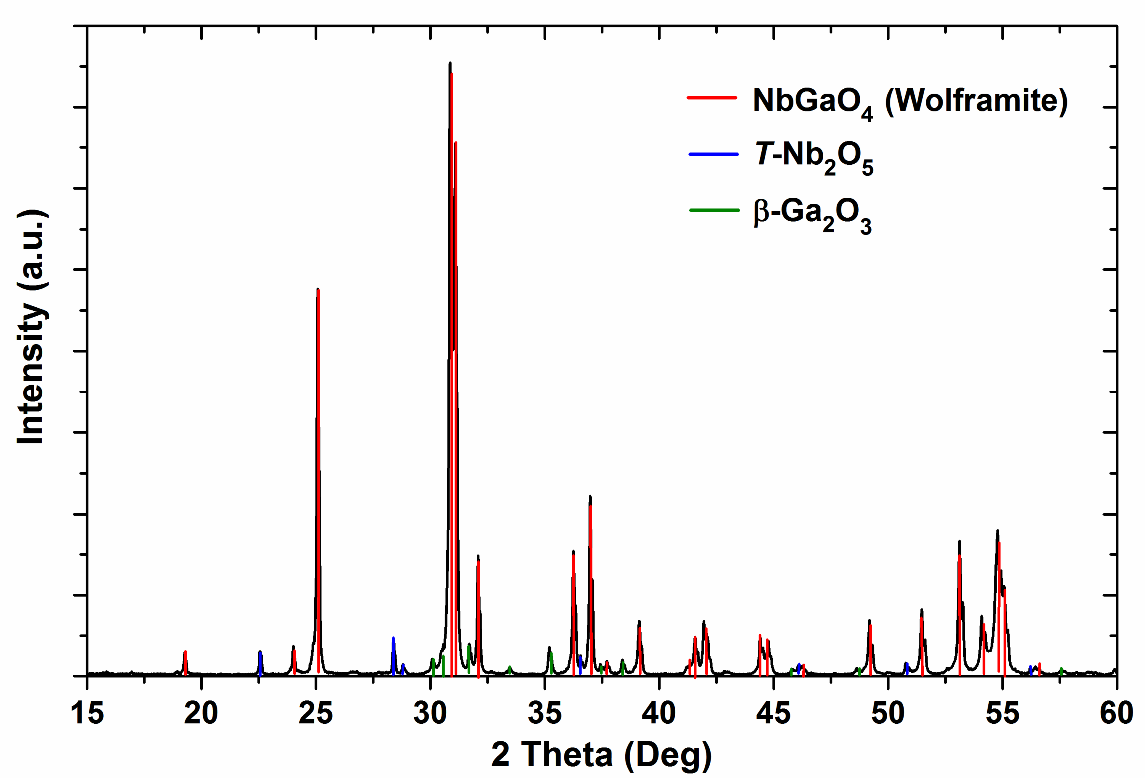

Figure 13. Angle dispersive XRD pattern (CuKα) of the product of a HPHT synthesis of a 1:1 mix of Ga_2O_3 and Nb_2O_5 at 1 GPa and 1000°C. The major product is a wolframite structured $NbGaO_4$ (red) with minor T-Nb_2O_5 (blue) and β-Ga_2O_3 (green).

Optical Properties of Rutile Type Oxynitride

The optical properties of the rutile-structured oxynitride were evaluated using UV-VIS-NIR diffuse reflectance to determine whether the band gap was suitable for water splitting photocatalysis. Relative absorbance (α_{KM}) was generated using a Kubelka-Munk transform and was fit using the same band gap functional fitting methods used to study the optical properties of $(GaN)_{1-x}(ZnO)_x$ nanorods and nanocrystalline oxynitride spinel.[63, 64] The optical fitting revealed a contribution from a direct band gap of 0.84 eV as well as an indirect band gap of 0.51 eV (Figure 14).

The optical data and band gaps are consistent with the black color of the powder as it absorbs through the visible range. The short band gap is unexpected as the respective oxide, $GaNbO_4$, is a wide band-gap semiconductor.[61, 62] However, a HPHT reaction of Ga_2O_3 and Nb_2O_5 at identical synthesis conditions (1 GPa, 1000°C) produced a black powder of wolframite type $GaNbO_4$ (Figure 13). The color in both the HPHT oxide and oxynitride is likely due to reduction of Nb^{5+} at the surface due to the moderately reducing conditions imposed by the graphite furnace.[65] Such a surface reduction occurs when rutile, TiO_2 (Ti^{4+} to Ti^{3+}), is heated under reducing atmospheres.[66] Synthesis under a less reducing atmosphere or post synthesis oxidative treatment could change the color and perceived optical band gap. Unfortunately, in the as synthesized state, the rutile type $Nb_{1.412}Ga_{0.583}O_{3.412}N_{0.588}$ is not suitable for photocatalytic water splitting.

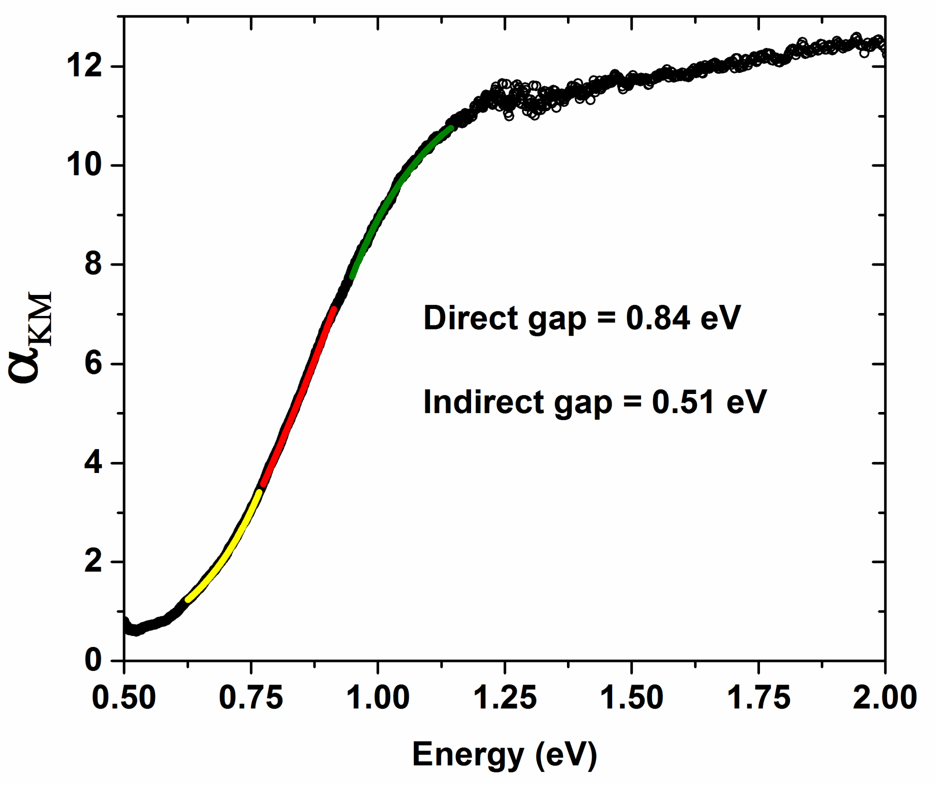

Figure 14. Kubelka-Munk absorption of the rutile type phase synthesized at 1 GPa - 1000°C. The absorbance regions are modelled showing the direct band gap (green line), indirect band gap (red line), and the Urbach tail (yellow line).

Conclusions

We have demonstrated the successful use of combinatory techniques that can be used to speed up and optimize the discovery of compounds at high-pressure. While being used in an unfavorable capacity, USPEX successfully guided the synthetic efforts acting as a reaction indicator. While the predicted $GaNb_2O_5N$ oxynitride in the GaN – Nb_2O_5 system was not formed, the *in situ* EDXRD investigation mapped out the P-T reaction space in the course of a single day, leading to the discovery of two different $Nb_{1.412}Ga_{0.583}O_{3.412}N_{0.588}$ phases having rutile and PbO_2 structures. Structural studies at DOE user facilities found the novel oxynitride phases have positional disorder amongst both the cations and the anions. The incorporation of positional disorder is currently not practical with state of the art crystal structure prediction algorithms. However, while the predicted structures may not match experimental results in the current implementation of USPEX, the variable composition calculations offer insights into the chemistry of the system and can be used to direct synthetic efforts with 0 K calculations at a significant overpressure. To increase the likelihood of success in oxynitride prediction, future directions will need to incorporate/account for disorder to better evaluate oxynitride systems.

References

1. Demazeau, G., High pressure and chemical bonding in materials chemistry. *Zeitschrift Fur Naturforschung Section B-a Journal of Chemical Sciences* **2006,** 61, (7), 799-807.

2. Range, K. J., Solid-state chemistry at high-pressure. *Chemie in Unserer Zeit* **1976,** 10, (6), 180-188.

3. Huppertz, H., New synthetic discoveries via high-pressure solid-state chemistry. *Chemical Communications* **2011,** 47, (1), 131-140.

4. Badding, J. V.; Meng, J. F.; Polvani, D. A., Pressure tuning in the search for new and improved solid state materials. *Chemistry of Materials* **1998,** 10, (10), 2889-2894.

5. Gregoryanz, E.; Sanloup, C.; Somayazulu, M.; Badro, J.; Fiquet, G.; Mao, H. K.; Hemley, R. J., Synthesis and characterization of a binary noble metal nitride. *Nature Materials* **2004,** 3, (5), 294-297.

6. Zhang, W. W.; Oganov, A. R.; Goncharov, A. F.; Zhu, Q.; Boulfelfel, S. E.; Lyakhov, A. O.; Stavrou, E.; Somayazulu, M.; Prakapenka, V. B.; Konopkova, Z., Unexpected Stable Stoichiometries of Sodium Chlorides. *Science* **2013,** 342, (6165), 1502-1505.

7. Lazicki, A.; Goncharov, A. F.; Struzhkin, V. V.; Cohen, R. E.; Liu, Z.; Gregoryanz, E.; Guillaume, C.; Mao, H. K.; Hemley, R. J., Anomalous optical and electronic properties of dense sodium. *Proceedings of the National Academy of Sciences of the United States of America* **2009,** 106, (16), 6525-6528.

8. Eremets, M. I.; Trojan, I. A., Evidence of maximum in the melting curve of hydrogen at megabar pressures. *Jetp Letters* **2009,** 89, (4), 174-179.

9. Oganov, A. R.; Ma, Y. M.; Lyakhov, A. O.; Valle, M.; Gatti, C., Evolutionary Crystal Structure Prediction as a Method for the Discovery of Minerals and Materials. In *Theoretical and Computational Methods in Mineral Physics: Geophysical Applications*, 2010; Vol. 71, pp 271-298.

10. Oganov, A. R.; Glass, C. W., Evolutionary crystal structure prediction as a tool in materials design. *Journal of Physics-Condensed Matter* **2008,** 20, (6), art icle 064210.

11. Oganov, A. R.; Chen, J. H.; Gatti, C.; Ma, Y. Z.; Ma, Y. M.; Glass, C. W.; Liu, Z. X.; Yu, T.; Kurakevych, O. O.; Solozhenko, V. L., Ionic high-pressure form of elemental boron. *Nature* **2009,** 457, (7231), 863-867.

12. Ma, Y.; Eremets, M. I.; Oganov, A. R.; Xie, Y.; Trojan, I.; Medvedev, S.; Lyakhov, A. O.; Valle, M.; Prakapenka, V., Transparent dense sodium. *Nature* **2009,** 458, 182-185.

13. Solozhenko, V. L.; Solozhenko, E. G.; Zinin, P. V.; Ming, L. C.; Chen, J. H.; Parise, J. B., Equation of state and phase stability of turbostratic carbon nitride. *Journal of Physics and Chemistry of Solids* **2003,** 64, (8), 1265-1270.

14. Maddox, J., Crystals from 1st principles. *Nature* **1988,** 335, (6187), 201-201.

15. Disalvo, F. J., Solid-state chemistry - a rediscovered chemical frontier. *Science* **1990,** 247, (4943), 649-655.

16. Glass, C. W.; Oganov, A. R.; Hansen, N., USPEX - Evolutionary crystal structure prediction. *Computer Physics Communications* **2006,** 175, (11-12), 713-720.

17. Hautier, G.; Fischer, C.; Ehrlacher, V.; Jain, A.; Ceder, G., Data Mined Ionic Substitutions for the Discovery of New Compounds. *Inorganic Chemistry* **2011,** 50, (2), 656-663.

18. Wu, Y. B.; Lazic, P.; Hautier, G.; Persson, K.; Ceder, G., First principles high throughput screening of oxynitrides for water-splitting photocatalysts. *Energy & Environmental Science* **2013,** 6, (1), 157-168.

19. Curtarolo, S.; Morgan, D.; Persson, K.; Rodgers, J.; Ceder, G., Predicting crystal structures with data mining of quantum calculations. *Physical Review Letters* **2003,** 91, (13).

20. Fuertes, A., Synthesis and properties of functional oxynitrides - from photocatalysts to CMR materials. *Dalton Transactions* **2010,** 39, (26), 5942-5948.

21. Maeda, K.; Domen, K., New non-oxide photocatalysts designed for overall water splitting under visible light. *Journal of Physical Chemistry C* **2007,** 111, (22), 7851-7861.

22. Maeda, K.; Domen, K., Oxynitride materials for solar water splitting. *MRS Bulletin* **2011,** 36, (1), 25-31.

23. Maeda, K.; Teramura, K.; Domen, K., Effect of post-calcination on photocatalytic activity of (Ga1-xZnx)(N1-xOx) solid solution for overall water splitting under visible light. *Journal of Catalysis* **2008,** 254, (2), 198-204.

24. Troyanchuk, I. O.; Kasper, N. V.; Mantytskaya, O. S.; Shapovalova, E. F., High-Pressure Synthesis of Some Perovskite - Like Compounds with a Mixed Anion Type. *Materials Research Bulletin* **1995,** 30, (4), 421-425.

25. Yang, M. H.; Rodgers, J. A.; Middler, L. C.; Oro-Sole, J.; Jorge, A. B.; Fuertes, A.; Attfield, J. P., Direct Solid-State Synthesis at High Pressures of New Mixed-Metal Oxynitrides: $RZrO_2N$ (R = Pr, Nd, and Sm). *Inorganic Chemistry* **2009,** 48, (24), 11498-11500.

26. Soignard, E.; Machon, D.; McMillan, P. F.; Dong, J. J.; Xu, B.; Leinenweber, K., Spinel-structured gallium oxynitride (Ga(3)O(3)N) synthesis and characterization: An experimental and theoretical study. *Chemistry of Materials* **2005,** 17, (22), 5465-5472.

27. Kinski, I.; Miehe, G.; Heymann, G.; Theissmann, R.; Riedel, R.; Huppertz, H., High-pressure synthesis of a gallium oxonitride with a spinel-type structure. *Zeitschrift Fur Naturforschung Section B-a Journal of Chemical Sciences* **2005,** 60, (8), 831-836.

28. Huppertz, H.; Hering, S. A.; Zvoriste, C. E.; Lauterbach, S.; Oeckler, O.; Riedel, R.; Kinski,

I., High-Pressure Synthesis, Electron Energy-Loss Spectroscopy Investigations, and Single Crystal Structure Determination of a Spinel-Type Gallium Oxonitride Ga-2.79 square(0.21)(O3.05N0.76 square(0.19)). *Chemistry of Materials* **2009,** 21, (10), 2101-2107.

29. Hering, S. A.; Zvoriste, C. E.; Riedel, R.; Kinski, I.; Huppertz, H., A Systematic Investigation of the Stability Field of Spinel-type Gallium Oxonitrides. *Zeitschrift Fur Naturforschung Section B-a Journal of Chemical Sciences* **2009,** 64, (10), 1115-1126.

30. Chen, H. Y.; Wang, L. P.; Bai, J. M.; Hanson, J. C.; Warren, J. B.; Muckerman, J. T.; Fujita, E.; Rodriguez, J. A., In Situ XRD Studies of ZnO/GaN Mixtures at High Pressure and High Temperature: Synthesis of Zn-Rich $(Ga_{1-x}Zn_x)(N_{1-x}O_x)$ Photocatalysts. *Journal of Physical Chemistry C* **2010,** 114, (4), 1809-1814.

31. Haines, J.; Chateau, C.; Leger, J. M.; Le Sauze, A.; Diot, N.; Marchand, R.; Hull, S., Crystal structure of moganite-type phosphorus oxynitride: relationship to other twinned-quartz-based structures. *Acta Crystallographica Section B-Structural Science* **1999,** 55, 677-682.

32. Baumann, D.; Sedlmaier, S. J.; Schnick, W., An Unprecedented AB(2) Tetrahedra Network Structure Type in a High-Pressure Phase of Phosphorus Oxonitride (PON). *Angewandte Chemie-International Edition* **2012,** 51, (19), 4707-4709.

33. Li, Q.; Ma, Y. M.; Oganov, A. R.; Wang, H. B.; Wang, H.; Xu, Y.; Cui, T.; Mao, H. K.; Zou, G. T., Superhard Monoclinic Polymorph of Carbon. *Physical Review Letters* **2009,** 102, (17), 175506.

34. Oganov, A. R.; Ma, Y. M.; Xu, Y.; Errea, I.; Bergara, A.; Lyakhov, A. O., Exotic behavior and crystal structures of calcium under pressure. *Proceedings of the National Academy of Sciences of the United States of America* **2010,** 107, (17), 7646-7651.

35. Zhou, X. F.; Oganov, A. R.; Qian, G. R.; Zhu, Q., First-Principles Determination of the Structure of Magnesium Borohydride. *Physical Review Letters* **2012,** 109, (24).

36. Bazhanova, Z. G.; Oganov, A. R.; Gianola, O., Fe-C and Fe-H systems at pressures of the Earth's inner core. *Physics-Uspekhi* **2012,** 55, (5), 489-497.

37. Zeng, Q. F.; Peng, J. H.; Oganov, A. R.; Zhu, Q.; Xie, C. W.; Zhang, X. D.; Dong, D.; Zhang, L. T.; Cheng, L. F., Prediction of stable hafnium carbides: Stoichiometries, mechanical properties, and electronic structure. *Physical Review B* **2013,** 88, (21).

38. Zhu, Q.; Jung, D. Y.; Oganov, A. R.; Glass, C. W.; Gatti, C.; Lyakhov, A. O., Stability of xenon oxides at high pressures. *Nature Chemistry* **2013,** 5, (1), 61-65.

39. Zhu, Q.; Oganov, A. R.; Lyakhov, A. O., Novel stable compounds in the Mg-O system under high pressure. *Physical Chemistry Chemical Physics* **2013,** 15, (20), 7696-7700.

40. Cheng, X. Y.; Zhang, W.; Chen, X. Q.; Niu, H. Y.; Liu, P. T.; Du, K.; Liu, G.; Li, D. Z.; Cheng, H. M.; Ye, H. Q.; Li, Y. Y., Interstitial-boron solution strengthened WB3+x. *Applied Physics Letters* **2013,** 103, (17).

41. Cheng, X.-Y.; Chen, X.-Q.; Li, D.-Z.; Li, Y.-Y., Computational materials discovery: the case of the W-B system. *Acta Crystallographica Section C* **2014,** 70, (2), 85-103.

42. Zeng, Q.; Oganov, A. R.; Lyakhov, A. O.; Xie, C.; Zhang, X.; Zhang, J.; Zhu, Q.; Wei, B.; Grigorenko, I.; Zhang, L.; Cheng, L., Evolutionary search for new high-k dielectric materials: methodology and applications to hafnia-based oxides. *Acta Crystallographica Section C* **2014,** 70, (2), 76-84.

43. Yang, M. H.; Oro-Sole, J.; Rodgers, J. A.; Jorge, A. B.; Fuertes, A.; Attfield, J. P., Anion order in perovskite oxynitrides. *Nature Chemistry* **2011,** 3, (1), 47-52.

44. Attfield, J. P., Principles and Applications of Anion Order in Solid Oxynitrides. *Crystal Growth & Design* **2013,** 13, (10), 4623-4629.

45. Clark, L.; Oro-Sole, J.; Knight, K. S.; Fuertes, A.; Attfield, J. P., Thermally Robust Anion-Chain Order in Oxynitride Perovskites. *Chemistry of Materials* **2013,** 25, (24), 5004-5011.

46. Oro-Sole, J.; Clark, L.; Bonin, W.; Attfield, J. P.; Fuertes, A., Anion-ordered chains in a d1 perovskite oxynitride: NdVO2N. *Chemical Communications* **2013,** 49, (24), 2430-2432.

47. Oro-Sole, J.; Clark, L.; Kumar, N.; Bonin, W.; Sundaresan, A.; Attfield, J. P.; Rao, C. N. R.; Fuertes, A., Synthesis, anion order and magnetic properties of RVO3-xNx perovskites (R = La, Pr, Nd; 0 [less-than-or-equal] x [less-than-or-equal] 1). *Journal of Materials Chemistry C* **2014,** 2, (12), 2212-2220.

48. Bischoff, A.; Grund, T.; Jording, T.; Heying, B.; Hoffmann, R. D.; Rodewald, U. C.; Pottgen, R., First refinement of the sinoite structure of a natural crystal from the neuschwanstein (EL6) meteorite. *Zeitschrift Fur Naturforschung Section B-a Journal of Chemical Sciences* **2005,** 60, (12), 1231-1234.

49. Srinivasa, S. R.; Cartz, L.; Jorgensen, J. D.; Worlton, T. G.; Beyerlein, R. A.; Billy, M., High-Pressure Neutron-Diffraction Study of Si2n2o. *Journal of Applied Crystallography* **1977,** 10, (Jun1), 167-171.

50. Yashima, M.; Lee, Y.; Domen, K., Crystal structure and electron density of tantalum oxynitride, a visible light responsive photocatalyst. *Chemistry of Materials* **2007,** 19, (3), 588-593.

51. Oganov, A. R.; Glass, C. W., Crystal structure prediction using ab initio evolutionary techniques: Principles and applications. *Journal of Chemical Physics* **2006,** 124, (24), 244704.

52. Oganov, A. R.; Lyakhov, A. O.; Valle, M., How Evolutionary Crystal Structure Prediction Works-and Why. *Accounts of Chemical Research* **2011,** 44, (3), 227-237.

53. Lyakhov, A. O.; Oganov, A. R.; Stokes, H. T.; Zhu, Q., New developments in evolutionary structure prediction algorithm USPEX. *Computer Physics Communications* **2013,** 184, (4), 1172-1182.

54. Blochl, P. E., Projector Augmented-Wave Method. *Physical Review B* **1994,** 50, (24),

17953-17979.

55. Kresse, G.; Furthmuller, J., Efficient iterative schemes for ab initio total-energy calculations using a plane-wave basis set. *Physical Review B* **1996,** 54, (16), 11169-11186.

56. Perdew, J. P.; Burke, K.; Ernzerhof, M., Generalized gradient approximation made simple. *Physical Review Letters* **1996,** 77, (18), 3865-3868.

57. Troullier, N.; Martins, J. L., Efficient Pseudopotentials for Plane-Wave Calculations. *Physical Review B* **1991,** 43, (3), 1993-2006.

58. A. C. Larson, R. B. V. D., General Structure Analysis System (GSAS). *Los Alamos National Laboratory* **2000,** Report LAUR 86-748.

59. Toby, B. H., EXPGUI, a graphical user interface for GSAS. *Journal of Applied Crystallography* **2001,** 34, 210-213.

60. Shannon, R. D., Revised Effective Ionic-Radii and Systematic Studies of Interatomic Distances in Halides and Chalcogenides. *Acta Crystallographica Section A* **1976,** 32, (Sep1), 751-767.

61. Blasse, G.; Buth, A. H.; Buth, A. H., The Luminescence of the High-Pressure Modification of Gallium Niobate (Ganbo4). *Journal of Solid State Chemistry* **1981,** 37, (2), 264-266.

62. Devi, S.; Kelkar, S.; Kashid, V.; Salunke, H. G.; Gupta, N. M., Preparation-method-dependent morphological, band structural, microstructural, and photocatalytic properties of noble metal-GaNbO4 nanocomposites. *Rsc Advances* **2013,** 3, (37), 16817-16828.

63. Reinert, A. A.; Payne, C.; Wang, L. M.; Ciston, J.; Zhu, Y. M.; Khalifah, P. G., Synthesis and Characterization of Visible Light Absorbing (GaN)(1-x)(ZnO)(x) Semiconductor Nanorods. *Inorganic Chemistry* **2013,** 52, (15), 8389-8398.

64. Dharmagunawardhane, H. A. N.; Woerner, W. R.; Wu, Q.; Huang, H.; Chen, X.; Orlov, A.; Khalifah, P. G.; Parise, J. B., Photocatalytic hydrogen evolution using nanocrystalline gallium oxynitride spinel. *Journal of Materials Chemistry A* **2014,** 2, (45), 19247-19252.

65. Whitaker, M. L.; Nekvasil, H.; Lindsley, D. H.; Difrancesco, N. J., The role of pressure in producing compositional diversity in intraplate basaltic magmas. *Journal of Petrology* **2007,** 48, (2), 365-393.

66. Khomenko, V. M.; Langer, K.; Rager, H.; Fett, A., Electronic absorption by Ti3+ ions and electron delocalization in synthetic blue rutile. *Physics and Chemistry of Minerals* **1998,** 25, (5), 338-346.

Chapter 3

Evaluating carbon dioxide adsorption of metal-organic frameworks and zeolites under humid conditions using coupled *in situ* X-ray diffraction and calorimetry techniques

Abstract

Combined application of *in situ* X-ray diffraction (XRD) and differential scanning calorimetry (DSC) is a novel technique for evaluating the suitability of microporous compounds for post-combustion CO_2 capture. While many microporous compounds show promise for CO_2 capture, most are not evaluated in the presence of water vapor, a major component of post-combustion flue-gas. Compounds evaluated include representatives of the classes of compounds typically proposed for CO_2 capture, zeolites and metal-organic frameworks (MOFs): zeolite NaX, Ni-MOF-74 [Ni_2(dobdc); dobdc = 2,5-dihydroxyterephtalate], ZIF-7 [ZIF: Zeolitic Imidazole Framework, $Zn(phim)_2$; phim: benzimidazole] and CaSDB [SDB: 4,4'-sulfonyldibenzoate]. Although NaX and Ni-MOF-74 show very high affinity towards CO_2 under idealized dry conditions, they are also very sensitive to the presence of water vapor and experience significant performance loss at 25% relative humidity (RH). Relative to NaX and Ni-MOF-74, ZIF-7 and CaSDB are found to be resistant to water vapor and show strong CO_2 affinity even in the presence of 75% RH. The CO_2 enthalpy of adsorption of in ZIF-7, a flexible framework that undergoes a guest-induced gate-opening phase transition, is ~11 kJ/mol before, and ~27 kJ/mol after the transition. At 22°C and 75% RH CO_2 adsorption shifts the gate-opening transition in ZIF-7 to a higher pressure by 0.1 atm. This investigation presents a new method for screening microporous

compounds for post-combustion flue-gas carbon dioxide capture.

Introduction

As atmospheric carbon dioxide concentrations continue to rise in conjunction with fossil fuel consumption, the mitigation of carbon dioxide emissions from anthropogenic sources has become one of the most important environmental challenges we face today. Current sequestration efforts have focused on CO_2 capture at existing stationary emission sources as ~60% of the worldwide carbon dioxide emission is from electricity generation.[1, 2] The CO_2 emissions just from coal combustion constitute 30 - 40% of the total anthropogenic contribution and is expected to increase as energy demands grow.[3] The conventional CO_2 capture methods involving aqueous alkanolamine solutions are effective, but these solutions are corrosive, toxic and require a large amount of energy for regeneration after CO_2 saturation (up to 30% of the output of coal power plants).[2, 4-6] Thus focus has shifted to more energy efficient and environmental friendly methods such adsorption in microporous solids.

Solid-state adsorption using zeolites and metal-organic frameworks (MOFs) are promising solutions that can be employed for post-combustion carbon dioxide capture as they tend to have high CO_2 selectivity and adsorption capacity.[2, 7] Porous aluminosilicate zeolites are produced at the industrial scale and have high surface area, chemical, and thermal stability. MOFs have garnered significant interest as they are structurally diverse while having tunable pores and high surface area.[2, 8] However, post-combustion capture involves removing CO_2 in the presence of water vapor from a flue-gas stream and while some zeolite and MOF compounds have been shown to have excellent CO_2 adsorption properties under dry conditions, very few studies have evaluated adsorption performance in humid gas streams.[9-12]

Capturing CO_2 from sources such as flue-gas from coal-fired power plants with microporous compounds is challenging as the presence of water vapor competes for adsorption sites and reduces the ability of porous compounds to adsorb CO_2. Flue-gas produced at coal-fired power plants has 5-7% H_2O by volume in addition to N_2 (73-77%), CO_2 (15-16%), and O_2 (3-4%).[13] Gas adsorption performance is typically evaluated with gas adsorption isotherms and gas breakthrough experiments while structural studies are independently conducted with X-ray and neutron scattering.[2, 7, 14-18] Thus far, the effect of water vapor on the adsorption process has only been studied with breakthrough experiments in humid gas streams or with dry isotherm measurements on samples after exposure water vapor.[9, 11, 12, 19-21] Understanding a compound's adsorption characteristics in the presence of water is essential for the development and optimization of new functional compounds for post-combustion CO_2 capture.

Recently, calorimetric measurements have emerged as a new technique to evaluate gas adsorption in microporous compounds. Using calorimetry, the enthalpy of adsorption for a gas can be directly measured at any desired condition as opposed to being indirectly calculated with the isosteric heats of adsorption (Q_{st}) technique, which relies on modeling isotherms collected at multiple temperatures. A calorimetric approach is especially advantageous when dealing with adsorption phase transitions, gate-opening processes, or complex adsorption for which the Clausius–Clapeyron cannot be applied for Q_{st} calculation.[22, 23] Calorimetry has been previously used to investigate the CO_2 enthalpy of adsorption of on CD-MOF-2 and noble gasses (Xe and Kr) on Cu HKUST-1 using a Calvert-type microcalorimeter with a commercial gas dosing system.[22, 24] Early versions of the coupled X-ray diffraction – differential scanning calorimetry (XRD-DSC) technique described here were used to investigate the CO_2 and N_2 differential enthalpies of adsorption on CaSDB and CdSDB.[15, 16]

Using combinatory *in situ* XRD-DSC techniques, we are able to study the performance and structural effects of CO_2 adsorption in microporous compounds in humid gas streams. Herein, the XRD-DSC system in its entirety is presented as well as the types of gas adsorption experiments that can be conducted with humid gas streams at room temperature (22°C). The XRD-DSC system allows for the direct calorimetric measurement of the total enthalpy of adsorption while simultaneously collecting X-ray diffraction patterns to evaluate changes in the structure. We evaluate the performance and structural effects of CO_2 adsorption in the presence of water on a series of prevalent CO_2 sorption compounds – 3 metal organic frameworks (CaSDB, ZIF-7, and Ni-MOF-74) and zeolite NaX.

Design

The XRD-DSC system (Figure 1) is composed of a Rigaku Ultima IV diffractometer (CuKα radiation with a D/TeX high speed linear position sensitive detector), a Rigaku XRD-DSC stage, Rigaku HUM-1 humidity generator, ULVAC vacuum pump (5×10^{-4} Torr), a vacuum manifold, and a custom built humid atmosphere swing chamber. The humid atmosphere swing chamber (HASC) was necessary to buffer between the humidity generator and XRD-DSC stage so that both humid atmosphere and vacuum swings could be performed.

The system is organized (Figure 2) such that the desired gas flows from the selection manifold through a flow meter and into the humidity generator where mass flow controllers balance the mixing of wet and dry gas streams. The humidified gas mixture then flows into the HASC (Figure 3) where the relative humidity (RH) of the gas stream can stabilize based on a feedback interaction between the humidity probe and generator. Once the atmosphere has stabilized at the desired humidity, it is directed to the XRD-DSC stage through a needle valve. The vacuum manifold can pull vacuum directly on the XRD-DSC stage or allow gas to flow over the sample in the stage and exhaust to a fume hood.

The humidity of the atmosphere in the chamber is controlled through a feedback loop between the humidity probe and generator. The humid gas enters the chamber from the generator and can pass through to an exhaust until the atmosphere has a stable flow at the desired RH. The valve can then be switched to deliver the humid atmosphere to the sample on the DSC-XRD stage. In addition to atmosphere swings, the chamber allows for vacuum – humid atmosphere swings as the input from the generator can be closed off. Thus when the valve is opened between the XRD-DSC stage (at vacuum) and the chamber, the syringe base of the HASC moves due to the pressure differential and delivers the humid atmosphere to the sample in the XRD-DSC stage.

The design of XRD-DSC system allows for 3 types of sample treatment.

1. ***In situ* activation**: Prior to gas adsorption measurements, microporous compounds must be thermally activated to remove any stabilizing molecules occupying the adsorption sites. The microporous compounds can be thermally activated up to 350°C in the XRD-DSC stage under either vacuum or any desired atmosphere.
2. **Vacuum swing:** Perform vacuum to atmosphere swings up to 1 atm of pressure. This can mimic adsorption/desorption isotherms with non-corrosive gases at fixed humidity up to 90% RH.
3. **Atmosphere swing:** In this mode, flowing atmospheres can be exchanged to evaluate adsorption competition between gases/adsorbates at fixed humidity up to 90% RH.

Figure 1. (Left) Photo of complete XRD-DSC system. (Top right) XRD-DSC stage with sealing cap. (Bottom right) XRD-DSC attachment without cap showing the Al_2O_3 standard and sample powder on aluminum pans.

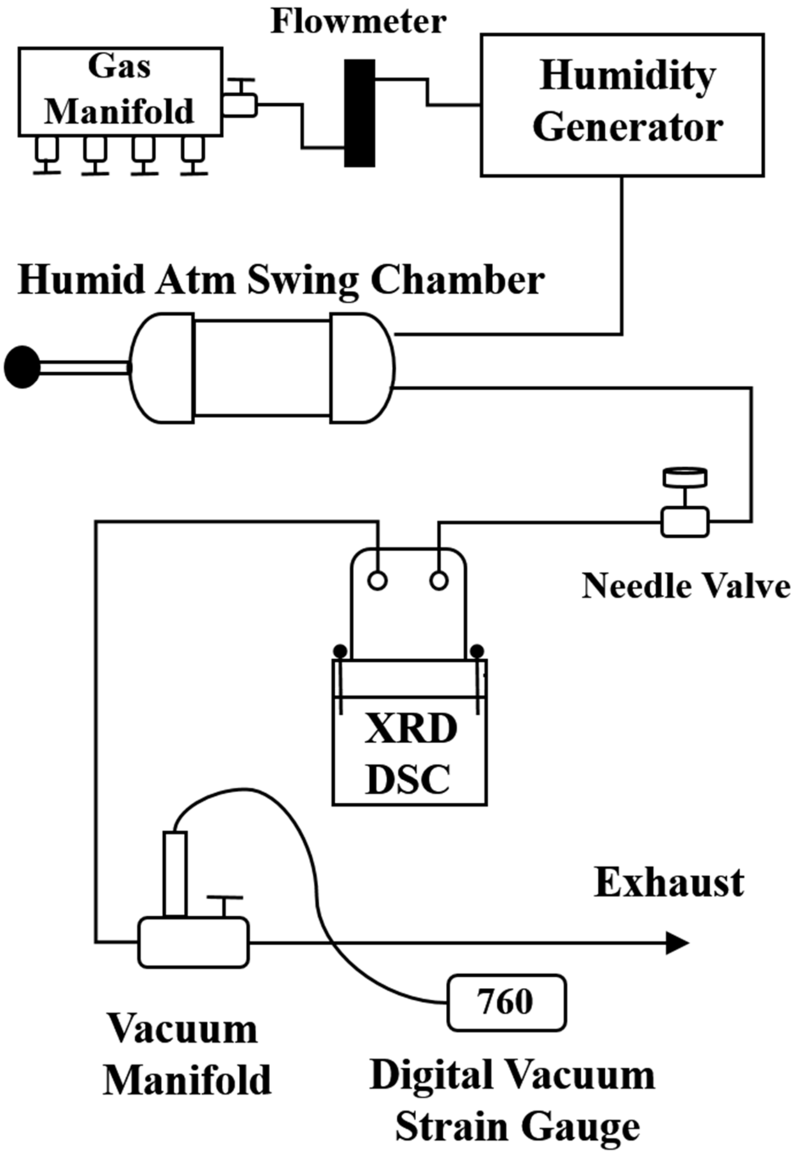

Figure 2. Schematic of entire XRD – DSC system.

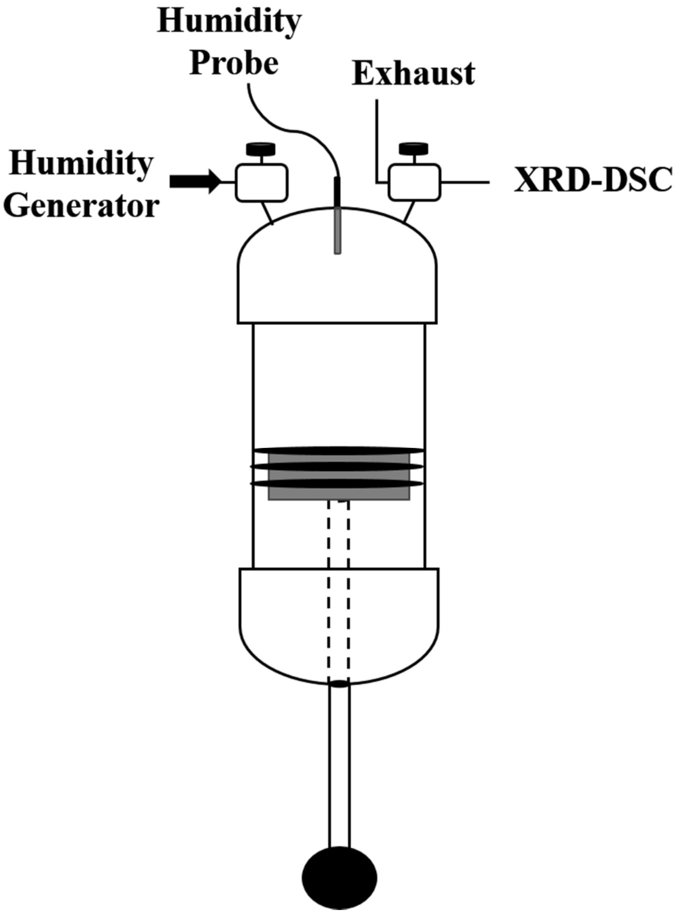

Figure 3. Schematic of humid atmosphere swing chamber (HASC). The atmosphere is input from the humidity generator which controls the mixing of wet and dry mass flow controllers based on feedback from a humidity probe sealed in the top of the chamber. The base of the chamber is designed like a syringe with a triple O-ring seal so the volume of the chamber can be changed without atmospheric contamination.

Data Collection

Powder X-ray Diffraction

The sample powder and DSC standard are loaded in separate aluminum pans (~ 10 mg each) on the XRD-DSC stage (Figure 1). Ideally, the stage is aligned so that the incident X-ray beam is only focused on the sample with the diffractometer in Bragg-Brentano geometry. If the sample and DSC standard pans are too close or filled too high with powder, some of the DSC standard powder may be in the beam path and the XRD patterns may be contaminated by reflections from the DSC standard. The size of the aluminum coated kapton® polyimide windows on the XRD-DSC stage cap limit the angular range to $5° \leq 2\theta \leq 40°$. While the 2θ coverage is limited, this range does cover the portions of the XRD patterns for microporous compounds most sensitive to changes in channel/pore chemistry – i.e. guest molecule sorption and desorption.

The powder XRD patterns were collected at a rate of 1°/min with a 0.02° step size over the available 2θ range. Due to the X-ray geometry and sample holders, avoidance of preferred orientation of the crystallites in the powder samples is difficult and often significantly impacts the relative intensity of observed reflections. Combined with the limited angular range of the data, this makes quantitative analysis difficult. However, the changes in low angle intensity however do provide valuable information for the qualitative comparison of framework responses to gas sorption, including phase transitions.

Calorimetric Measurements

The total enthalpies of adsorption were measured by the Rigaku DSC as part of the XRD-DSC stage. Powdered Al_2O_3 was used as the *in situ* DSC reference and the DSC was calibrated against the melting of Ga. The XRD-DSC can heat samples up to 350°C under vacuum or a non-corrosive atmosphere. The measurements are conducted at room temperature and as the XRD-DSC stage cannot actively cool, the experimental temperature is influenced by air temperature. While the temperature of the room housing the XRD-DSC system is strictly regulated, the experimental temperature can slowly vary by ±0.5°C. The DSC data was analyzed using ThermoPlus 2 Analysis software (v3.720, Rigaku).

Adsorption Measurements

Adsorption isotherm measurements were necessary to calculate the CO_2 enthalpy of adsorption for the compounds in this study. The CO_2 adsorption isotherms for NaX, and ZIF-7 were collected using a Quantachrome Autosorb–iQ gas sorption analyzer. The NaX samples were activated at 300°C and the ZIF-7 samples were activated at 200°C for 16 hours under high vacuum prior to the adsorption measurements. After activation, isotherms (up to 1 atm) were collected at 22°C for ZIF-7 and NaX. Prior adsorption isotherm data of CaSDB and Ni-MOF-74 were used for calculating the CO_2 enthalpy of adsorption.[25, 26]

Experimental

The compounds CaSDB [SDB: 4,4-sulfonyldibenzoate], ZIF-7 [Zn(benzimidazole)$_2$], Ni-MOF-74 [Ni$_2$(1,4-dioxide-2,5-benzenedicarboxylate)], and zeolite NaX were chosen for this study as all have shown high CO_2 adsorption capacity and selectivity while each having different attributes and adsorption mechanisms (Table 1).[7, 16, 18, 25, 27-29] CaSDB, ZIF-7, and Ni-MOF-74 are all MOFs while zeolite NaX is an inorganic aluminosilicate. CaSDB and ZIF-7 adsorb gases through organic linker coordination while Ni-MOF-74 and NaX adsorb via unsaturated metal sites.[7, 16-18] The structures of each compound are shown in Figures 4-7. Moreover, ZIF-7 is unique in that it has a pressure mediated gate-opening transition with adsorption/desorption hysteresis.[28]

Additionally, each compound has previously had some form of CO_2 adsorption evaluation in the presence of or after exposure to water vapor. The first XRD-DSC investigation found CaSDB still functions at high humidity (75% RH) using N_2 – CO_2 atmosphere swings.[16] ZIF-7 adsorption isotherms recorded after exposure to moist air (2.6 % v/v, 8.3% RH) at 12°C show only a ~2% reduction in capacity.[19] Zeolite NaX vacuum swing breakthrough experiments found the fixed bed productivity dropped 22% during exposure to simulated flue-gas at 30°C and 95% RH.[12] Adsorption measurements after exposing Ni-MOF-74 to water vapor found the capacity retention approaches zero at high relative humidity (90% RH, 25°C) and low humidity breakthrough experiments (3% RH, 25°C) found the capacity is reduced by 41% after once cycle.[21, 30]

The compounds CaSDB, ZIF-7, and Ni-MOF-74, were used as synthesized and zeolite NaX was commercially purchased (Linde 13X).[17, 25, 29] Each compound was activated *in situ* on the XRD-DSC stage by heating under vacuum at a rate of 2°/min to the desired temperature (CaSDB - 290°C, ZIF-7 - 200°C, Ni-MOF-74 - 200°C, NaX - 300°C) in order to remove the stabilizing molecules in the pores. Samples were held at the activation temperature for 12 hours then passively cooled back to room temperature (22°C) before adsorption swings.

Table 1. Summary of the microporous compounds characteristics

Compound	Type		Adsorption Mechanism		Gate-Opening Transition
	MOF	Zeolite	Organic-Linker Coordination	Unsaturated Metal Site	
CaSDB	X		X		
ZIF-7	X		X		X
Ni-MOF-74	X			X	
NaX		X		X	

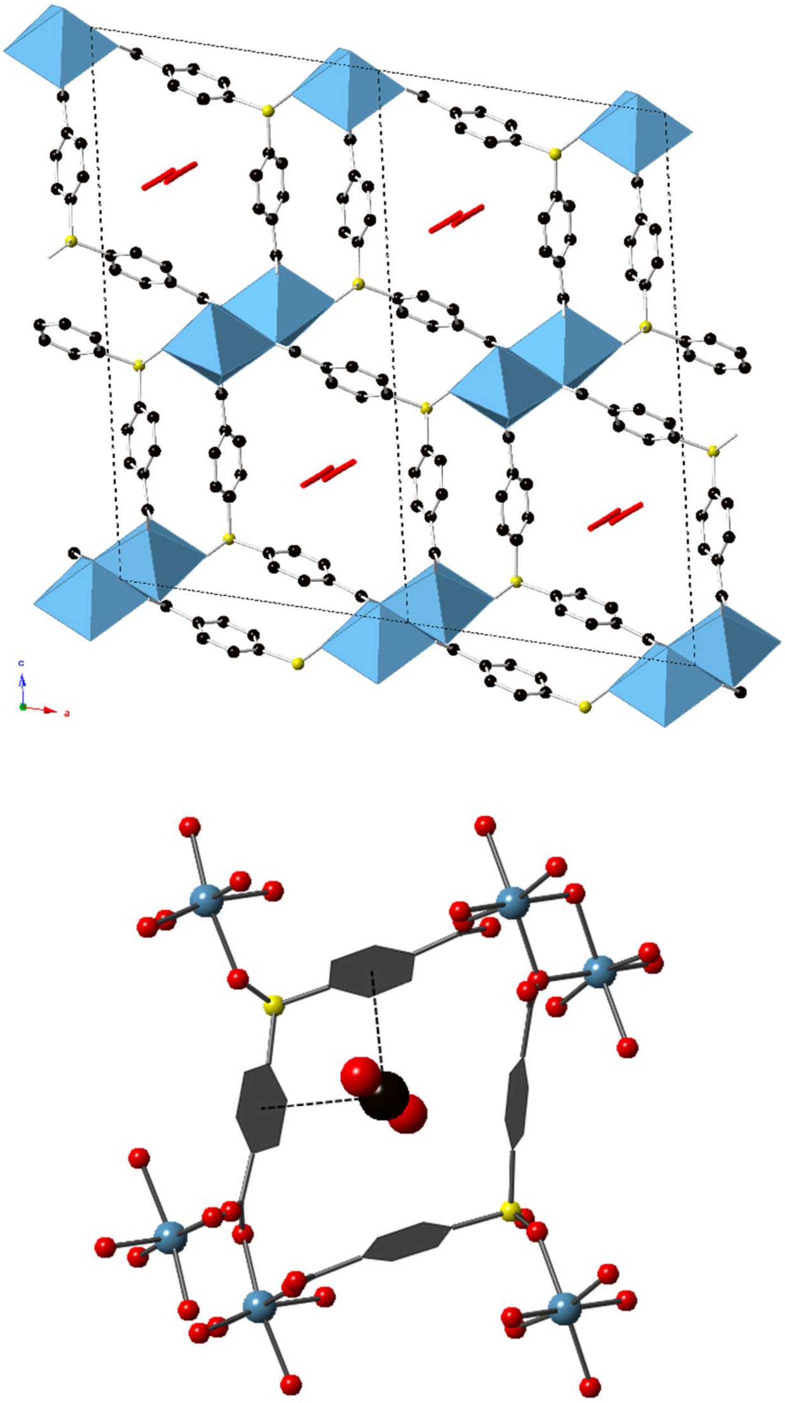

Figure 4. (top) Structure of CaSDB at 1 atm of CO_2. The calcium polyhedra are shown in blue, sulfur in yellow, carbon in black and CO_2 in red. The CO_2 molecules are coordinated to the two benzene rings. (bottom) Ball and stick model of the CaSDB pore showing only one of the partially occupied CO_2 sites coordinating to the benzene rings.

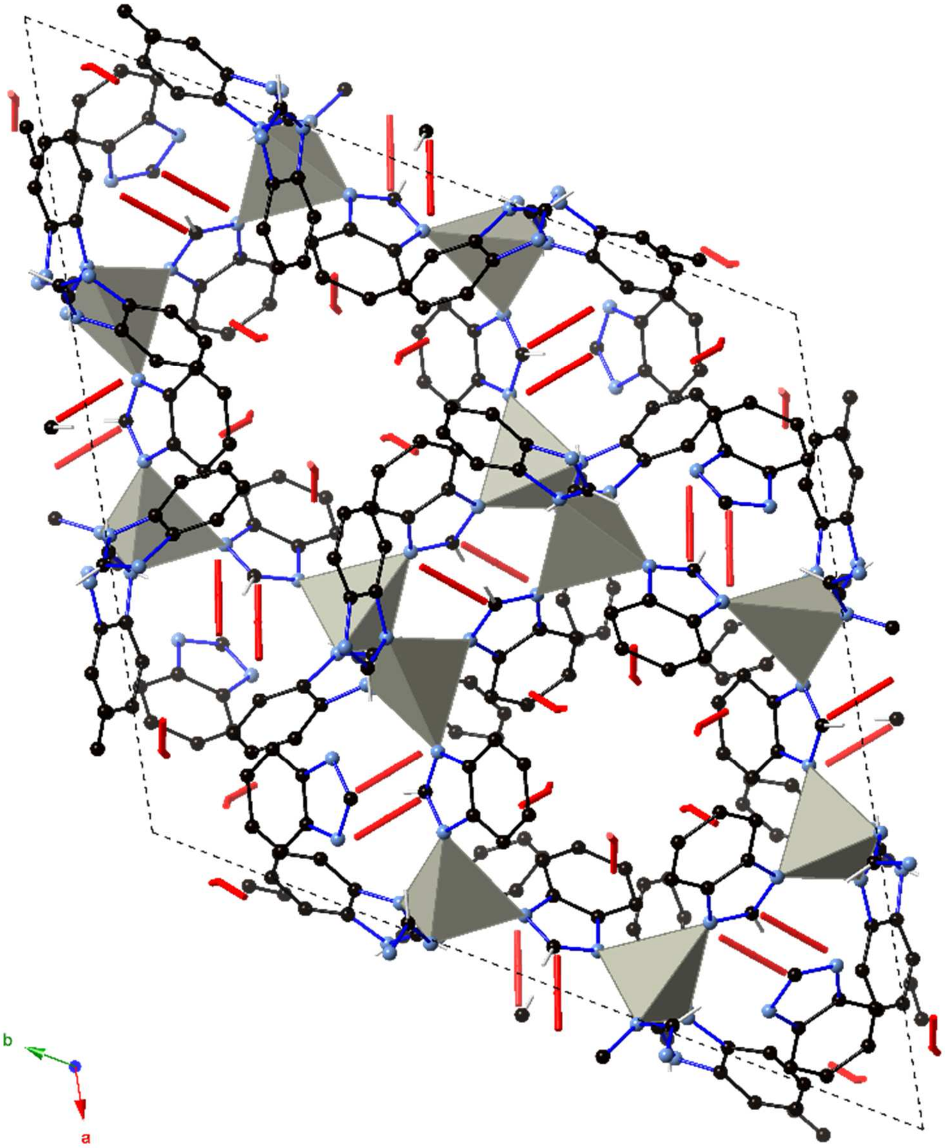

Figure 5. Structure of ZIF-7 (gate-open) at 1 atm of CO_2. Zinc tetrahedra are shown in grey, nitrogen in blue, carbon in black and CO_2 in red. The CO_2 molecules are coordinated to the benzimidazolate rings.

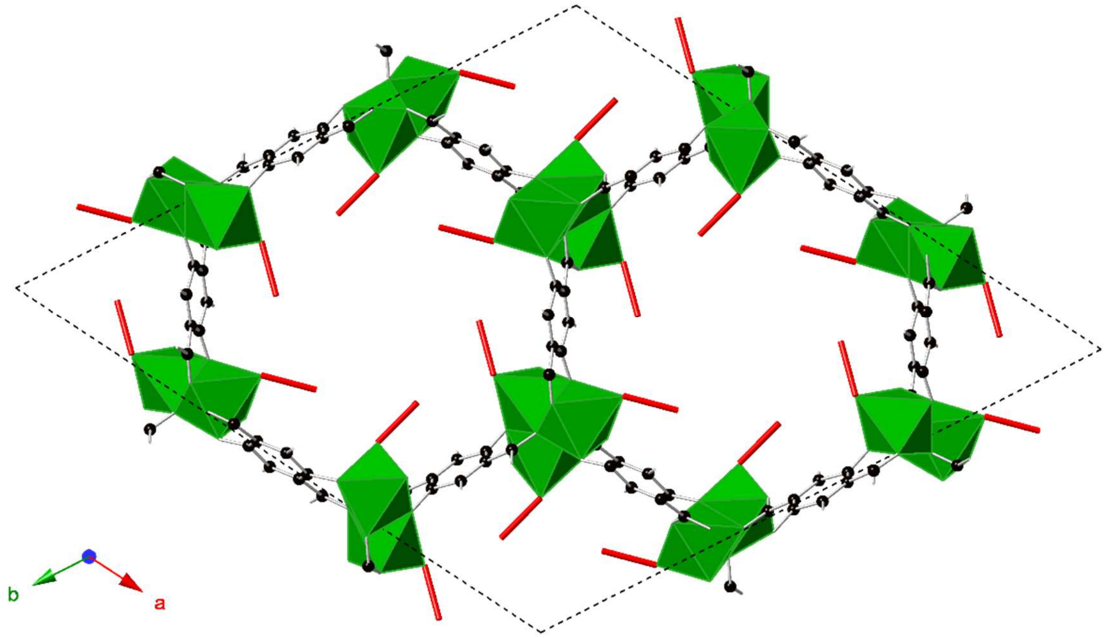

Figure 6. Structure of Ni-MOF-74 at 1 atm CO_2. Nickel octahedra are green, carbon atoms are black, and CO_2 is red. The CO_2 molecules are coordinated to the Ni atoms and the oxygen atoms of CO_2 complete the Ni octahedra.

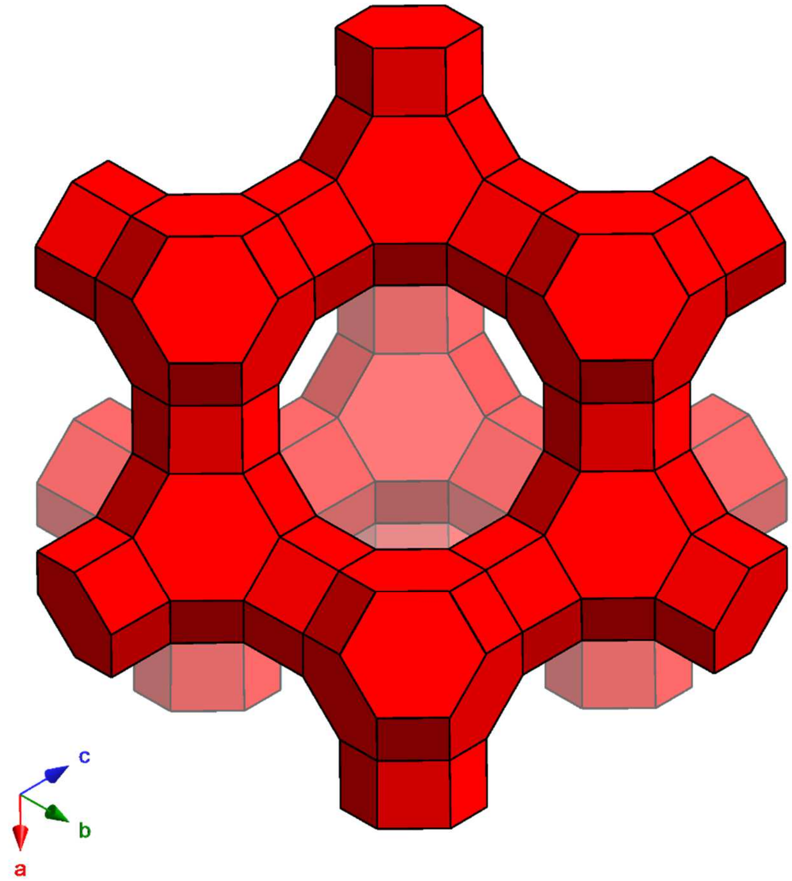

Figure 7. Framework structure of dehydrated zeolite NaX. The aluminosilicate network (red) is shown as polyhedral representation of the interconnected cages with the oxygen atoms and extra framework cations omitted for clarity.

Results and Discussion

Vacuum – Atmosphere Swings

In the simplest form, vacuum – atmosphere swings using the XRD-DSC can be used to mimic past calorimetric experiments and rapidly evaluate the gas adsorption process to directly determine the CO_2 enthalpy of interaction.[22, 24] Under dry conditions, the adsorption is unimpeded and the total enthalpy of adsorption (H) is measured by the DSC in terms of the adsorbent, represented here in J/g. Using complementary isotherm measurements, the CO_2 enthalpy of adsorption (H_{CO2}) can be directly determined as opposed to the indirect isosteric heat of adsorption approach (Q_{st}). The total measured enthalpy (H) is simply a function of the CO_2 enthalpy of adsorption (H_{CO2}) and the amount of CO_2 adsorbed (n_i) through Equation 1.[15, 16, 22, 24, 31]

$$(1) \qquad H = H_{CO2}\, x\, n_i$$

The DSC signals from vacuum - 1 atm CO_2 swings for each compound are shown in Figure 8 and the CO_2 enthalpies of adsorption are listed in Table 2. In the case of CaSDB and Ni-MOF-74, we see good agreement between the enthalpy of adsorption and reported isosteric heats of adsorption at 1 atm. The complex gate-opening transition of ZIF-7 rendered Q_{st} calculations impossible, but the enthalpy of adsorption at 1 atm is very similar to CaSDB which also has an organic linker coordination adsorption mechanism. The enthalpy of adsorption before and after the transition in ZIF-7 is discussed below (**ZIF-7 Vacuum – Atmosphere Swing** section).

Using the NaX adsorption isotherm data (Figure 9), the 1 atm CO_2 enthalpy of adsorption (H_{CO2}) in NaX was found to be 14.31 kJ/mol which is much lower than the recently reported value of ~38 kJ/mol.[7] However, when Q_{st} was calculated out to such a high loading as was found here, the Q_{st} was found to drop off sharply at above 6.5 mmol/g to ~20 kJ/mol.[32]

Aside from using the total measured enthalpy to directly determine the CO_2 enthalpy of adsorptions for compounds, the total enthalpy can be used as a metric to judge performance through capacity loss after exposure to water. The CO_2 enthalpy of adsorption is a constant when experiments are repeated at the same conditions. Therefore, any loss in the measured total enthalpy arises from capacity loss and is a direct representation of performance.

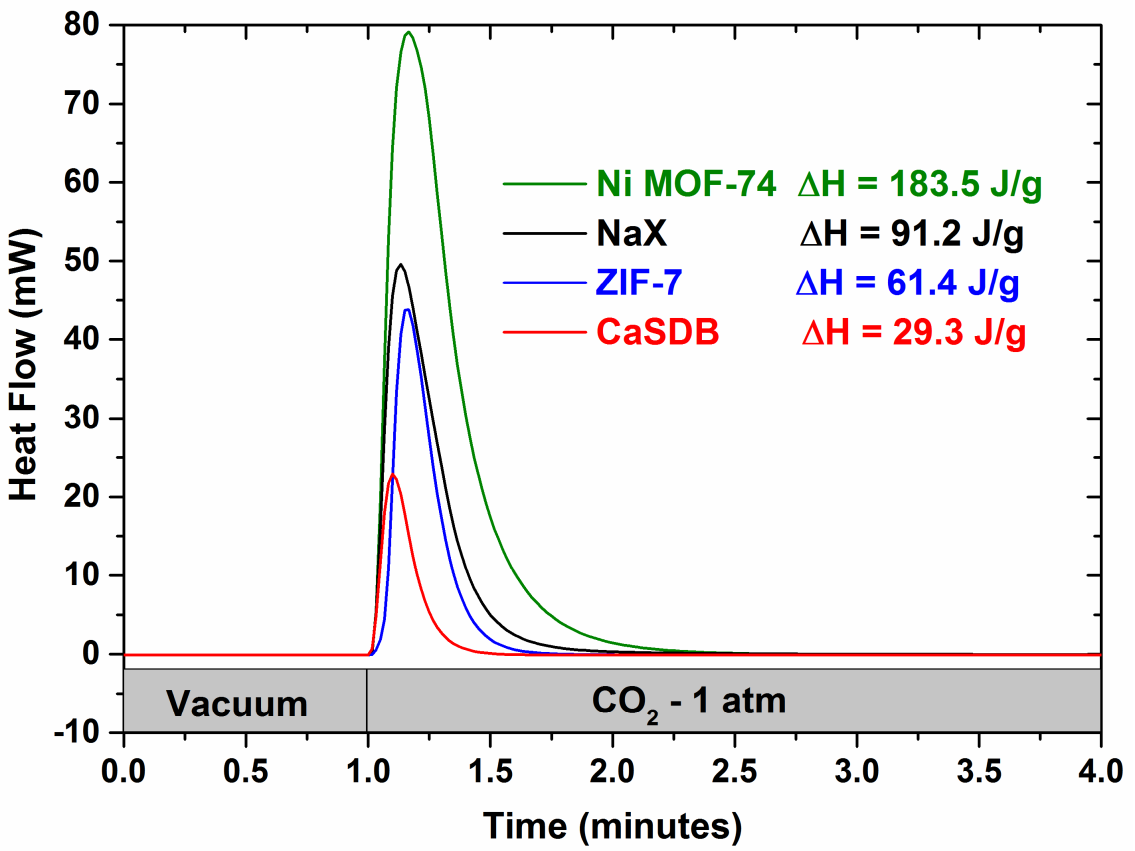

Figure 8. DSC signals from vacuum – 1 atm CO_2 swing from Ni-MOF-74 (green), NaX (black), ZIF-7 (blue), and CaSDB (red) at 22°C.

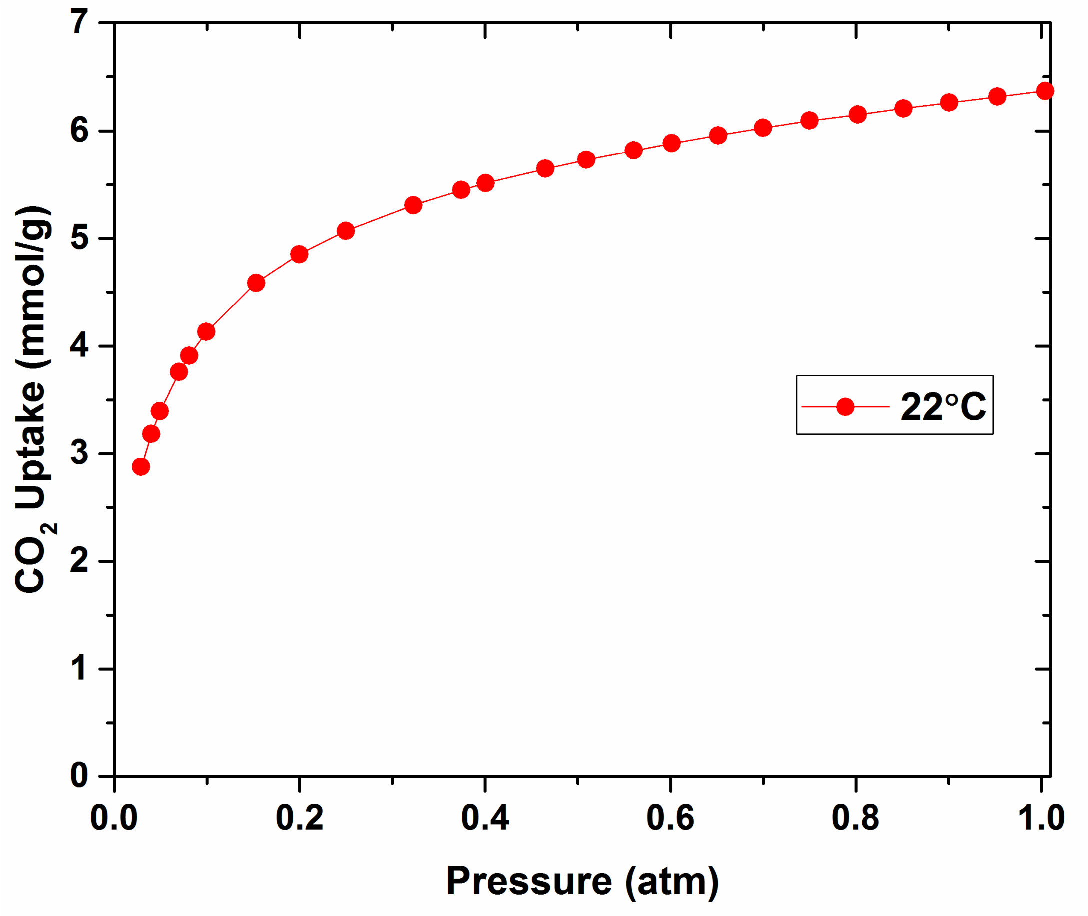

Figure 9. NaX CO_2 adsorption isotherm measured at 22°C.

Table 2. Summary of the CO_2 adsorption properties at 1 atm and 22°C for selected zeolites and MOFs

Compound	Pressure (bar)	Capacity (mmol/g)	H_{CO2} (kJ/mol)	Q_{st} (kJ/mol)	ref
CaSDB	1	0.993*	29.45	~28.5*	[25]
ZIF-7	1	2.18	27.08	-	
Ni-MOF-74	1	5.88*	31.23	27.9*	[26]
NaX	1	6.37	14.31	~38*	[7]

*25°C data taken from listed reference

Vacuum – Humid Atmosphere Swings

Vacuum – humid atmosphere swing cycles at room temperature (22°C) and 25% RH were conducted to evaluate the effect water vapor has during CO_2 adsorption in the selected microporous compounds. A RH of 25% at was chosen as the CO_2 gas stream at 1 atm will be 6.5% H_2O by volume, at the high end of flue-gas composition.[13] This experiment is comparable to humid breakthrough experiments as CO_2 and water vapor are simultaneously exposed to samples. But in the case of vacuum – humid atmosphere swings, only CO_2 is used as the influent and the process is viewed as snapshots in time to evaluate the changes in functionality and structure with respect to exposure. This mimics the exposure of the microporous compounds to flue-gas with vacuum swing CO_2 removal and subsequent re-exposure to the flue-gas without thermal reactivation. Not needing to thermally reactivate compounds between capture cycles would reduce the cost of a compound's use in post-combustion carbon capture. The cycling between vacuum and CO_2 at 1 atm allows one to correlate the structural changes with each swing and evaluate the permanent capacity loss due to water adsorption.

The performance during the successive vacuum – humid atmosphere swings is evaluated as the ratio of the measured enthalpy during 25% RH CO_2 loading to the total measured enthalpy during dry CO_2 vacuum swings (Figure 10). The adsorption of water is also an exothermic event, but the signal from water adsorption was found to be too slow and weak on the timescale of the vacuum – humid atmosphere swing, so the water adsorption exotherm contribution is negligible (**Atmosphere Swing** section below). The drop-off in performance is most significant for NaX and Ni-MOF-74, with NaX having an exponential decrease to ~30 % capacity after 23 cycles and Ni-MOF-74 linearly decreasing to ~30% capacity (Figure 10). The performance loss and XRD patterns for NaX under vacuum correlate showing water poisoning the adsorption sites which cannot be removed by re-exposure to vacuum. While not directly comparable, the observed significant performance losses of NaX and Ni-MOF-74 agree with previous breakthrough experiments which found a productivity reduction of 22% and 41% respectively, after one breakthrough cycle.[12, 21]

The initial steep performance loss in NaX (~50%) over the first 6 swings correlates with the reduction in the intensity of low angle reflections in the XRD patterns under vacuum (Figure 11) arising from the water occupying the adsorption sites. The intensity change in the XRD patterns under vacuum from swings 6-23 is gradual just like the performance loss. The XRD patterns collected under the CO_2 atmosphere (Figure 11) show a slight and gradual change in intensities as more H_2O occupies the adsorption sites alongside CO_2. The NaX XRD patterns under vacuum and CO_2 are compared during swings 1 and 23 in Figure 12 which show the patterns become similar during the process as the sites are poisoned and the capacity is reduced to ~30% of the original.

On the other hand, the XRD patterns of Ni-MOF-74 do not correlate with performance as ideally as NaX. While the performance decline of Ni-MOF-74 is nearly linear until swing 25, the XRD patterns collected under vacuum show a steep change to swing 10, and a more gradual change in relative intensities until the final swing cycle (Figure 13). The XRD patterns for Ni-MOF-74 under a CO_2 atmosphere show the most change in the first 15 swings, and thereafter remain unchanged until the final swing cycle. While comparison of XRD patterns from cycles 1 and 35 (Figure 14) show similar intensities, as expected from water occupying the adsorption site, the trends in performance loss and changes in XRD intensity does not match. The trend discrepancy may arise from some bulk sites being preferentially poisoned at first, and surface site poisoning later preventing bulk CO_2 adsorption. The discrepancy could also be explained by the formation of formic or carbonic acid in the pores, which would impact the XRD patterns. The catalysis would be more prevalent at the onset of the H_2O/CO_2 expose with gradual changes occurring after equilibrium in the XRD patterns as water slowly poisons the adsorption sites. Though such a catalysis in MOFs is rare, the catalysis event occurs at unsaturated metal sites.[33-36] Further investigation is needed to elucidate the cause of the Ni-MOF-74 results. Ideally, *in situ* structural studies at a synchrotron or neutron source could be conducted in conjunction with IR spectroscopy or gas chromatography-mass spectroscopy to evaluate the products resulting from possible reactions of species in the pores.

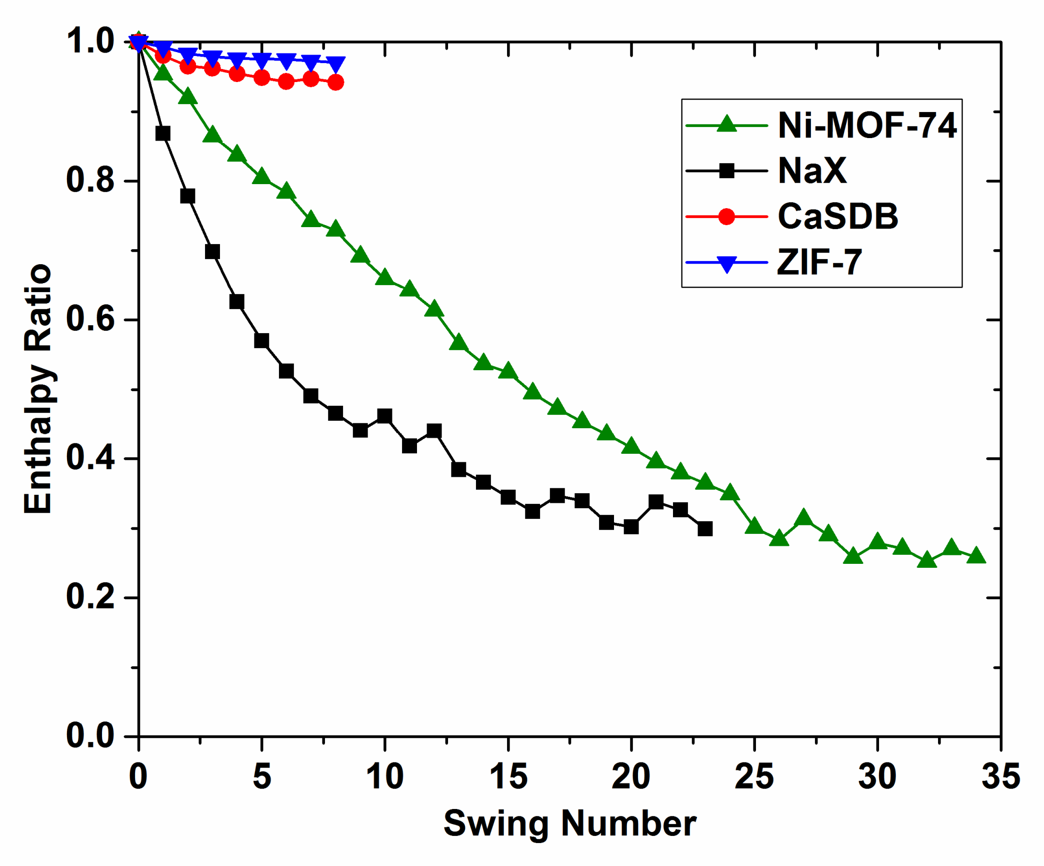

Figure 10. The measured enthalpy ratios of successive vacuum – CO_2 gas loading swings (1 atm) at 25% relative humidity and 22°C for CaSDB (red), ZIF-7 (blue), Ni-MOF-74 (green), NaX (black).

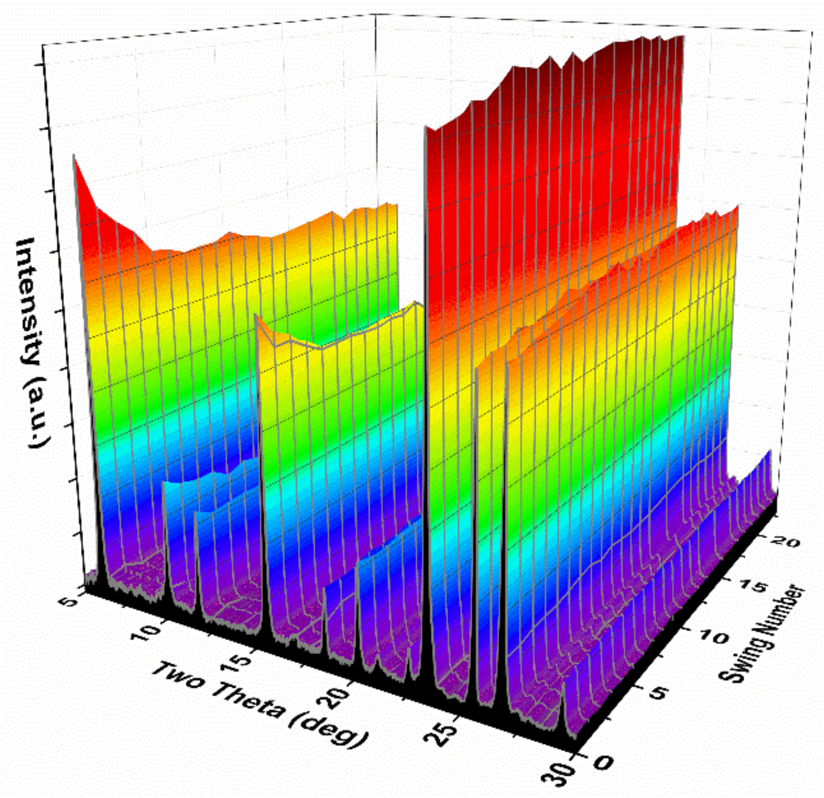

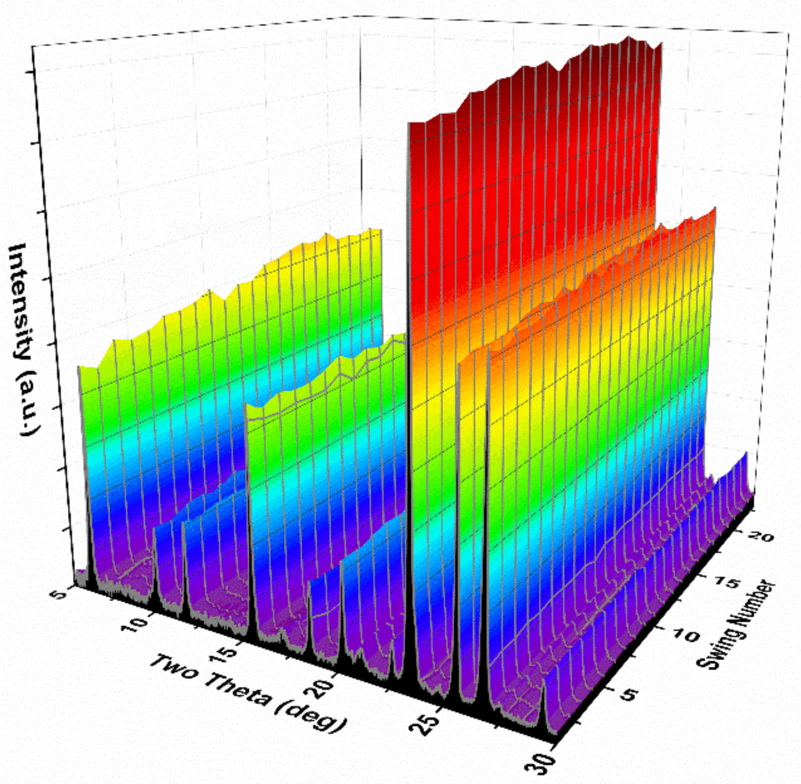

Figure 11. Successive XRD patterns of NaX under vacuum (top) and 25% RH CO_2 (bottom) during vacuum – humid 1 atm CO_2 swings.

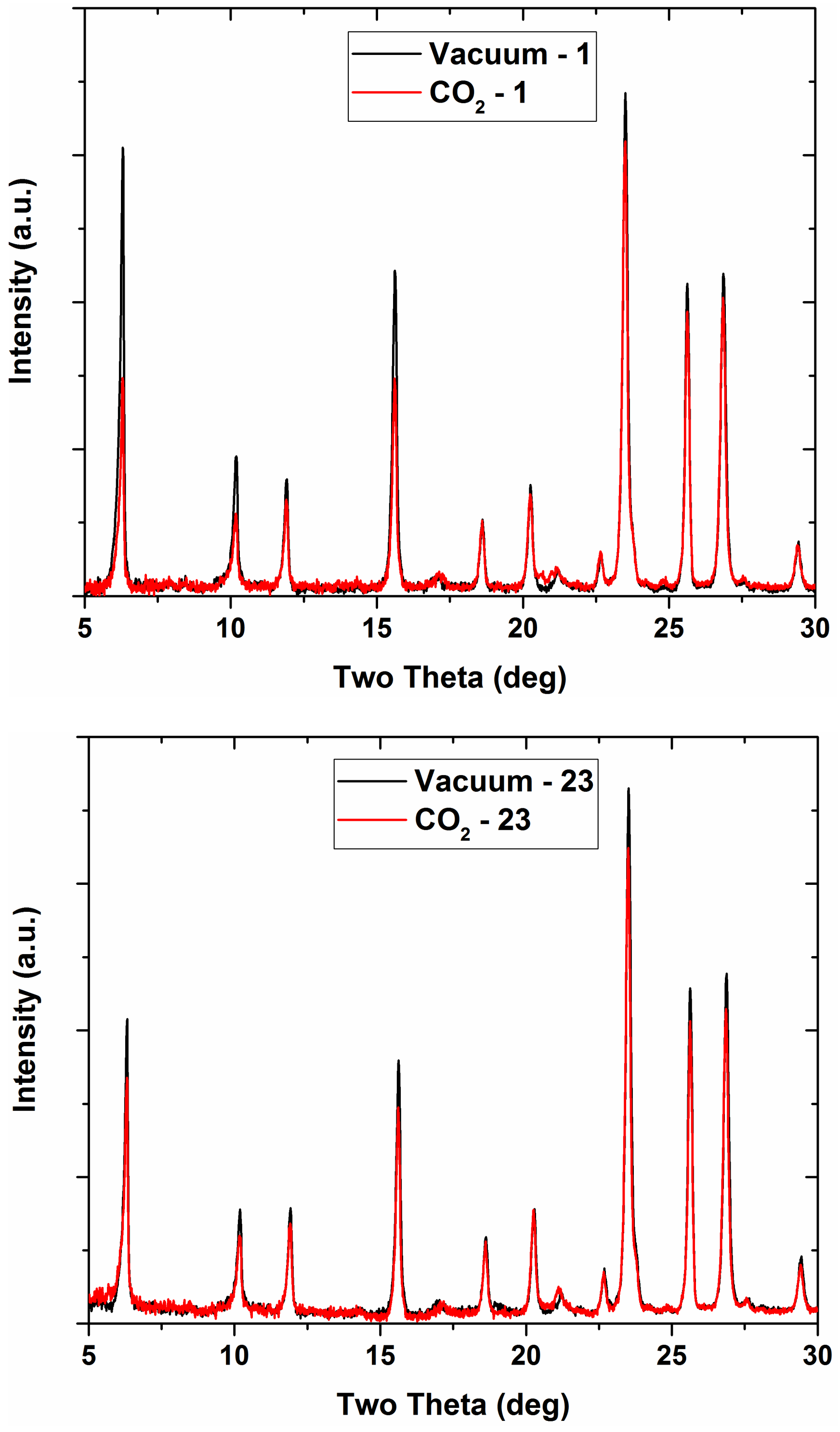

Figure 12. Comparison of the NaX XRD patterns collected under vacuum and 25% RH CO_2 during cycle 1 (top) and cycle 23 (bottom).

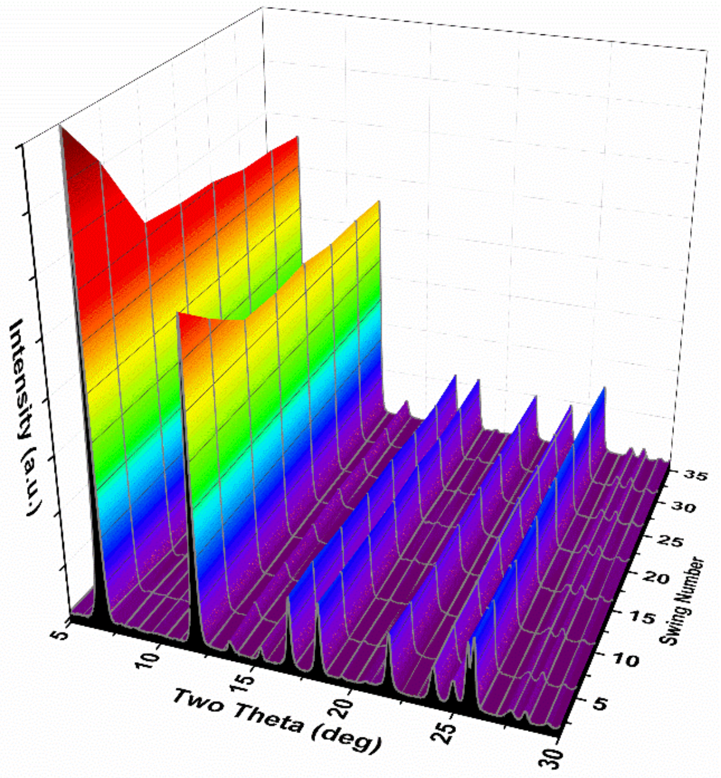

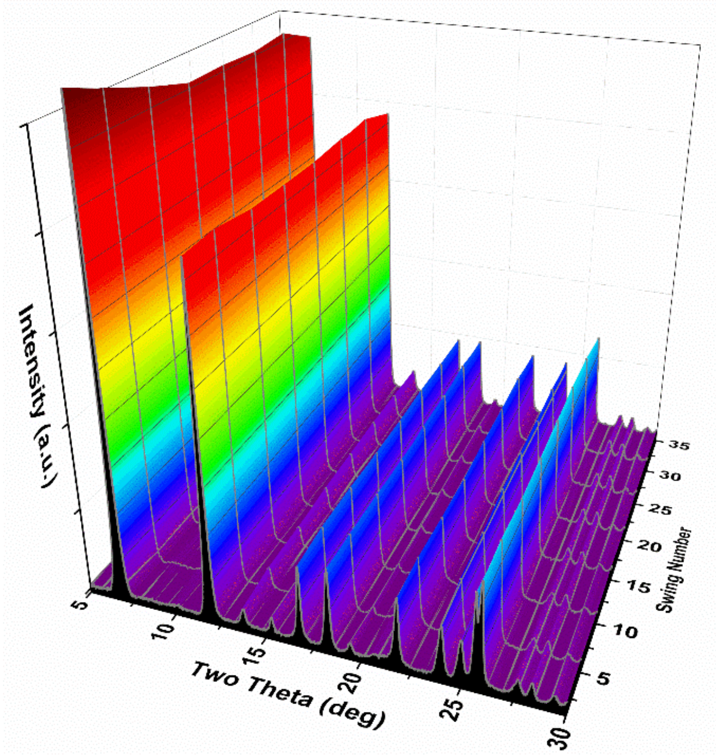

Figure 13. Successive XRD patterns of Ni-MOF-74 under vacuum (top) and 25% RH CO_2 (bottom) during vacuum – humid 1 atm CO_2 swings.

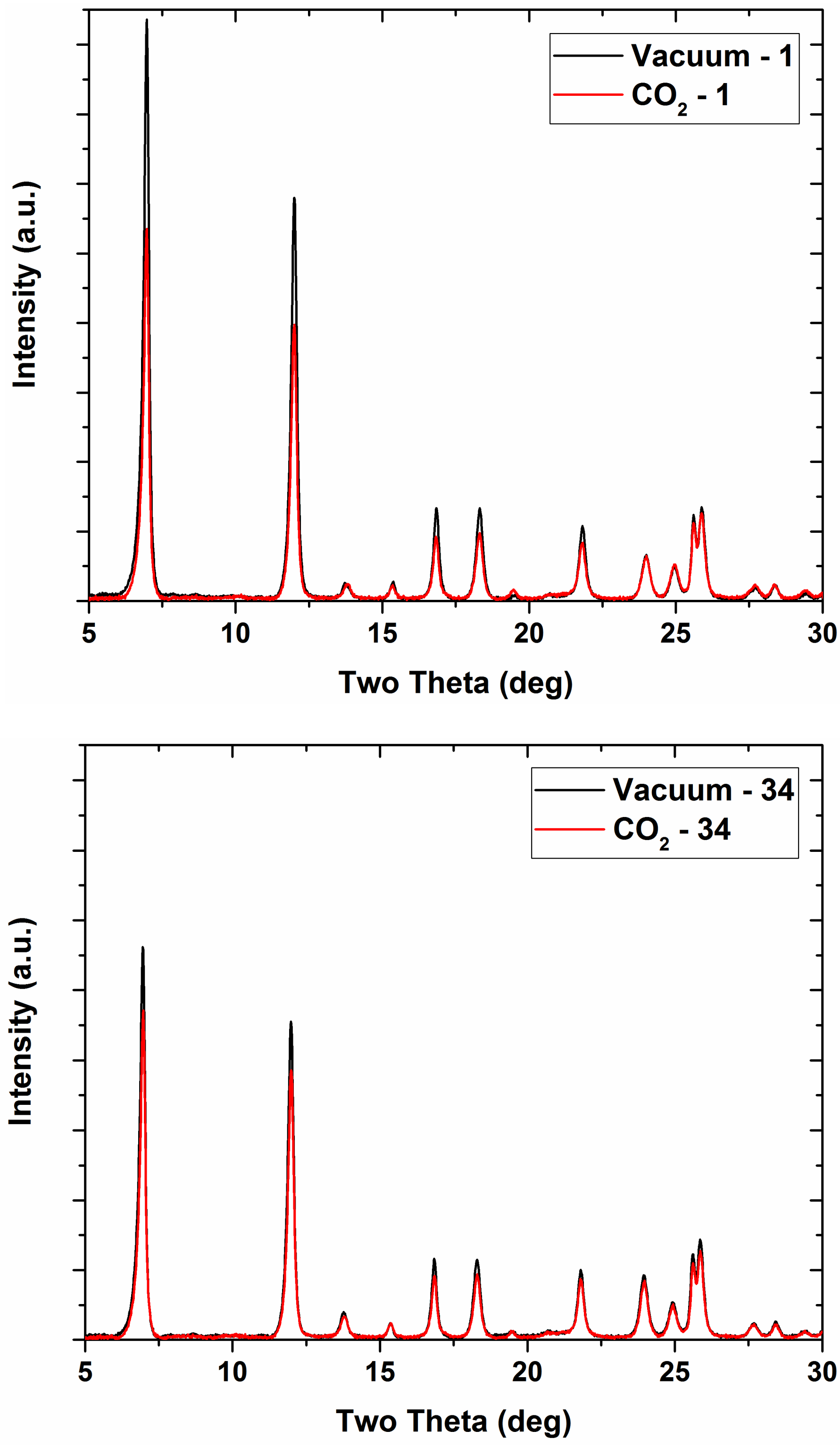

Figure 14. Comparison of the Ni-MOF-74 XRD patterns collected under vacuum and 25% RH CO_2 during cycle 1 (top) and cycle 34 (bottom).

At 25% RH, the presence of water vapor has very little effect on ZIF-7 and CaSDB, which show gradual drops to ~97% and ~95% of the dry total enthalpy over the course of 8 swing cycles respectively. Additional vacuum – humid atmosphere swings were conducted at 75% RH to evaluate the effects of higher moisture content. At 75% RH, both ZIF-7 and CaSDB experience a steep decrease in enthalpy in the initial swings (Figure 15) with ZIF-7 gradually decreasing to ~85% of the dry enthalpy by cycle 12. The XRD patterns for ZIF-7 collected during the swing cycles reflect the trends seen in the enthalpy data (Figure 16). The XRD patterns of ZIF-7 collected under vacuum show a sharp change after the first 2 cycles and then a gradual change in reflection intensities until the final swing cycle. The XRD patterns collected under 75% RH CO_2 show minimal changes from cycle to cycle as the pores are still predominantly occupied by CO_2.

However, CaSDB displays very different behavior from ZIF-7 during the 75% RH CO_2 cycles. After the initial performance decrease to ~85%, the enthalpy spikes at swings 6 and 10, and this correlates with significant changes in the vacuum XRD patterns (Figure 17). The CaSDB XRD patterns under 75% RH CO_2 show a sharp decrease in low angle reflection intensity during the first two cycles, and after cycle 6 the relative intensity of other reflections increase. The CaSDB results are enigmatic in comparison to NaX, Ni-MOF-74, and ZIF-7 which all demonstrate correlated changes in performance and XRD patterns as expected from water poisoning the adsorption sites.

The co-adsorption of H_2O and CO_2 in CaSDB does not appear to follow the straightforward trend of water simply poisoning the adsorption sites and indicates there may be a secondary interaction. The formation of calcium carbonate is unlikely as the CaSDB reflections remain sharp and no new reflections from calcite or other $CaCO_3$ polymorphs could be identified in the XRD patterns. The odd behavior of CaSDB during the vacuum – 75% RH CO_2 swings, like that of Ni-

MOF-74 at 25% RH, could be explained by an interaction between CO_2 and H_2O which could both significantly alter the XRD patterns and the DSC signal. Though as mentioned earlier, such a reaction in the pore has only been observed in MOFs with unsaturated metal sites. It is also possible that the presence H_2O in the pores is causing some of the organic linkers in CaSDB to rotate 45° back to the position in as-synthesized CaSDB phase where H_2O occupies the channels. The lattice of the as-synthesized and activated CaSDB phases are nearly identical so linker rotation would only impact the intensities of reflections and not the positions.[25] Such an event could also cause aberrations in the DSC data if the application of vacuum were able to correct the linker rotation by impacting the H_2O adsorption. As is the case for Ni-MOF-74, further *in situ* structural studies are needed to understand the changes in the XRD patterns.

While interpretation of the DSC signal from vacuum - humid CO_2 swings allowed evaluations of CO_2 adsorption performance for the selected microporous compounds in the presence of water vapor, the XRD patterns offered additional insights into structural changes associated with gas sorption and desorption. The performance of NaX and Ni-MOF-74, the compounds with unsaturated metal sites after activation were most impacted by the presence of water vapor during CO_2 adsorption with measured total enthalpy reductions to ~30% after vacuum - 25% RH CO_2 swings. The compounds with organic linker coordination adsorption mechanisms, CaSDB and ZIF-7, are less impacted by the presence of water vapor during CO_2 adsorption. Even at 75% RH, CaSDB and ZIF-7 resistant to water vapor with a gradual performance loss of ~18% over 12 swing cycles. While the XRD patterns of each cycle offered insight to the structural changes due to water impeding CO_2 adsorption, not all of the XRD data are able to elucidate the cause of performance changes in the compounds.

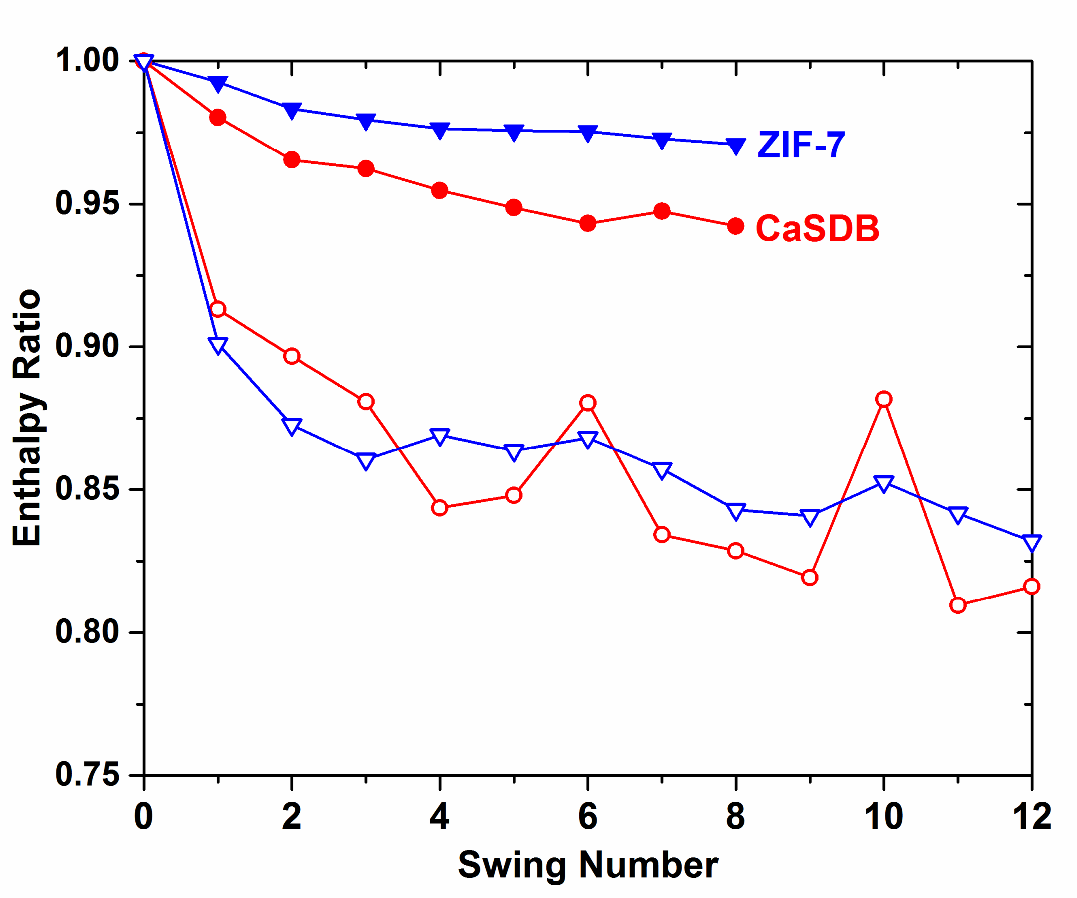

Figure 15. The enthalpy ratios of successive vacuum – 1 atm CO_2 gas loading swings at 25% (closed symbols) and 75% (open symbols) RH for CaSDB (red), ZIF-7 (blue) at 22°C.

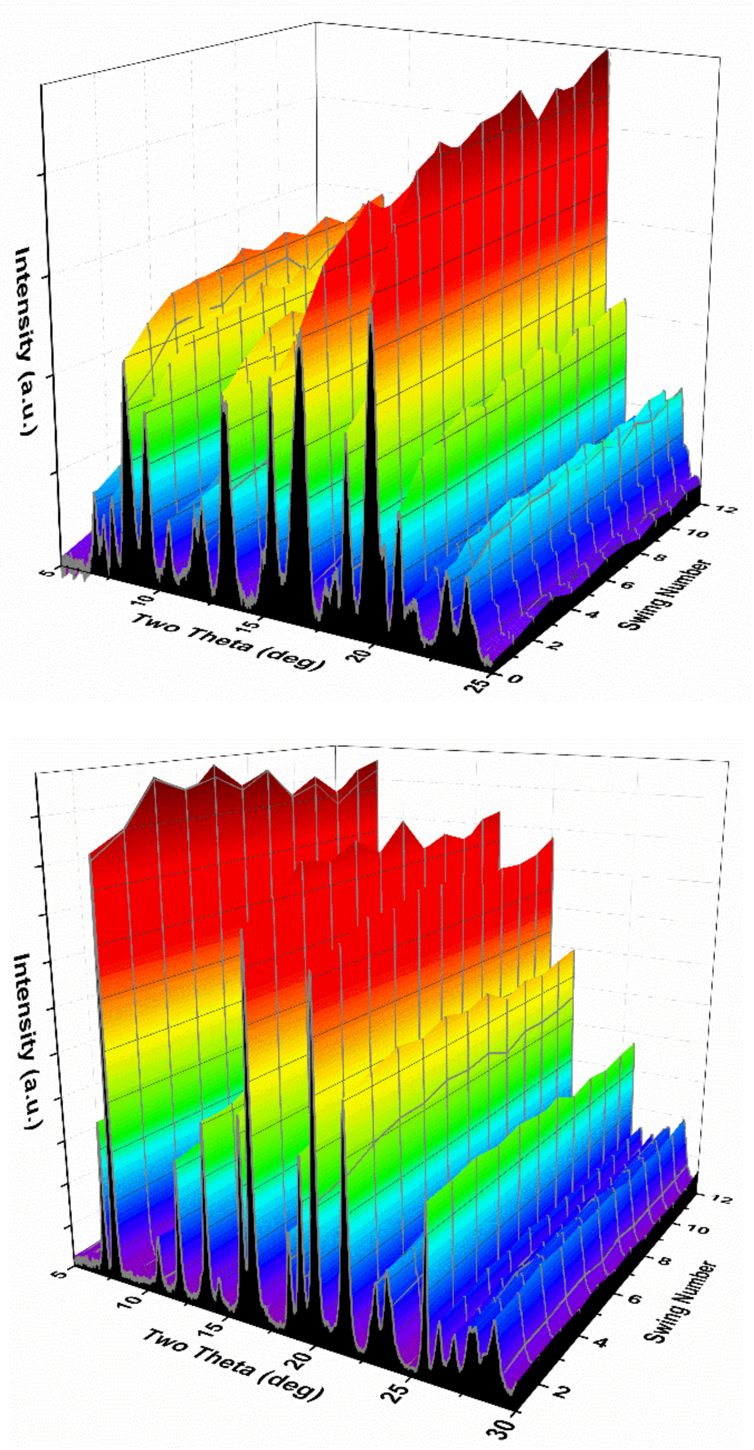

Figure 16. Successive XRD patterns of ZIF-7 under vacuum (top) and 75% RH CO_2 (bottom) during vacuum – humid 1 atm CO_2 swings.

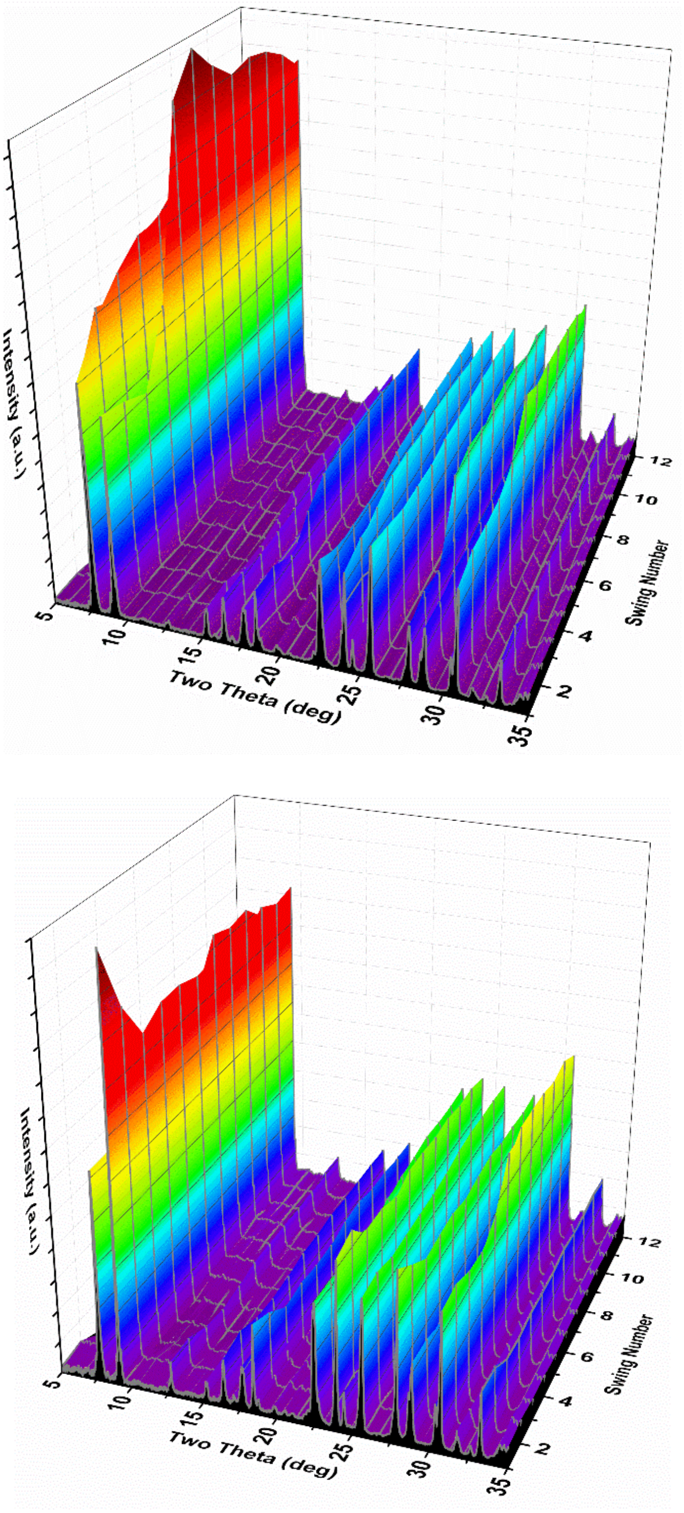

Figure 17. Successive XRD patterns of CaSDB under vacuum (top) and 75% RH CO_2 (botttom) during vacuum – humid 1 atm CO_2 swings.

ZIF-7 Vacuum – Atmosphere Swings

Additional vacuum – humid CO_2 swing experiments were conducted as a function of pressure to 1 atm with ZIF-7 to understand the effect water vapor has on adsorption/desorption hysteresis of the guest induced gate-opening transition.[28] The effect of temperature on the CO_2 adsorption of ZIF-7 is well known, as the onset pressure of the gate opening and degree of hysteresis both increase with temperature.[28] However, the effect water vapor has on the ZIF-7 gate-opening transition during CO_2 adsorption has not been studied. To evaluate what effect the presence of water vapor has on ZIF-7 during CO_2 adsorption, vacuum – atmosphere swings were performed so as to mimic adsorption/desorption isotherms under dry and 75% RH conditions. Under both dry and 75% RH CO_2 conditions, ZIF-7 was titrated with CO_2 in 0.1 atm intervals from vacuum to 1 atm and back to vacuum while collecting XRD patterns at each pressure point. The DSC signal from the pressure series under dry conditions is shown in Figure 18. The enthalpy at each pressure point is plotted as the cumulative sum of the enthalpy to that pressure point, in the same manner as an adsorption isotherm is reported. Each point on the adsorption curve is therefore the enthalpy that would be measured during a vacuum – atmosphere swing to that pressure point. Each point on the desorption curve is the enthalpy that would be measured in going from vacuum to 1 atm CO_2 and then to the plotted pressure point.

The measured cumulative enthalpy adsorption/desorption curves display the same shape and hysteresis as isotherm measurements (Figure 19). The presence of water vapor not only reduces the measured enthalpy and therefore capacity of ZIF-7 (85.2% of dry), it shifts the onset of the gate opening and closing by +0.1 atm (Figure 20). The performance reduction is similar to what is found after 10 cycles of vacuum – 75% RH CO_2 swings (Figure 15). As there is no deviation from the adsorption curve, the gate opening transition does not contribute any additional energy during the adsorption. Due to the complex adsorption process involving the gate-opening transition, the CO_2 enthalpy of adsorption could not be estimated using Q_{st} techniques and isotherm experiments. The ZIF-7 CO_2 enthalpy of adsorption was determined using Equation 1 with the measured total enthalpy results and adsorption isotherm measurements (Figure 21) and is plotted in Figure 22 as a function of CO_2 loading. Prior to the gate opening, the CO_2 enthalpy of adsorption of ~ 11 kJ/mol which subsequently jumps to ~ 27 kJ/mol after the gate-opening transition.

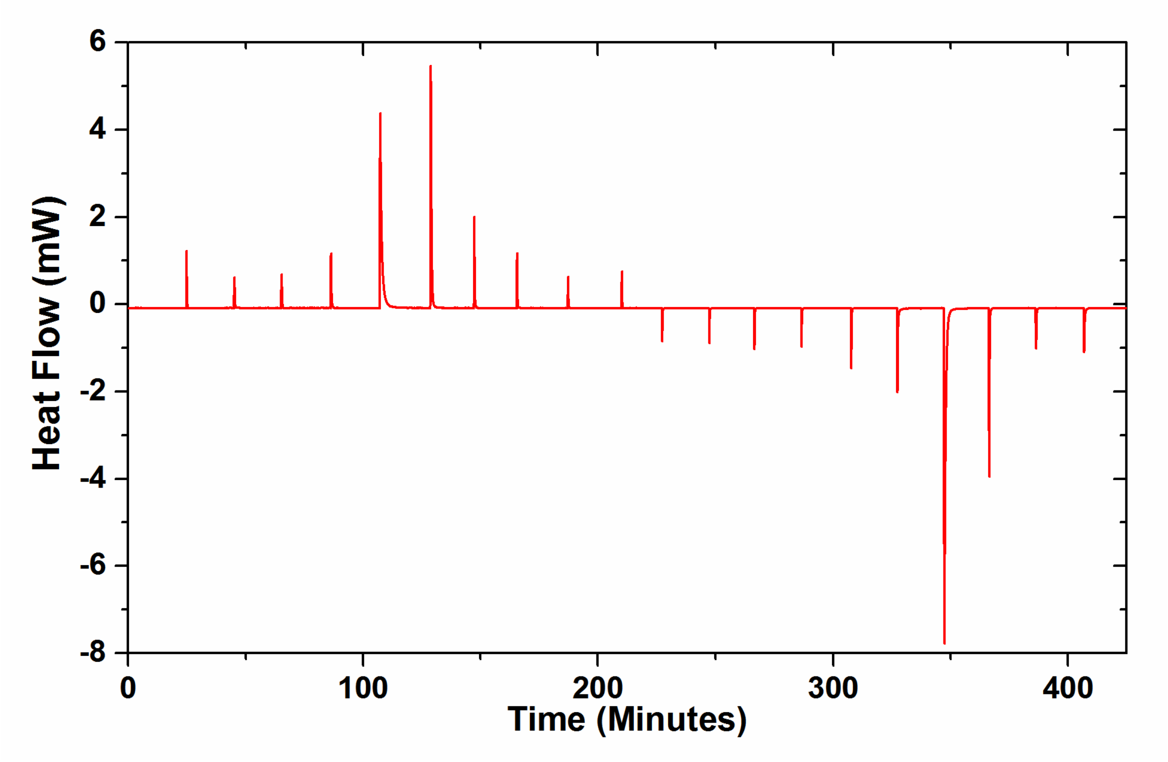

Figure 18. The continuous DSC signal from increasing pressure of dry CO_2 at 0.1 atm intervals going from vacuum to 1 atm, and back to vacuum on 11 mg of ZIF-7. Each peak is from the 0.1 atm pressure change during adsorption/desorption of CO_2 in ZIF-7.

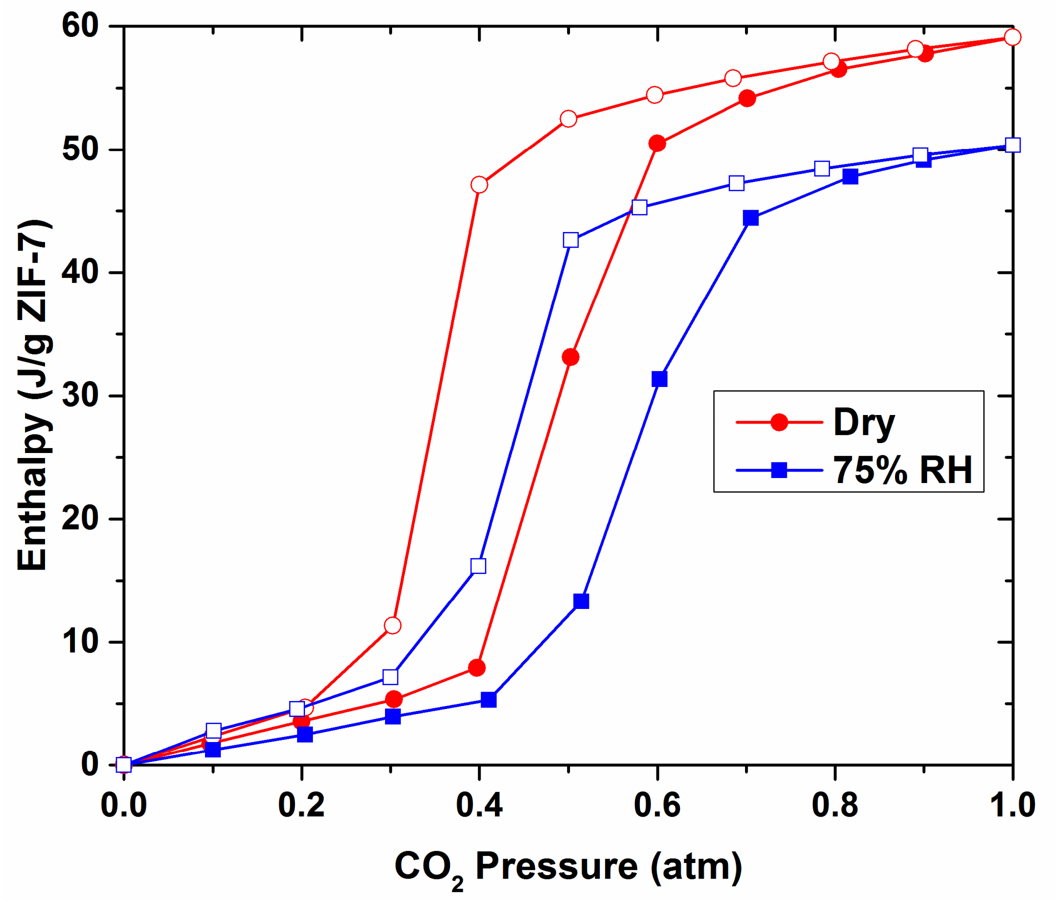

Figure 19. Cumulative measured enthalpy plot of ZIF-7 during CO_2 adsorption – desorption with the XRD-DSC under dry (red) and 75% RH (blue) conditions. Closed symbols are from enthalpy measurements during adsorption and open symbols are from desorption enthalpy measurements.

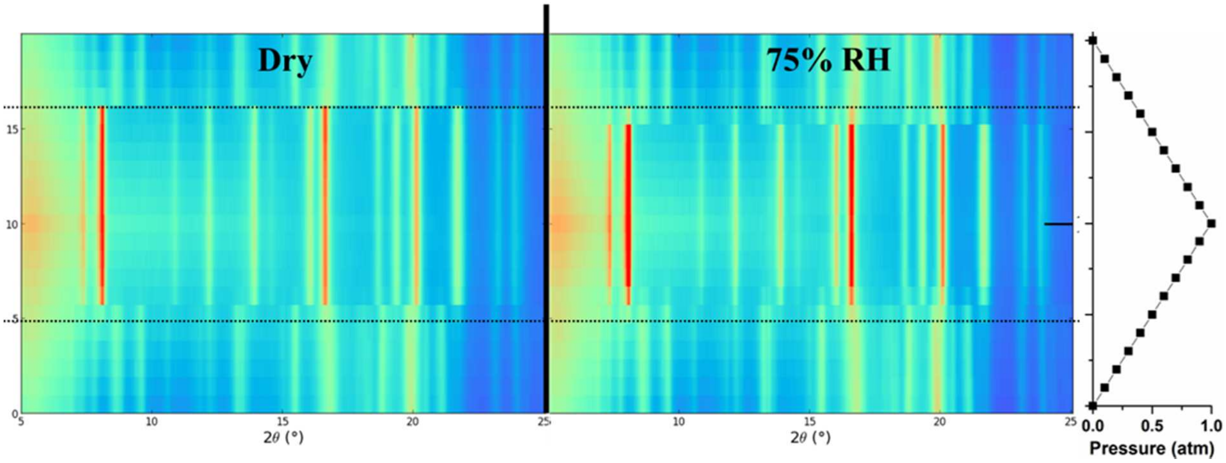

Figure 20. The 2D Powder XRD patterns of ZIF-7 during the 0.1 atm titration of CO_2 under dry (left) and 75% RH conditions (middle) as a function of pressure (right). Going from the bottom to the top of the figure, the pressure of CO_2 atmosphere on the sample during the XRD collection increases at 0.1 atm intervals until 1 atm is reached; at which point pressure decreases 0.1 atm in successive patterns until vacuum. Dashed lines are drawn to highlight the 0.1 atm pressure shift in the gate-opening transition.

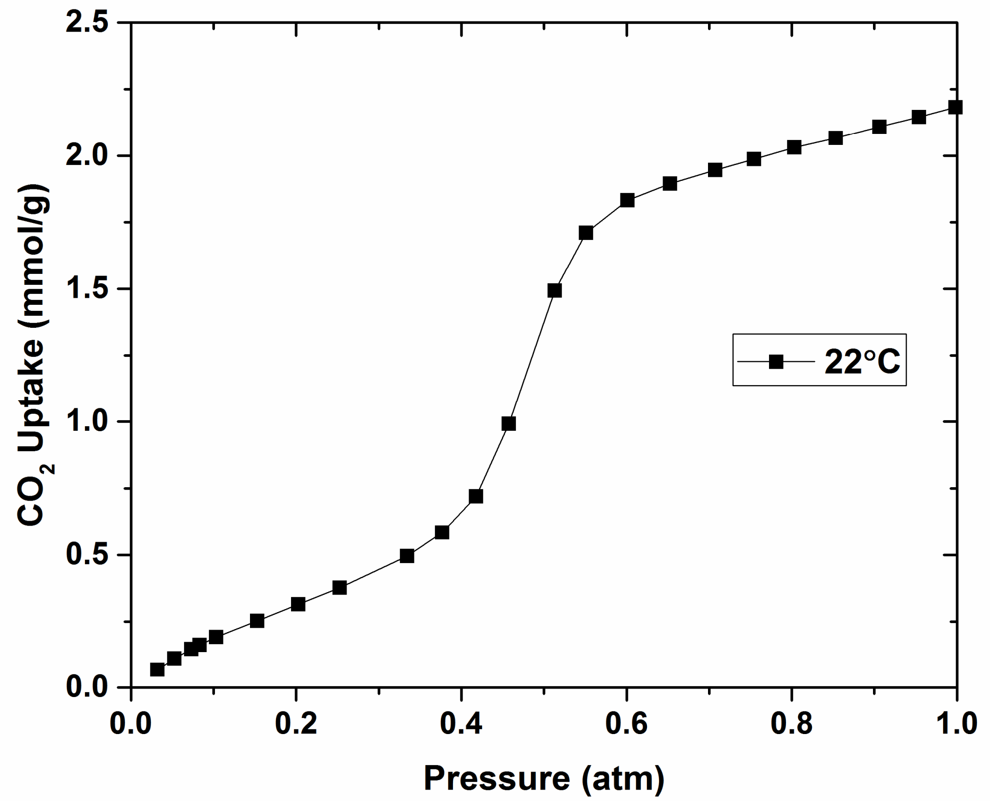

Figure 21. ZIF-7 CO$_2$ adsorption isotherm collected at 22°C.

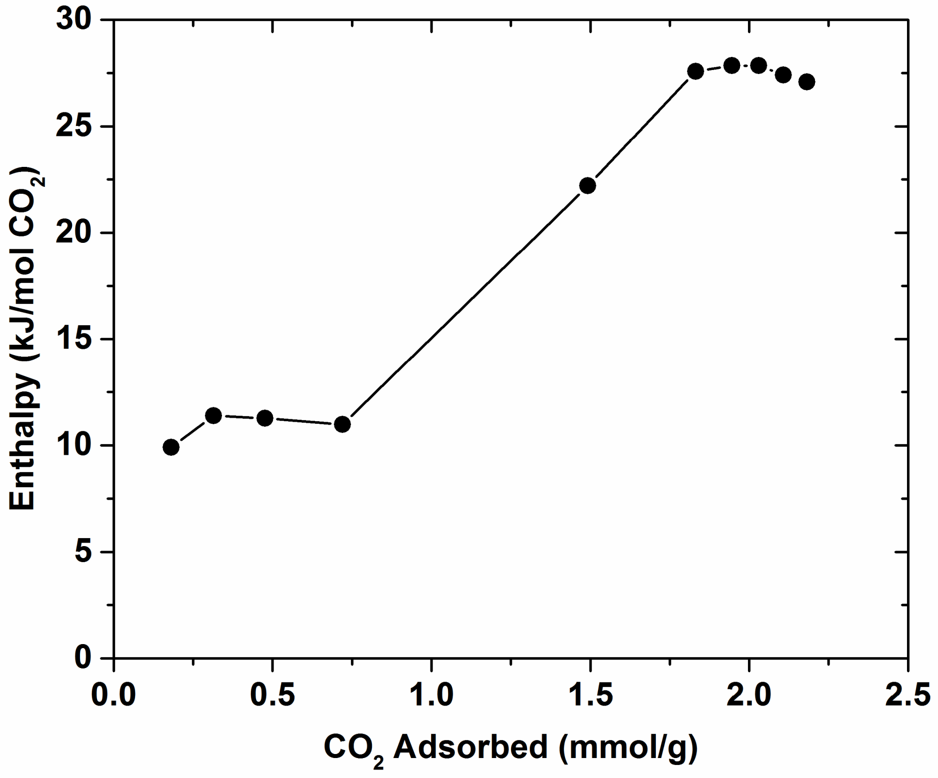

Figure 22. ZIF-7 CO_2 enthalpy of interaction as a function of CO_2 loading.

Atmosphere Swing

Humid flowing atmosphere swings from 25% RH helium to 25% RH CO_2 were conducted as a means to measure the changes in adsorption capacity after constant exposure to water vapor. This is a complementary technique to isotherm experiments where the adsorbent is first exposed to a humid gas stream before the isotherm measurements to quantify capacity loss from water poising the adsorption site. Helium was chosen as the carrier gas as it has a negligible enthalpy of adsorption and low X-ray scattering power so that pore occupation by helium would have minimal impact on the XRD patterns. Each sample was first activated *in situ* and kept under vacuum at room temperature, then exposed to flowing (150 ml/min) 25% RH helium for a minimum of 3 hours before switching the atmosphere to 25% RH CO_2. The reduction in adsorption capacity is determined from the difference in the measured differential enthalpies between helium and CO_2 under dry conditions and after exposure to 25% RH helium (Table 3). The Ni-MOF-74 sample had slower water adsorption than the other samples and was kept under flowing 25% RH helium for 7 hours until equilibrium was reached. The DSC signal of each sample is shown in Figures 23, 25, 27, and 29 with the corresponding XRD patterns shown in Figures 24, 26, 28, and 30.

The prolonged exposure to water vapor had the greatest impact on Ni-MOF-74 and NaX. After transitioning from vacuum to 25% RH helium, both compounds exhibit large exotherms arising from water adsorption. In both cases, the adsorption of water into the pore was an energetic and slow process that lasted ~350 min for Ni-MOF-74 and ~150 min for NaX (Figures 23 and 25). The adsorption of water in the pores of NaX and Ni-MOF-74 significantly reduced the enthalpy of the following CO_2 swings, being only 5.46% and 3.38% of the respective dry He – CO_2 values. However, in the case of CaSDB and ZIF-7, the organic linker coordinating adsorbents, no exotherms are produced during the prolonged exposure to 25% RH helium flow (Figures 27 and

29). The subsequent swing to 25% RH CO_2 produced enthalpies that were 64.16% and 79.02% of the dry He-CO_2 differential enthalpies for CaSDB and ZIF-7 respectively.

The atmosphere swing results are in agreement with previous studies utilizing isotherm adsorption experiments after exposing compounds to humid environments. The CaSDB results are in line with previous XRD-DSC studies showing CaSDB retains capacity even after exposure to 75% RH atmospheres.[16] The previous isotherm studies found ZIF-7 to be resistive to water vapor as it had only a 2% drop in capacity after exposure to 8.3% RH air at 12°C.[19] The reduction of Ni-MOF-74 capacity to 3.38% after exposure at 25% RH displays the same trend that found Ni-MOF-74 capacity approaches zero at 90% RH.[30]

The companion XRD patterns of the atmosphere swings give additional insight into the water adsorption and humid CO_2 capture performance. The XRD patterns comparing activated NaX, Ni-MOF-74, and ZIF-7 under vacuum wand 1 atm dry helium atmosphere (Figures 24, 26, and 30) are virtually indistinguishable while the dry helium CaSDB pattern shows a slight reduction in reflection intensities (Figure 28). From the comparison figures, we can conclude helium has only a minor effect on the XRD patterns. However, significant changes in relative intensity are observed in Ni-MOF-74 and NaX when comparing the XRD patterns of the dry helium atmosphere with those after the 25% RH helium exposure. As helium has virtually no effect on the pattern, the resulting decrease in reflection intensities under 25% RH can only be attributed to water occupying the adsorption sites which is in agreement with the DSC data. The Ni-MOF-74 and NaX XRD patterns of the subsequent 25% RH CO_2 swings have only minor intensity differences with the 25% RH helium pattern as the adsorption sites were almost entirely occupied by water thus only allowing a small amount of CO_2 to be adsorbed. In contrast, modest changes are observed in CaSDB and ZIF-7 XRD patterns after exposure to 25% RH He pursuant to the moderate adsorption of water. Furthermore, significant changes in the CaSDB and ZIF-7 XRD patterns are observed after the 25%RH CO_2 swing as the majority of the adsorption sites are still unoccupied and able to adsorb CO_2.

The humid atmosphere swings show a stark difference in the adsorption performance of compounds with unsaturated metal sites versus that of organic linker coordination. After exposure to water vapor, the adsorption performance of Ni-MOF-74 and NaX is significantly reduced while CaSDB and ZIF-7 still retain most of their functionality. The unsaturated metal sites have a strong affinity for water as evidenced by the presence of large water adsorption exotherms. But the absence of water adsorption exotherms in CaSDB and ZIF-7 indicates the organic linker coordination adsorption mechanism in these compounds have a weaker interaction with water and adsorption performance is only mildly hindered by water vapor.

Table 3. Measured helium – CO_2 differential enthalpies under dry and 25% RH conditions

Compound	Dry He – CO_2 ΔH (J/g)	25% RH He – CO_2 ΔH (J/g)	Percent of Dry
CaSDB	29.25	18.77	64.16
ZIF-7	61.16	48.33	79.02
Ni-MOF-74	183.48	6.21	3.38
NaX	90.52	5.85	5.46

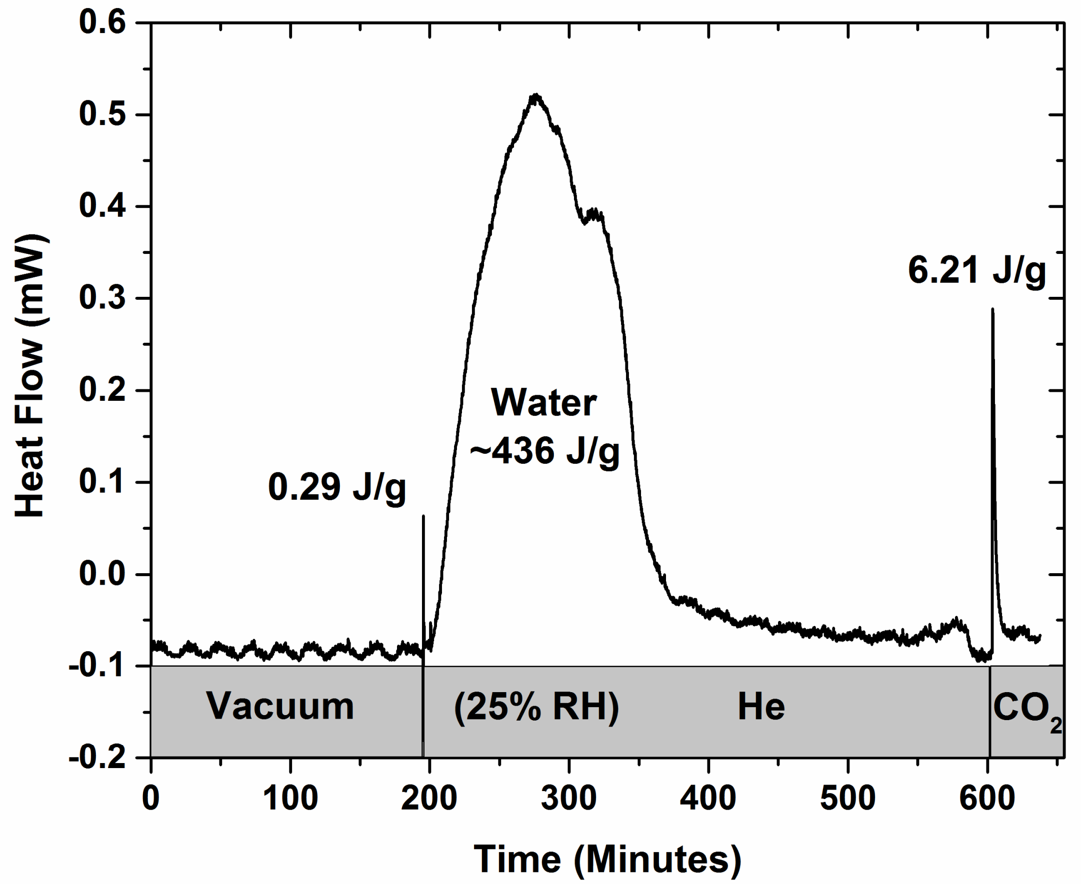

Figure 23. DSC signal during Ni-MOF-74 humid atmosphere (25% RH) swing. Activated Ni-MOF-74 under vacuum is first exposed to helium gas at 25% RH at a constant flow of 150 mL/min, then to an atmosphere of CO_2 at 25% RH. After exposure to the 25% RH helium stream, a large exotherm is observed due to the slow adsorption of water. The aberration in the signal between ~560 and 600 minutes is due to an electronic noise contribution from collecting the XRD pattern.

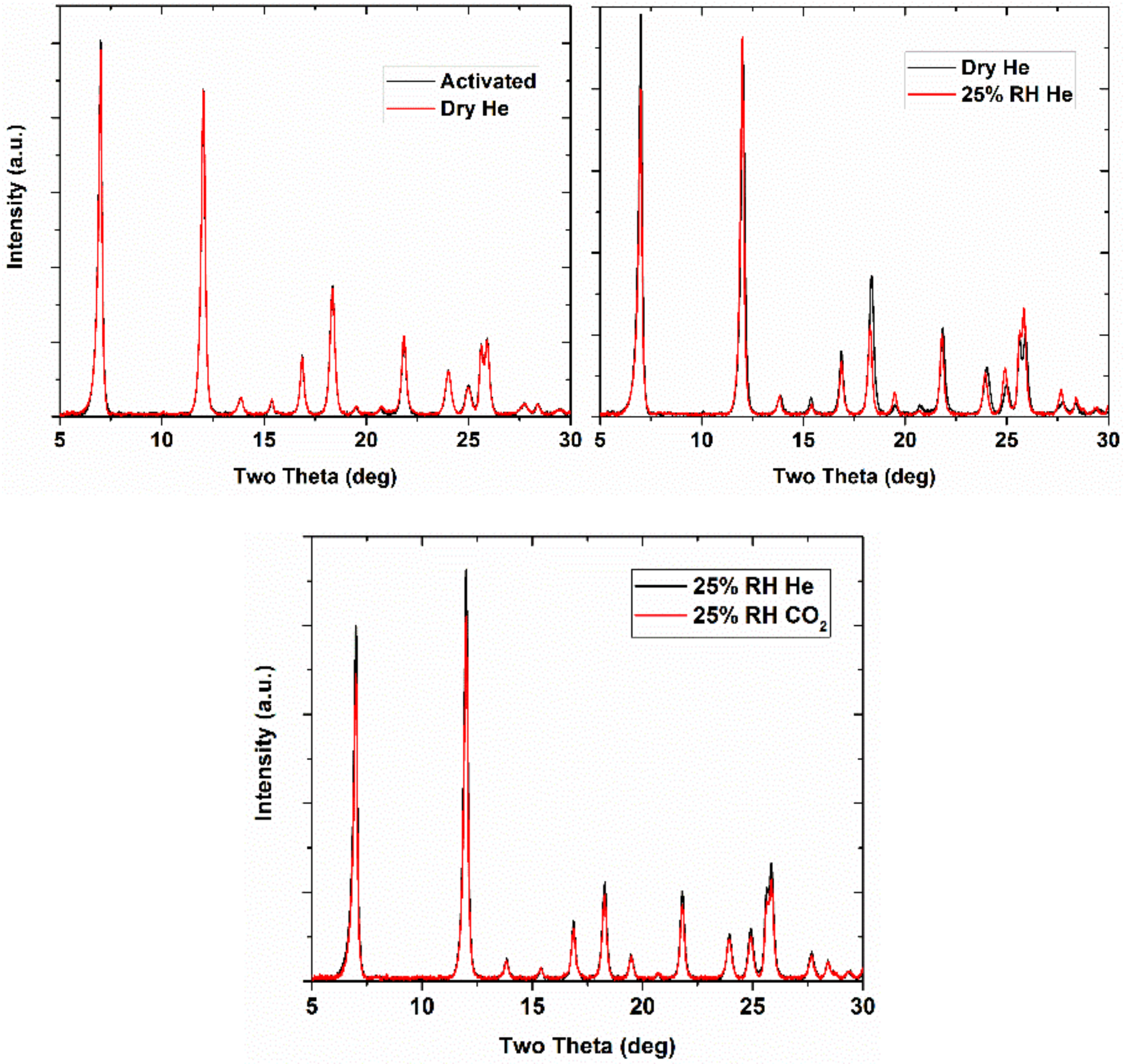

Figure 24. XRD patterns of Ni-MOF-74 under different gas loading conditions. (top left) Activated Ni-MOF-74 under vacuum vs dry helium. (top right) Ni-MOF-74 under dry helium vs after exposure to 25% RH helium. (bottom) Ni-MOF-74 under 25% RH helium vs 25% RH CO_2.

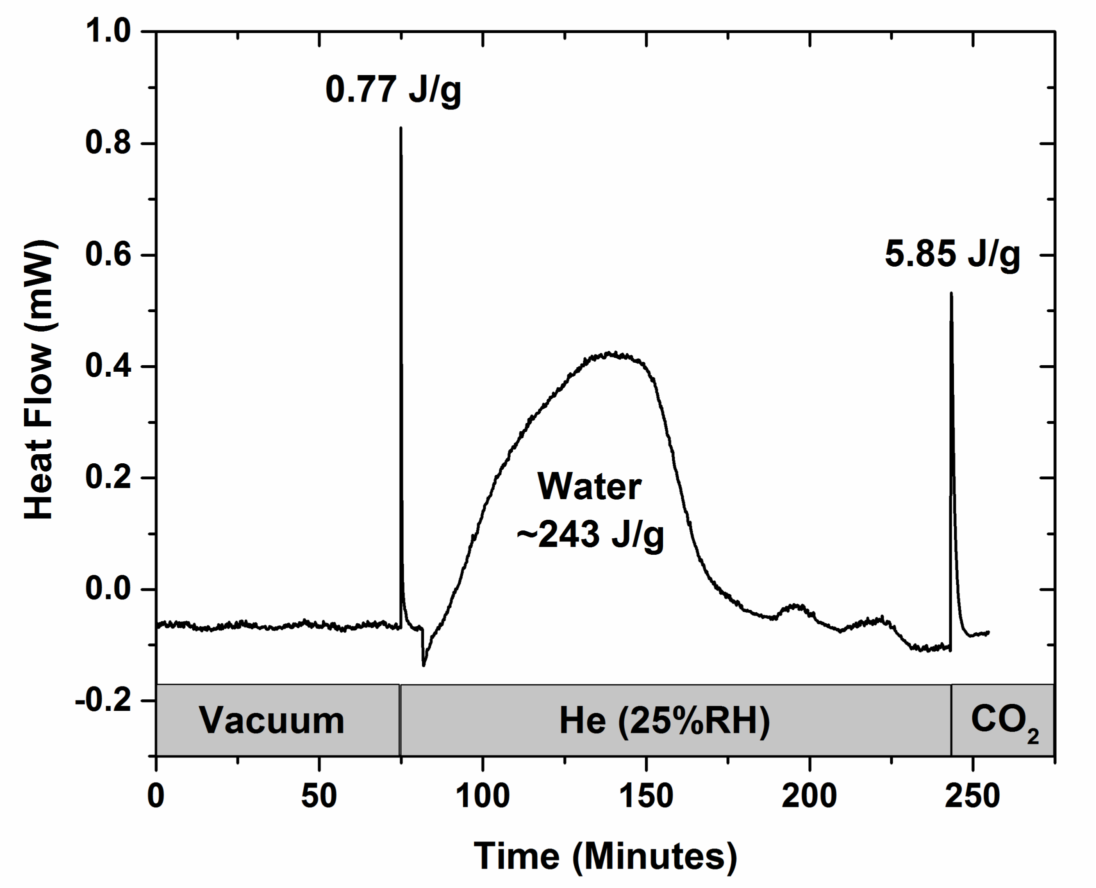

Figure 25. DSC signal during NaX humid atmosphere (25% RH) swing. Activated NaX under vacuum is first exposed to helium gas at 25% RH at a constant flow of 150 mL/min, then to an atmosphere of CO_2 at 25% RH. After exposure to the 25% RH helium stream, a large exotherm is observed due to the slow adsorption of water.

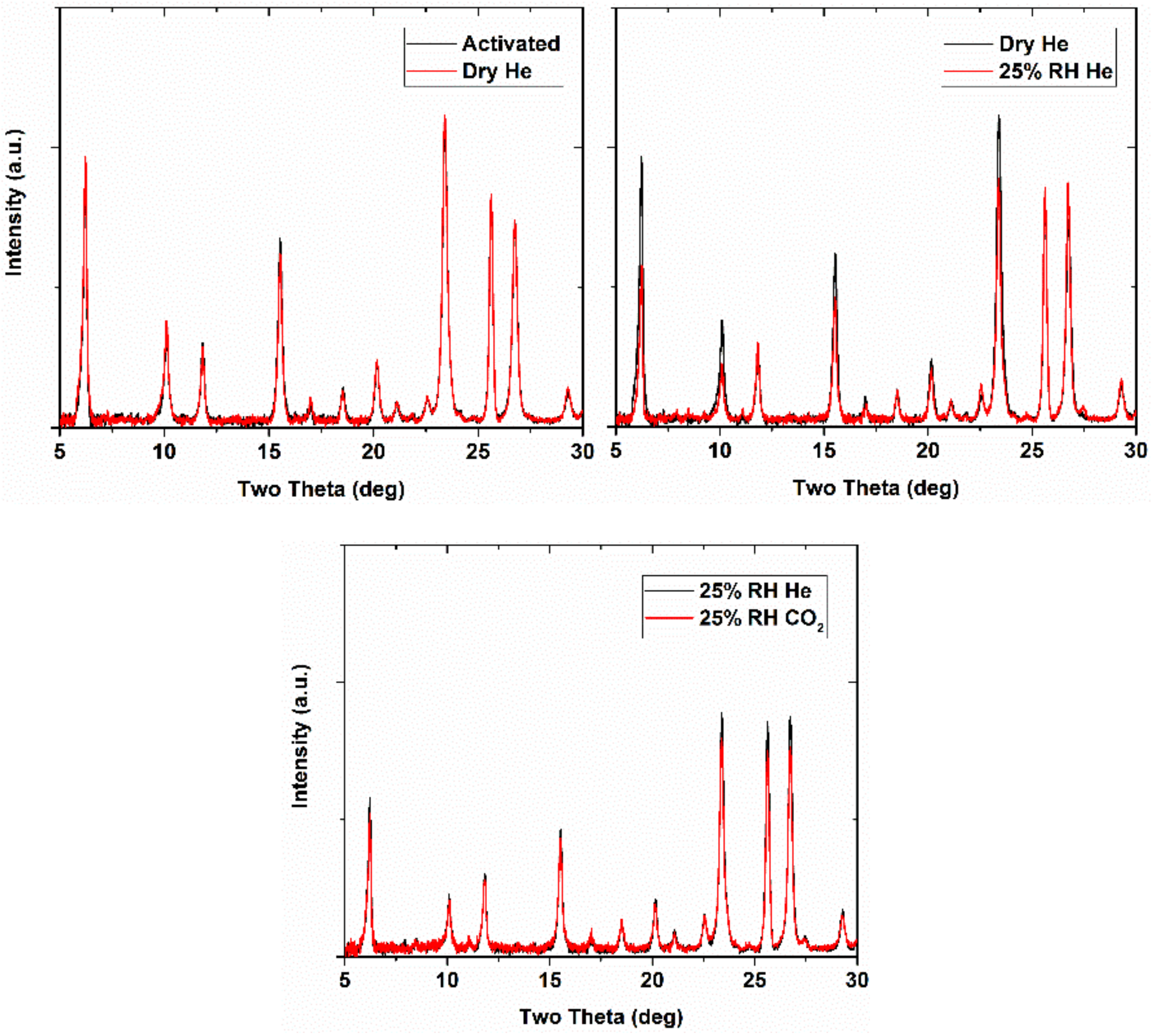

Figure 26. XRD patterns of NaX under different gas loading conditions. (top left) Activated NaX under vacuum vs dry helium. (top right) NaX under dry helium vs after exposure to 25% RH helium. (bottom) NaX under 25% RH helium vs 25% RH CO_2.

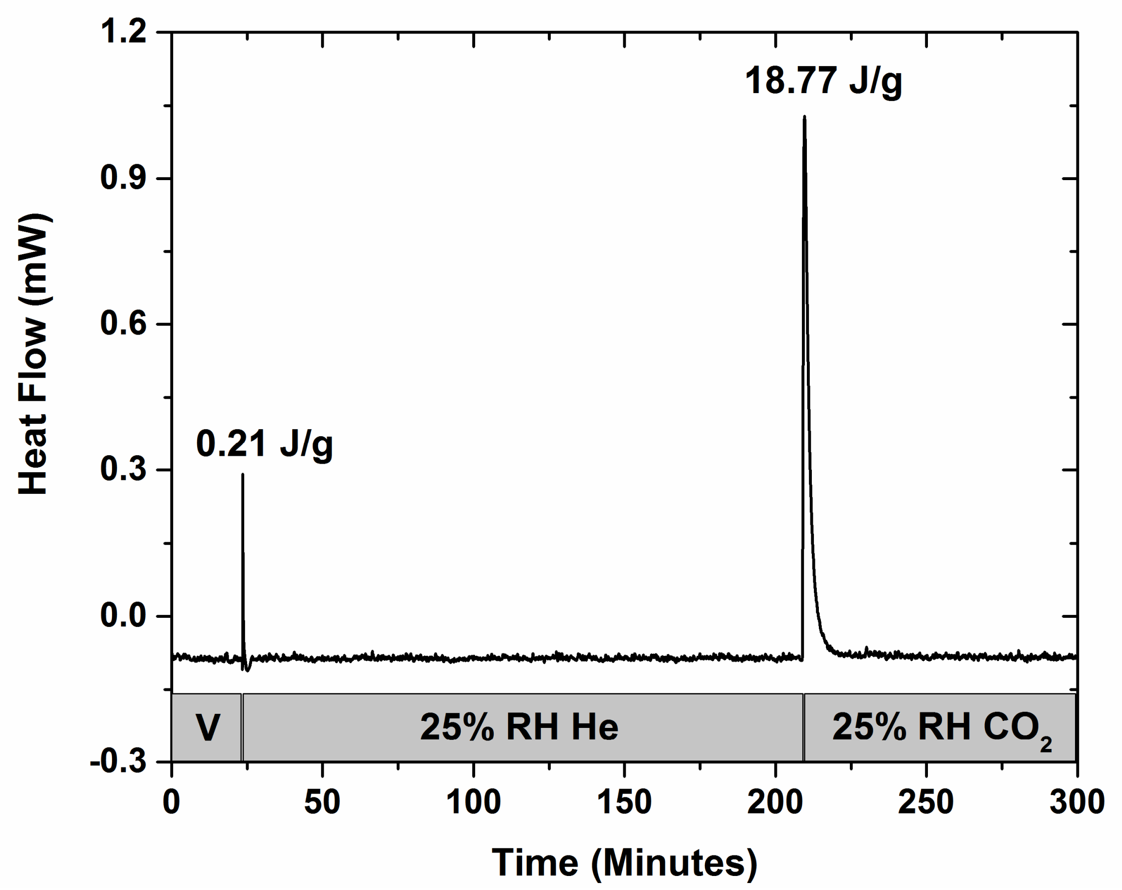

Figure 27. DSC signal during CaSDB humid atmosphere (25% RH) swing. Activated CaSDB under vacuum is first exposed to helium gas at 25% RH at a constant flow of 150 mL/min, then to an atmosphere of CO_2 at 25% RH.

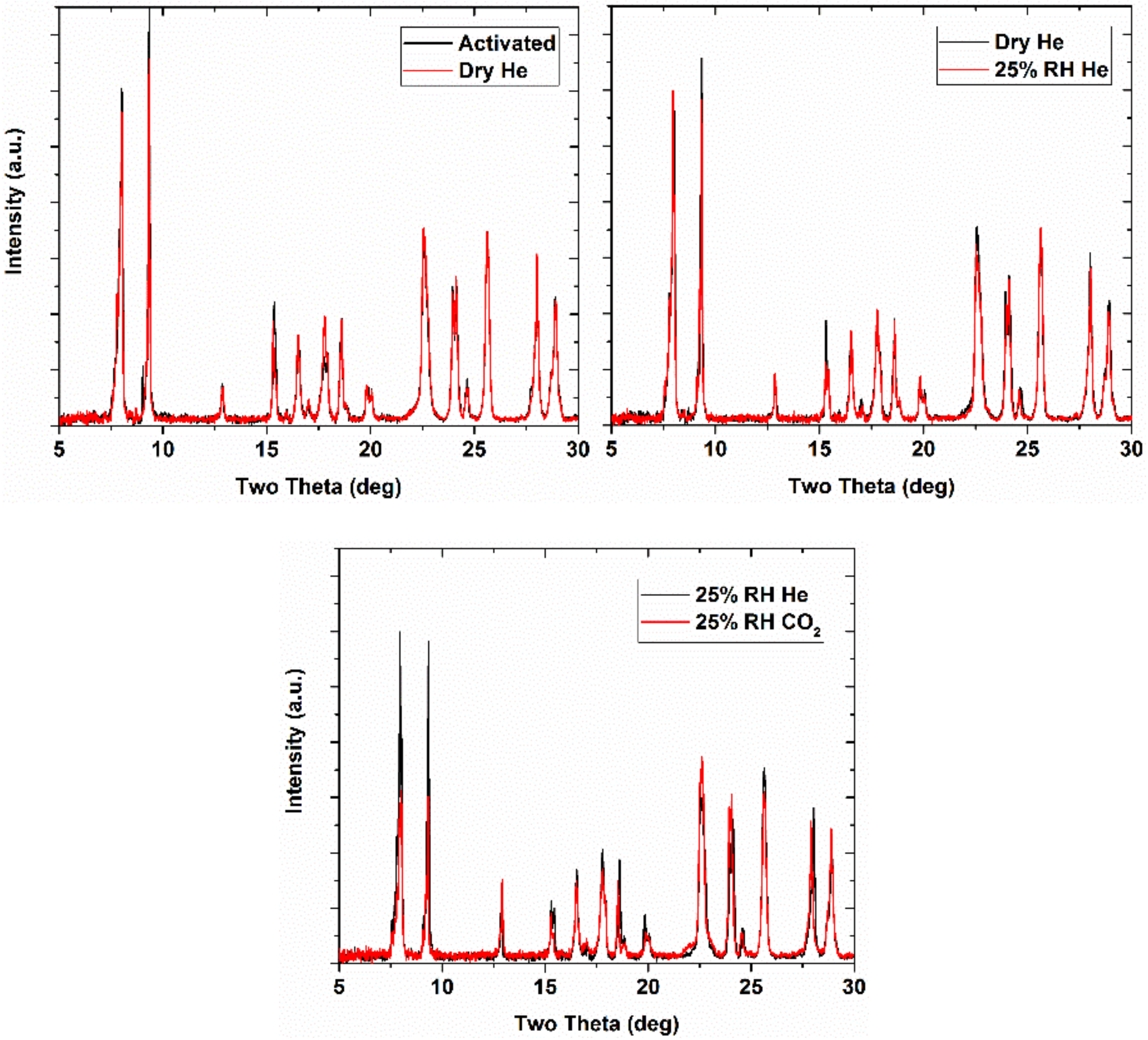

Figure 28. XRD patterns of CaSDB under different gas loading conditions. (left) Activated CaSDB under vacuum vs dry helium. (middle) CaSDB under dry helium vs after exposure to 25% RH helium. (right) CaSDB under 25% RH helium vs 25% RH CO_2.

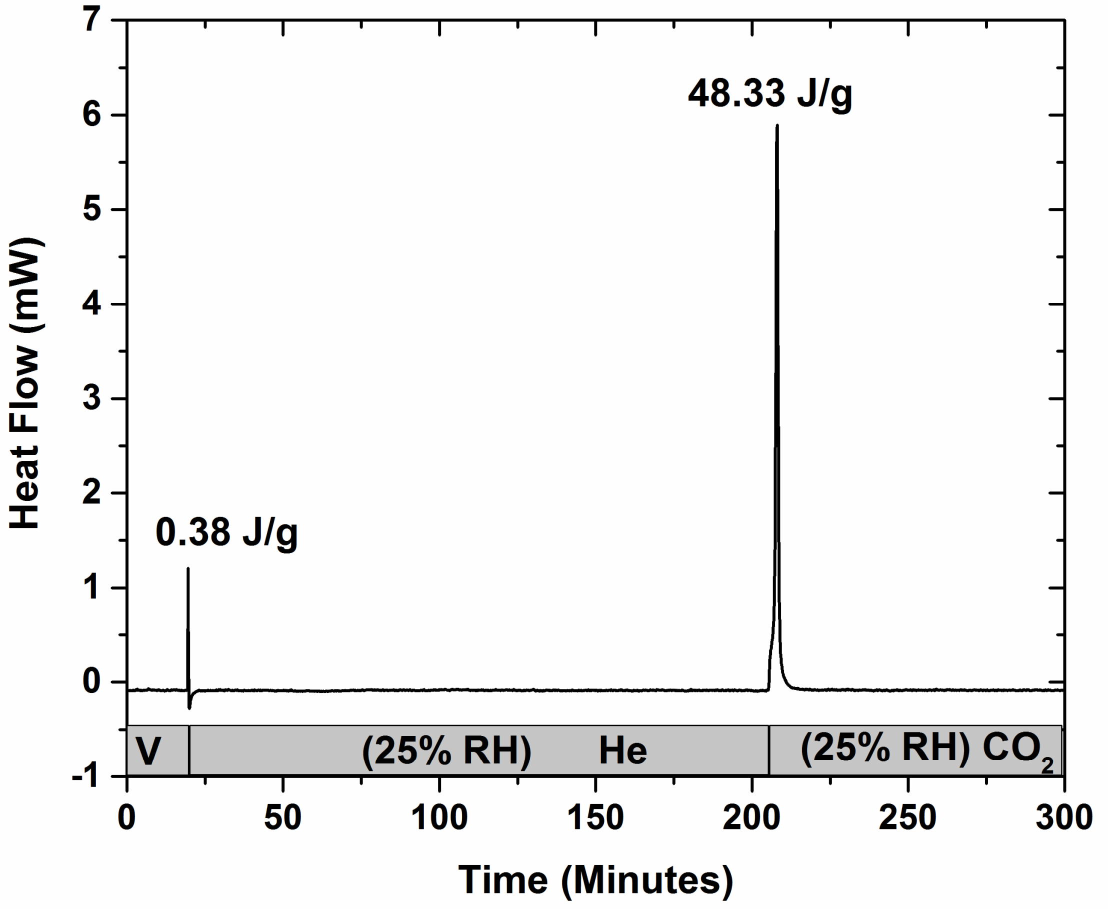

Figure 29. DSC signal during ZIF-7 humid atmosphere (25% RH) swing. Activated ZIF-7 under vacuum (V) is first exposed to helium gas at 25% RH at a constant flow of 150 mL/min, then to an atmosphere of CO_2 at 25% RH.

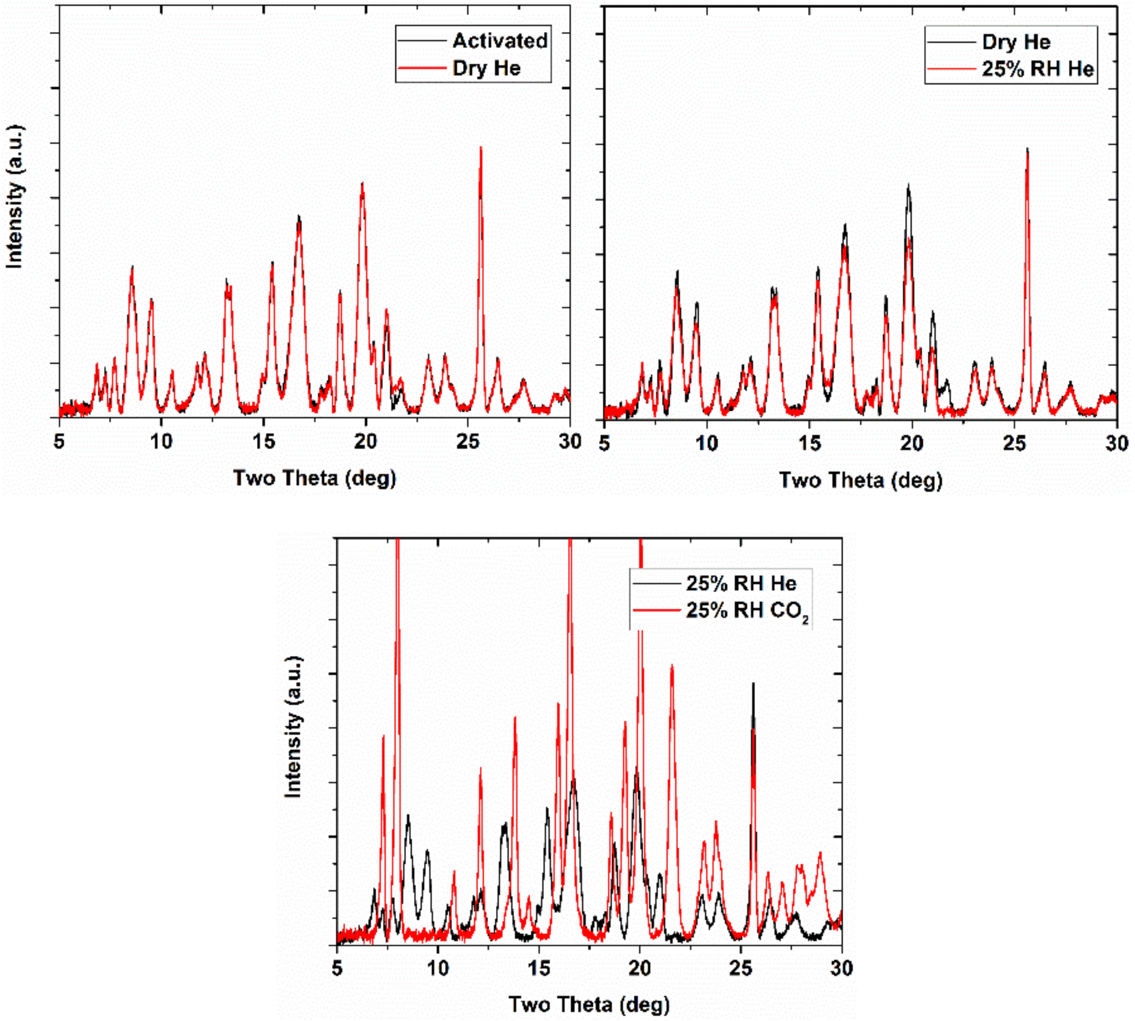

Figure 30. XRD patterns of ZIF-7 under different gas loading conditions. (top left) Activated ZIF-7 under vacuum vs dry helium. (top right) ZIF-7 under dry helium vs after exposure to 25% RH helium. (bottom) ZIF-7 under 25% RH helium vs 25% RH CO_2.

Design Limitations of the XRD-DSC

The current design/implementation of the XRD-DSC and HASC limits the experimental temperature for studies to room temperature (~22°C) as the HASC cannot currently be heated to the higher temperatures typical of flue gas (40-60°C).[13] This experimental setup requires all of the equipment shown in Figure 1 to be setup inside the Rigaku Ultima IV hutch so it can be sealed to collect the XRD patterns. Future adaptations could include moving the gas delivery equipment and vacuum manifold outside of the hutch and plumb gas lines through the hutch to the XRD-DSC head. The HASC operation can be further modified to operate at flue-gas temperature by fitting it in a recirculating oven outside the hutch and installing heated/insulated gas tubing to the XRD-DSC. These modifications would enable the study of CO_2 adsorption in microporous materials at both realistic temperatures and humidity.

Conclusions

The utility of the XRD-DSC vacuum and atmosphere swing techniques were successfully demonstrated through investigating of the effects of humidity on the CO_2 adsorption performance of selected microporous compounds. In principle, vacuum – atmosphere swings with the XRD-DSC can be used as a screening tool for gas adsorption in unknown materials and speed up the discovery-development cycle. Calorimetric measurements of the total enthalpy of gas adsorption can directly determine the CO_2 enthalpy of adsorption even in cases where the isosteric heat of adsorption cannot be calculated from isotherm fitting. This was highlighted by determining the CO_2 enthalpy of adsorption on the guest-induced gate-opening transition of ZIF-7 to be ~ 11 kJ/mol before, and ~ 27 kJ/mol after the transition. The total measured enthalpy during the adsorption process was used to evaluate the performance of CO_2 adsorption in the presence of water vapor in

CaSDB, ZIF-7, Ni-MOF-74, and zeolite NaX.

Humid atmosphere swings at 25% RH between helium and CO_2 evaluated the adsorption performance after prolonged exposure to water vapor. The organic linker coordination compounds of CaSDB and ZIF-7 have high resistance to water vapor and retain the majority of adsorption capacity, 64.16% and 79.02% respectively. The compounds with unsaturated metal site adsorption, NaX and Ni-MOF-74, have slow and energetic exotherms from water adsorption which reduced the subsequent CO_2 capacity to 5.46% and 3.38% respectively, after exposure. The changes observed in the XRD patterns supported the hypothesis that the capacity loss was due to water adsorption.

Vacuum – humid atmosphere swings evaluated the co-adsorption of water vapor and CO_2 to simulate vacuum swing capture under flue-gas water content. In similar fashion to the humid atmosphere swings, the presence of water vapor in 25% RH CO_2 reduced the performance of NaX and Ni-MOF-74 by ~70% while CaSDB and ZIF-7 only showed a minor reduction in performance to ~95% and ~97%, respectively. Even at a more extreme 75% RH, CO_2 adsorption in CaSDB and ZIF-7 was only mildly hindered. XRD patterns revealed the co-adsorption process is not a straightforward adsorption site poisoning in Ni-MOF-74 and CaSDB, and each compound warrants further investigation. Additionally, the adsorption of CO_2 under high humidity (75% RH) was found to shift the guest induced gate-opening transition in ZIF-7 by 0.1 atm while reducing the performance by ~15%. The humidity XRD-DSC experiments indicate the organic linker adsorption mechanism of CaSDB and ZIF-7 may be more ideally suited for post-combustion flue-gas CO_2 capture than compounds with unsaturated metal sites.

References

1. Pachauri, R. K. R., A., IPCC Fourth Assesment Report. In *Intergovernmental Panel on Climate Change*, 2007.

2. Sumida, K.; Rogow, D. L.; Mason, J. A.; McDonald, T. M.; Bloch, E. D.; Herm, Z. R.; Bae, T. H.; Long, J. R., Carbon Dioxide Capture in Metal-Organic Frameworks. *Chemical Reviews* **2012,** 112, (2), 724-781.

3. Demirbas, A., Carbon dioxide emissions and carbonation sensors. *Energy Sources Part a-Recovery Utilization and Environmental Effects* **2008,** 30, (1), 70-78.

4. Rochelle, G. T., Amine Scrubbing for CO2 Capture. *Science* **2009,** 325, (5948), 1652-1654.

5. Sharma, S. D.; Azzi, M., A critical review of existing strategies for emission control in the monoethanolamine-based carbon capture process and some recommendations for improved strategies. *Fuel* **2014,** 121, 178-188.

6. Figueroa, J. D.; Fout, T.; Plasynski, S.; McIlvried, H.; Srivastava, R. D., Advances in CO2 capture technology—The U.S. Department of Energy's Carbon Sequestration Program. *International Journal of Greenhouse Gas Control* **2008,** 2, (1), 9-20.

7. Bae, T. H.; Hudson, M. R.; Mason, J. A.; Queen, W. L.; Dutton, J. J.; Sumida, K.; Micklash, K. J.; Kaye, S. S.; Brown, C. M.; Long, J. R., Evaluation of cation-exchanged zeolite adsorbents for post-combustion carbon dioxide capture. *Energy & Environmental Science* **2013,** 6, (1), 128-138.

8. Furukawa, H.; Cordova, K. E.; O'Keeffe, M.; Yaghi, O. M., The Chemistry and Applications of Metal-Organic Frameworks. *Science* **2013,** 341, (6149), 974-+.

9. Fracaroli, A. M.; Furukawa, H.; Suzuki, M.; Dodd, M.; Okajima, S.; Gandara, F.; Reimer, J. A.; Yaghi, O. M., Metal-Organic Frameworks with Precisely Designed Interior for Carbon Dioxide Capture in the Presence of Water. *Journal of the American Chemical Society* **2014,** 136, (25), 8863-8866.

10. Nugent, P.; Belmabkhout, Y.; Burd, S. D.; Cairns, A. J.; Luebke, R.; Forrest, K.; Pham, T.; Ma, S. Q.; Space, B.; Wojtas, L.; Eddaoudi, M.; Zaworotko, M. J., Porous materials with optimal adsorption thermodynamics and kinetics for CO2 separation. *Nature* **2013,** 495, (7439), 80-84.

11. Kizzie, A. C.; Wong-Foy, A. G.; Matzger, A. J., Effect of Humidity on the Performance of Microporous Coordination Polymers as Adsorbents for CO2 Capture. *Langmuir* **2011,** 27, (10), 6368-6373.

12. Li, G.; Xiao, P.; Webley, P.; Zhang, J.; Singh, R.; Marshall, M., Capture of CO2 from high humidity flue gas by vacuum swing adsorption with zeolite 13X. *Adsorption-Journal of the International Adsorption Society* **2008,** 14, (2-3), 415-422.

13. Granite, E. J.; Pennline, H. W., Photochemical removal of mercury from flue gas. *Industrial*

& Engineering Chemistry Research **2002,** 41, (22), 5470-5476.

14. Hudson, M. R.; Queen, W. L.; Mason, J. A.; Fickel, D. W.; Lobo, R. F.; Brown, C. M., Unconventional, Highly Selective CO2 Adsorption in Zeolite SSZ-13. *Journal of the American Chemical Society* **2012,** 134, (4), 1970-1973.

15. Plonka, A. M.; Banerjee, D.; Woerner, W. R.; Zhang, Z. J.; Li, J.; Parise, J. B., Effect of ligand geometry on selective gas-adsorption: the case of a microporous cadmium metal organic framework with a V-shaped linker. *Chemical Communications* **2013,** 49, (63), 7055-7057.

16. Plonka, A. M.; Banerjee, D.; Woerner, W. R.; Zhang, Z. J.; Nijem, N.; Chabal, Y. J.; Li, J.; Parise, J. B., Mechanism of Carbon Dioxide Adsorption in a Highly Selective Coordination Network Supported by Direct Structural Evidence. *Angewandte Chemie-International Edition* **2013,** 52, (6), 1692-1695.

17. Zhao, P.; Lampronti, G. I.; Lloyd, G. O.; Suard, E.; Redfern, S. A. T., Direct visualisation of carbon dioxide adsorption in gate-opening zeolitic imidazolate framework ZIF-7. *Journal of Materials Chemistry A* **2014,** 2, (3), 620-623.

18. Dietzel, P. D. C.; Johnsen, R. E.; Fjellvag, H.; Bordiga, S.; Groppo, E.; Chavan, S.; Blom, R., Adsorption properties and structure of CO(2) adsorbed on open coordination sites of metal-organic framework Ni(2)(dhtp) from gas adsorption, IR spectroscopy and X-ray diffraction. *Chemical Communications* **2008**, (41), 5125-5127.

19. Xie, J. K.; Yan, N. Q.; Liu, F.; Qu, Z.; Yang, S. J.; Liu, P., CO2 adsorption performance of ZIF-7 and its endurance in flue gas components. *Frontiers of Environmental Science & Engineering* **2014,** 8, (2), 162-168.

20. Yu, J. M.; Balbuena, P. B., Water Effects on Postcombustion CO2 Capture in Mg-MOF-74. *Journal of Physical Chemistry C* **2013,** 117, (7), 3383-3388.

21. Liu, J.; Tian, J.; Thallapally, P. K.; McGrail, B. P., Selective CO2 Capture from Flue Gas Using Metal-Organic Frameworks-A Fixed Bed Study. *Journal of Physical Chemistry C* **2012,** 116, (17), 9575-9581.

22. Wu, D.; Gassensmith, J. J.; Gouvea, D.; Ushakov, S.; Stoddart, J. F.; Navrotsky, A., Direct Calorimetric Measurement of Enthalpy of Adsorption of Carbon Dioxide on CD-MOF-2, a Green Metal-Organic Framework. *Journal of the American Chemical Society* **2013,** 135, (18), 6790-6793.

23. Wu, D.; Navrotsky, A., Thermodynamics of metal-organic frameworks. *Journal of Solid State Chemistry* **2015,** 223, (0), 53-58.

24. Hulvey, Z.; Lawler, K. V.; Qao, Z. W.; Zhou, J.; Fairen-Jimenez, D.; Snurr, R. Q.; Ushakov, S. V.; Navrotsky, A.; Brown, C. M.; Forster, P. M., Noble Gas Adsorption in Copper Trimesate, HKUST-1: An Experimental and Computational Study. *Journal of Physical Chemistry C* **2013,** 117, (39), 20116-20126.

25. Banerjee, D.; Zhang, Z. J.; Plonka, A. M.; Li, J.; Parise, J. B., A Calcium Coordination

Framework Having Permanent Porosity and High CO2/N-2 Selectivity. *Crystal Growth & Design* **2012,** 12, (5), 2162-2165.

26. Yazaydın, A. Ö.; Snurr, R. Q.; Park, T.-H.; Koh, K.; Liu, J.; LeVan, M. D.; Benin, A. I.; Jakubczak, P.; Lanuza, M.; Galloway, D. B.; Low, J. J.; Willis, R. R., Screening of Metal−Organic Frameworks for Carbon Dioxide Capture from Flue Gas Using a Combined Experimental and Modeling Approach. *Journal of the American Chemical Society* **2009,** 131, (51), 18198-18199.

27. Caskey, S. R.; Wong-Foy, A. G.; Matzger, A. J., Dramatic tuning of carbon dioxide uptake via metal substitution in a coordination polymer with cylindrical pores. *Journal of the American Chemical Society* **2008,** 130, (33), 10870-+.

28. Aguado, S.; Bergeret, G.; Titus, M. P.; Moizan, V.; Nieto-Draghi, C.; Bats, N.; Farrusseng, D., Guest-induced gate-opening of a zeolite imidazolate framework. *New Journal of Chemistry* **2011,** 35, (3), 546-550.

29. Dietzel, P. D. C.; Besikiotis, V.; Blom, R., Application of metal-organic frameworks with coordinatively unsaturated metal sites in storage and separation of methane and carbon dioxide. *Journal of Materials Chemistry* **2009,** 19, (39), 7362-7370.

30. Liu, J.; Wang, Y.; Benin, A. I.; Jakubczak, P.; Willis, R. R.; LeVan, M. D., CO2/H2O Adsorption Equilibrium and Rates on Metal-Organic Frameworks: HKUST-1 and Ni/DOBDC. *Langmuir* **2010,** 26, (17), 14301-14307.

31. Sircar, S., Isosteric Heats of Multicomponent Gas-Adsorption on Heterogeneous Adsorbents. *Langmuir* **1991,** 7, (12), 3065-3069.

32. Pulin, A. L.; Fomkin, A. A., Thermodynamics of CO2 adsorption on zeolite NaX in wide intervals of pressures and temperatures. *Russian Chemical Bulletin* **2004,** 53, (8), 1630-1634.

33. Cho, S.-H.; Ma, B.; Nguyen, S. T.; Hupp, J. T.; Albrecht-Schmitt, T. E., A metal-organic framework material that functions as an enantioselective catalyst for olefin epoxidation. *Chemical Communications* **2006**, (24), 2563-2565.

34. Maihom, T.; Wannakao, S.; Boekfa, B.; Limtrakul, J., Production of Formic Acid via Hydrogenation of CO2 over a Copper-Alkoxide-Functionalized MOF: A Mechanistic Study. *Journal of Physical Chemistry C* **2013,** 117, (34), 17650-17658.

35. Horike, S.; Dinca, M.; Tamaki, K.; Long, J. R., Size-selective lewis acid catalysis in a microporous metal-organic framework with exposed Mn(2+) coordination sites. *Journal of the American Chemical Society* **2008,** 130, (18), 5854-+.

36. Alkordi, M. H.; Liu, Y.; Larsen, R. W.; Eubank, J. F.; Eddaoudi, M., Zeolite-like Metal−Organic Frameworks as Platforms for Applications: On Metalloporphyrin-Based Catalysts. *Journal of the American Chemical Society* **2008,** 130, (38), 12639-12641.

Chapter 4

Structural chemistry of akdalaite, $Al_{10}O_{14}(OH)_2$, the aluminum analogue of ferrihydrite, in its single and polycrystalline forms

Abstract

The complete structure of the mineral akdalaite – $Al_{10}O_{14}(OH)_2$ was solved using a combination of single crystal X-ray diffraction, neutron powder diffraction, and solid-state nuclear magnetic resonance. Akdalaite crystallizes in the space group $P6_3mc$ with lattice parameters of a = 5.576376(9) Å and c = 8.77275(4) Å. The position of the hydrogen site was determined and refined for the first time revealing a single split occupancy site about the three-fold axis, similar to the geometry observed in the hydroxide minerals portlandite and brucite. Crystallographic analysis revealed the crystal chemistry of akdalaite is non ideal and broadly conforms to that of ferrihydrite, the nanomineral for which it is the presumed structural analog. In particular, anomalies in bond valence and octahedral distortion occur in both structure models for akdalaite and ferrihydrite that border on violating crystal chemical principles. X-ray total scattering and pair distribution function analysis comparing akdalaite with 6 line ferrihydrite provide new evidence that the two compounds are indeed structurally related.

Introduction

Nanocrystalline minerals, or nanominerals, are prevalent throughout the natural environment where they commonly act as substrates for the sorption, transport, desorption of contaminants.[1, 2] While the properties of many nanominerals are well known, the atomic arrangements, which are responsible for those properties, are not. The fundamental equations that relate atomic arrangements to observed X-ray, neutron, and electron diffraction apply equally to all matter whether crystalline, nanocrystalline, or aperiodic.[3] However, simplifications of those equations for crystalline materials allow for the determination of atomic arrangements, *ab inito,* by considering only the Bragg scattering and ignoring diffuse scattering that can arise from defects or disorder. On the other hand, determination of the atomic arrangements in nanomaterials, with few exceptions,[4] cannot be carried out *ab initio*. Instead, the total scattering (Bragg + diffuse) must be fitted and so deriving a viable structure model often relies on intuition, model building, and database searches for potential crystalline analogs. Once a viable structure model is obtained, it can be refined against measured total scattering data, or its Fourier transform, the pair distribution function (PDF),[5] in a manner analogous to the well-known crystallographic techniques (Rietveld refinement) used for Bragg scattering and crystalline materials.[6, 7] The structure determination of the ubiquitous ferric oxyhydroxide nanomineral ferrihydrite (particle size < 6 nm) is a case in point.

The structure of ferrihydrite was the focus of scientific debate for at least half a century, and much of the literature for the for that period is summarized in a review by Jambor and Dutrizac.[8] Following publication of a multiphase model,[9] a single-phase model for the atomic arrangements in ferrihydrite emerged based on the structure of the aluminum oxyhydroxide mineral akdalaite as it provided the best match to the X-ray PDF patterns for all ferrihydrite particle sizes. The akdalaite model for ferrihydrite first presented by Michel et al. (2007)[10] and later refined by Michel et al. (2010)[11] was immediately controversial. The objections ranged from the valid - focusing on crystal chemical anomalies, to the vapid and naïve – complaints that XRD patterns don't match to crystalline model simulations and that refinements are under constrained with the release of all least squares parameters leading to an unstable refinement.[12-15] There are aspects of the akdalaite-based model that are inconsistent with expectations based on accepted crystal chemical arguments, but are these deviations for the expected crystal chemistry intrinsic to the model shared by both akdalaite and ferrihydrite? Is it possible akdalaite is an inappropriate analogue for ferrihydrite? Or is the real space PDF refinement process not adequately addressing contributions from particle size, morphology or surface contributions?

The single-phase akdalaite model for ferrihydrite is supported by, and has been reconciled with, available data, but the most recent model (Michel et al., 2010) remains controversial due to specific inconsistencies in the crystal chemistry.[11, 16, 17] The single-phase Michel model for ferrihydrite has some bond valence sums that are inconsistent with the expected values of +3 and -2 for Fe^{3+} and O^{2-}, respectively (Figure 1). Additionally, in the single-phase model the Fe1 – Fe1 distance and the Fe1 and Fe2 octahedral distortions are anomalous compared to values expected based on the crystal chemistry of the iron oxides and hydroxides (Figures 1 and 2).[13, 14] To evaluate the validity of the crystal chemical arguments, the akdalaite model must be completely solved and studied in detail.

As the akdalaite structure is related to that of δ-Al_{13} Keggin cluster, it would also be desirable to compare the single-phase ferrihydrite model to that of a δ-Fe_{13} Keggin cluster as well.[18] Comparisons to the δ-Al_{13} Keggin revealed similar over and under bonding, as seen in the single-phase ferrihydrite model, however the δ-Fe_{13} Keggin has never been isolated for crystallographic study.[12] Recent work has isolated the α-Fe_{13} Keggin but it cannot be used for a crystal chemical comparison to the ferrihydrite model as it has a different structure.[19] While a crystal chemical analysis of the δ-Fe_{13} Keggin could provide additional insight into the anomalies of the ferrihydrite structure, the Keggin clusters are not ideal for comparison as they are stabilized by counter-ions and are not continuous 3D structures, but rather isolated clusters.

If ferrihydrite were available in single crystal, polycrystalline, and nanocrystalline form, many of the questions raised about the relationships between models fitted to X-ray PDF data could be addressed directly. The crystal chemistry of "single crystal" ferrihydrite could then be explored for bonding anomalies, and the adequacy of the model evaluated for poly- and nanocrystalline forms. Although ferrihydrite does not exist in all size ranges, the aluminum oxyhydroxide akdalaite, which is the presumed structural analog of ferrihydrite, does. Herein, for the first time, the structure of akdalaite is fully characterized and compared to ferrihydrite through the utilization of single crystal X-ray diffraction, neutron powder diffraction, solid-state nuclear magnetic resonance, and X-ray total scattering. Structural analysis reveals the crystal chemical abnormalities of the single-phase ferrihydrite model intrinsic to the akdalaite structure. PDF analysis provides further evidence that the akdalaite model is a good description for the structure of ferrihydrite; though particle morphology, defects, and surface reconstruction affect the total scattering.[20, 21]

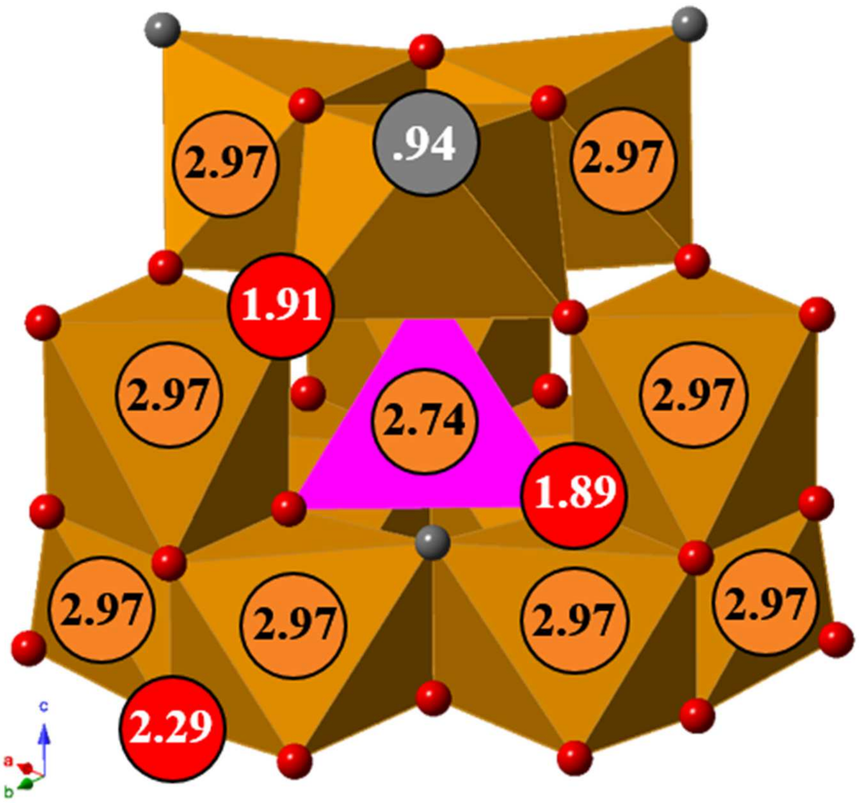

Figure 1. Revised structure of ferrihydrite from Michel et al. (2010) shown in the Keggin motif with the calculated bond valences of each site. The Fe octahedra are brown, the tetrahedral Fe is purple, oxygen atoms are red, and hydroxyl is gray.

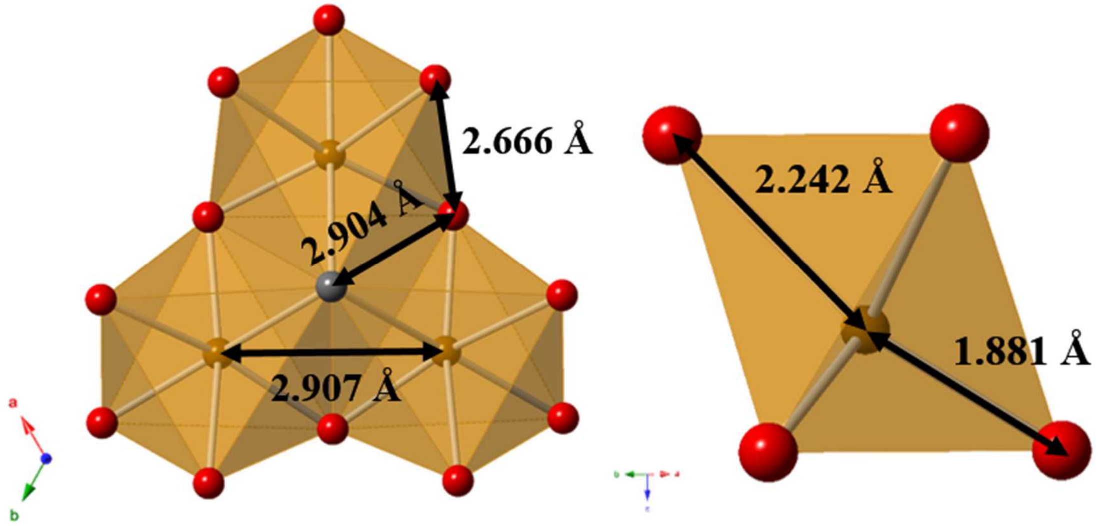

Figure 2. (left) The connectivity of the octahedral Fe1 site with the Fe1 – Fe1 distance as 2.907 Å, shared edge O1 – O3 distance of 2.904 Å, and unshared edge O3 – O2 distance of 2.666 Å. (right) Distorted Fe2 octahedra having Fe-O distances of 1.881 Å, which are shorter than the tetrahedral distances of 1.932 Å.

Akdalaite

The composition for the mineral akdalaite, $Al_{10}O_{14}(OH)_2$ is often misrepresented in the literature as $5Al_2O_3 \bullet H_2O$.[22] Akdalaite is found in 4 localities and exists naturally in both crystalline and nanocrystalline (~6 nm diameter plates) forms.[23-26] Akdalaite is structurally analogous to the minerals nolanite [$(Fe, V, Ti)_{10}O_{14}(OH)_2$] and rinmanite [$Zn_2Sb_2Mg_2Fe_4O_{14}(OH)_2$].[27-29] Before akdalaite was discovered in 1971, a synthetic analog was synthesized in 1964 using hydrothermal methods and given the name "tohdite."[22] However, akdalaite and "tohdite" were not determined to be equivalent until a reinvestigation of akdalaite using electron microscopy revealed the original akdalaite crystallographic investigation failed to take additional minor phases into account.[23]

The structure solution of crystalline "tohdite" (Figure 3) was conducted in 1965 and refined in 1969 using a laboratory-based powder X-ray diffraction (PXRD) pattern.[30, 31] The hexagonal unit cell has 10 aluminum sites with 8 in octahedral coordination and 2 in tetrahedral coordination in 3 crystallographically distinct Al sites (octahedral site 1 – 60%, octahedral site 2 – 20%, and tetrahedral site 1 – 20%). The PXRD derived "tohdite" model for akdalaite is somewhat unreliable since the exact overlap of reflections cannot be fully discerned in powder diffraction patterns, which makes Laue and point group assignments ambiguous. Powder diffraction data cannot distinguish between trigonal and hexagonal Laue groups, as both systems will appear as having 6/mmm crystal symmetry. Single crystal data, on the other hand, can separate out the reflections related by Laue symmetry and distinguish between the four trigonal and hexagonal Laue classes. It is imperative to accurately define atomic coordinates and the bonding environments, including the O-H coordination, in order to calculate the bond valence values for aluminum and oxygen. Moreover, the structural features involving hydrogen atoms can be more precisely determined using elastic neutron scattering.

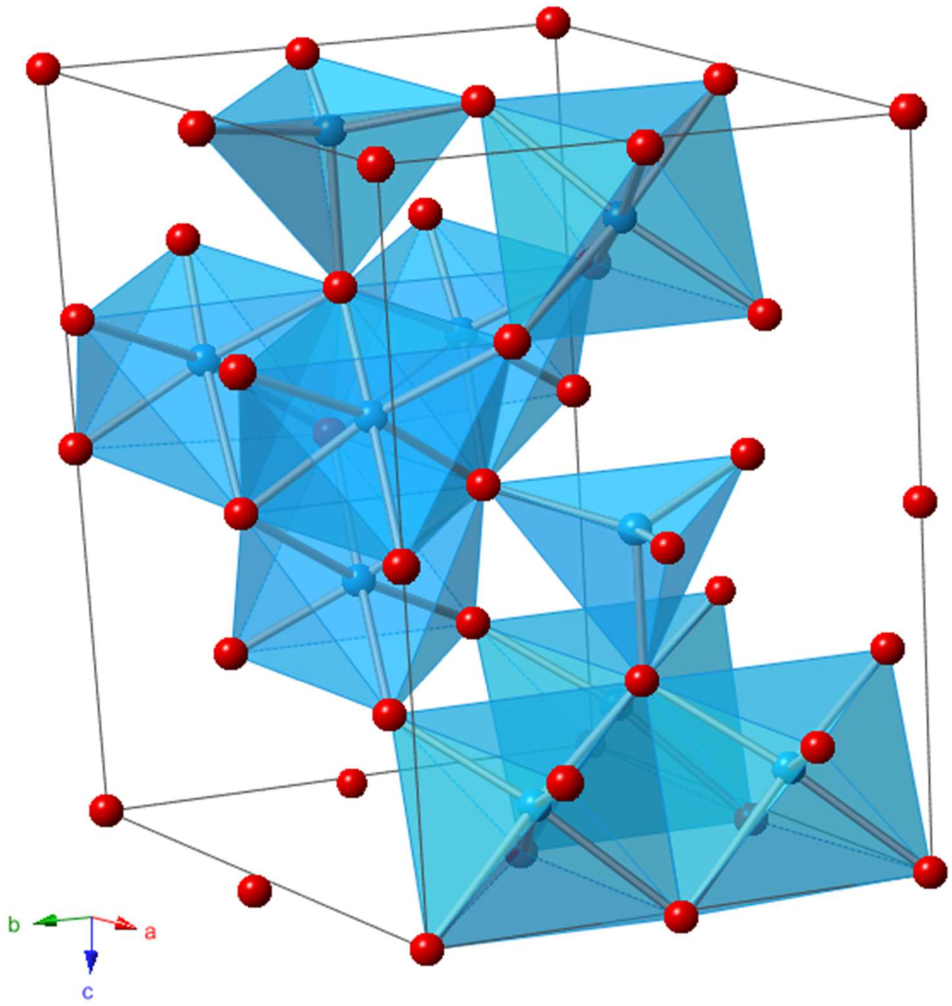

Figure 3. Unit cell of “tohdite.” Al atoms are centered in the blue polyhedra while oxygen atoms are red. Space group – P6$_3$mc; *a* = 5.575 Å, *c* = 8.761 Å.

Experimental

Sample Preparation and Provenance

Samples of crystalline akdalaite were synthesized hydrothermally in cold-seal pressure vessels[32] using a modified method of Rosenberg (2006).[33] The starting materials were sealed in a gold capsule (2 cm long, 5 mm diameter) with an aqueous solution of 0.54 M NH_4F in a 2:1 weight ratio. The capsule was subjected to 2 kbar and 475°C in the cold-seal vessel for 5 days. Two different starting materials were used to produce different crystal morphologies. When the starting material was a synthetic aluminum oxyhydroxide floc (Al-floc),[34] the akdalaite product consisted of uniform needles that were typically 50 µm long and 1 µm wide. The synthetic Al-floc material was formed by the instantaneous mixing of 0.2 M $AlCl_3$ and 0.48 M NaOH in equal volumes. The Al-floc gel was then centrifuged dried at 50°C for 12 hours. This was chosen as a starting material as it is amorphous and thought to be composed mostly of aggregates of Al_{13} Keggin polyoxocations with Al in 4, 5, and 6 coordination which would act as nucleation sites and allow for the rapid transformation to akdalaite.[34]

Larger akdalaite crystals of a size suitable for SC-XRD were synthesized using nanocrystalline boehmite (Vista Chemical Company Catapal D alumina) as the starting material. The akdalaite crystals produced from boehmite had a hexagonal plate morphology with diameter of ~20 µm, which were large enough for synchrotron single crystal diffraction studies. After hydrothermal synthesis, sample powders with washed repeatedly with DI water to remove any possible remnants of recrystallized NH_4F and dried at 50°C for 12 hours. In order to produce enough sample for powder neutron diffraction, a single experiment was conducted using nanocrystalline boehmite and a 5.5 cm long gold capsule.

Natural Sample

A small rock chip (1.0 x 0.5 x 0.5 mm) from the type locality of the Solnechnoye fluorite deposit in Kazakhstan[24] was obtained from a 2006 reexamination by Hwang et al.[23] Previous analysis established the rock chip contained akdalaite, fluorite, σ-Al_2O_3, and margarite. This sample was used to confirm that natural akdalaite is indeed "tohdite" as both have the same diffraction pattern after accounting for impurities.[23] The rock chip was kept whole as a suitable single crystal of akdalaite could not be found and is a rare type specimen.

Analytical Methods

Laboratory Powder X-ray Diffraction (PXRD)

Bulk sample identification and phase purity were initially checked using laboratory PXRD. The data were collected using a Rigaku Ultima IV (Cu Kα radiation) with a D/TeX linear position sensitive detector. Patterns were collected over a range of $5° \leq 2\theta \leq 90°$ with a step size of 0.01° at a rate of 1°/min.

Scanning Electron Microscopy (SEM)

SEM images of akdalaite synthesized using synthetic Al-floc starting material were obtained using a LEO 1550 scanning electron microscope at an operating voltage of 20 kV. The images of akdalaite synthesized from boehmite were obtained with a Hitachi S-2600N at an operating voltage of 10 kV. Samples were mounted on aluminum sample holders with carbon tape and gold coated using an EMS-550X sputter coater.

Single Crystal X-ray Diffraction (SC-XRD)

Reflections for a single crystal of synthetic akdalaite (hexagonal plate morphology) were collected at 100 K using a three-circle Bruker D8 diffractometer equipped with an APEXII detector (λ = 0.41328 Å) using 0.5° φ scans at the ChemMatCars beamline (sector 15) of the Advanced Photon Source (APS). Raw intensity data were collected, integrated and corrected for absorption effects with the Apex II software suite (v1.22, Bruker AXS).

Neutron Powder Diffraction (NPD)

Time of flight (TOF) neutron powder diffraction data were collected using the POWGEN instrument (BL-11) at the Spallation Neutron Source of Oak Ridge National Laboratory. Approximately 1g of powdered sample in was loaded into a 6 mm vanadium can for measurements at room temperature (299 K). POWGEN data were collected using frames 2 (0.35 Å $\leq$ d $\leq$ 3.0 Å) and 5 (1.15 Å $\leq$ d $\leq$ 6.0 Å). Frame 2 data were collected for 3 hours and frame 5 for 1 hour.

High-Energy Powder X-ray Total Scattering

High-energy X-ray total scattering data were collected at the 11-ID-B beamline at the APS using ~20 mg of synthetic akdalaite in a kapton capillary. The 2D diffraction data were collected at 58.26 keV (λ=0.2128 Å) using a Perking-Elmer XRD 1621 detector. The geometry of the experimental setup was calibrated with a CeO_2 standard (NIST 674a) and the data were integrated into a 1D pattern using the program Fit2D.[35] The total scattering function [*S(Q)*] and pair distribution function [PDF, *G(r)*] were obtained using a Q_{max} of 25 Å^{-1} with the program PDFgetX2 with standard and area detector geometry corrections.[36, 37]

Nuclear Magnetic Resonance (NMR)

All solid state NMR spectra were acquired with a 500 MHz (11.7 T) Varian Infinity-Plus spectrometer equipped with Varian/Chemagnetics sample probe assemblies configured for 3.2 and 4.0 mm (o.d.) rotors and operating at 130.3 and 499.78 MHz for ^{27}Al and ^{1}H, respectively. The ^{27}Al magic angle spinning (MAS) NMR spectra were acquired at a spinning rate of 20 kHz with 0.5 μs pulses (ν_{RF} = 50 kHz) and 0.5 s relaxation delay. Over 96% of the magnetization is recovered under these conditions. No differential relaxation effects were noted in spectra taken with relaxation delays that varied from 60 to 0.5 s. The ^{27}Al multiple-quantum MAS data (MQ/MAS) were taken at a 20 kHz spinning rate using 1.9 μs excitation and 0.8 μs conversion pulses (ν_{RF} = 132 kHz), followed by an 18 μs selective 90° zero-quantum filter pulse, with phase cycling to select the triple quantum coherence. We collected 80 hypercomplex points with a $t1$ increment of 25 μs, each the sum of 384 acquisitions taken with a 0.5 s relaxation delay. The ^{1}H MAS/NMR spectrum was obtained at a spinning rate of 15 kHz using 1 μs pulses (90° = 4 μs) and a 4 s relaxation delay. Chemical shifts are reported relative to a 0.1 *m* aqueous $AlCl_3$ solution for ^{27}Al and tetramethylsilane (TMS) for ^{1}H.

Results and Discussion

Initial Characterization

The synthesized akdalaite samples were first inspected with laboratory PXRD and the crystal morphology was investigated with SEM. Akdalaite synthesized using the Al-floc starting material was nearly pure akdalaite with a needle morphology and minor corundum impurity (Figure 4). The akdalaite synthesized from nanocrystalline boehmite also had a minor corundum impurity but had a hexagonal plate morphology suitable for SC-XRD (Figure 5). The 1g sample synthesized from boehmite for NPD utilized a much longer capsule (5.5 cm) and was likely subject to a higher thermal gradient in the cold seal vessel which resulted in a higher amount of impurity corundum (Figure 6).

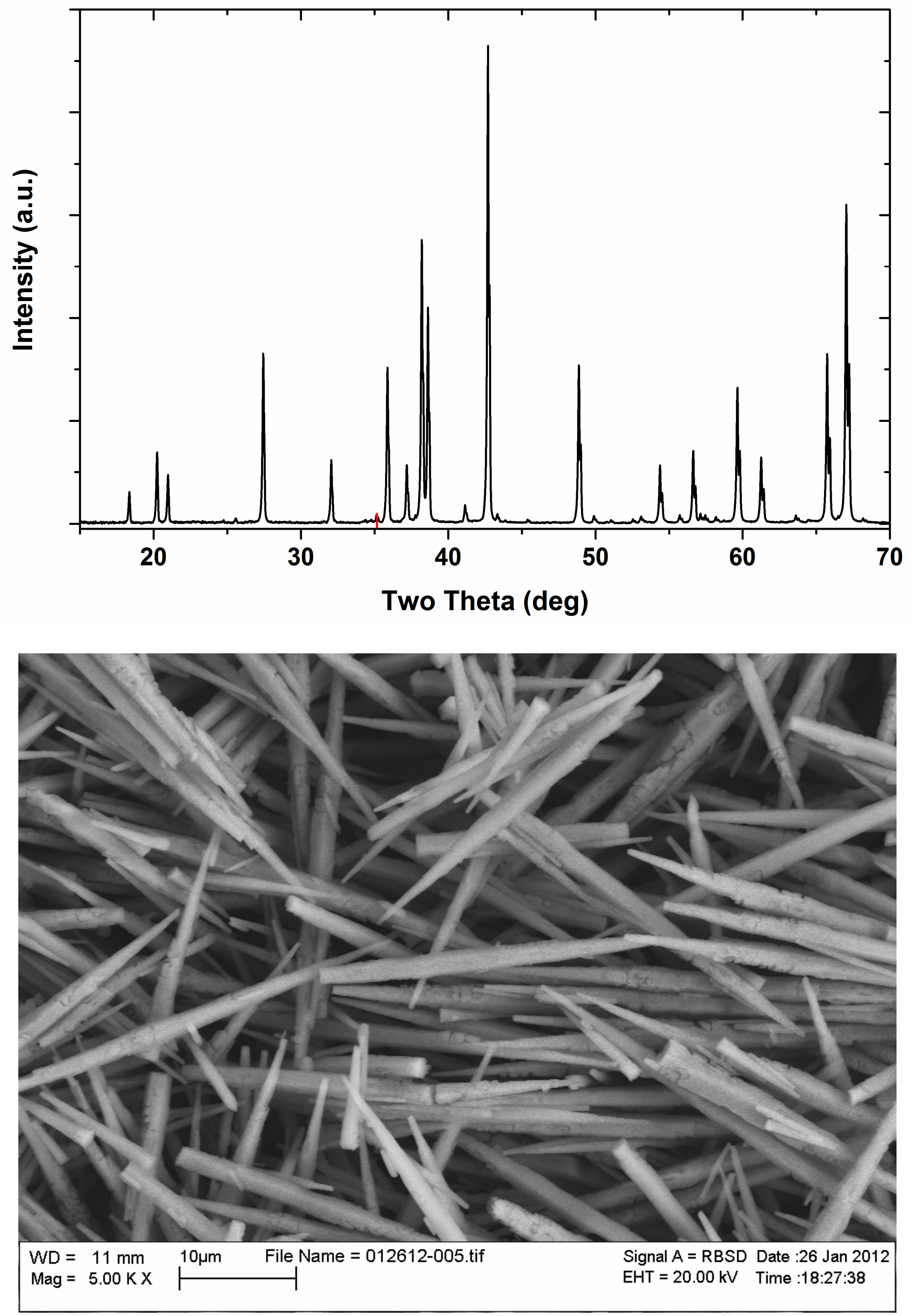

Figure 4. The PXRD pattern (top) and SEM image (bottm) of akdalaite synthesized from Al-floc showing only a minor impurity of corundum (red tick).

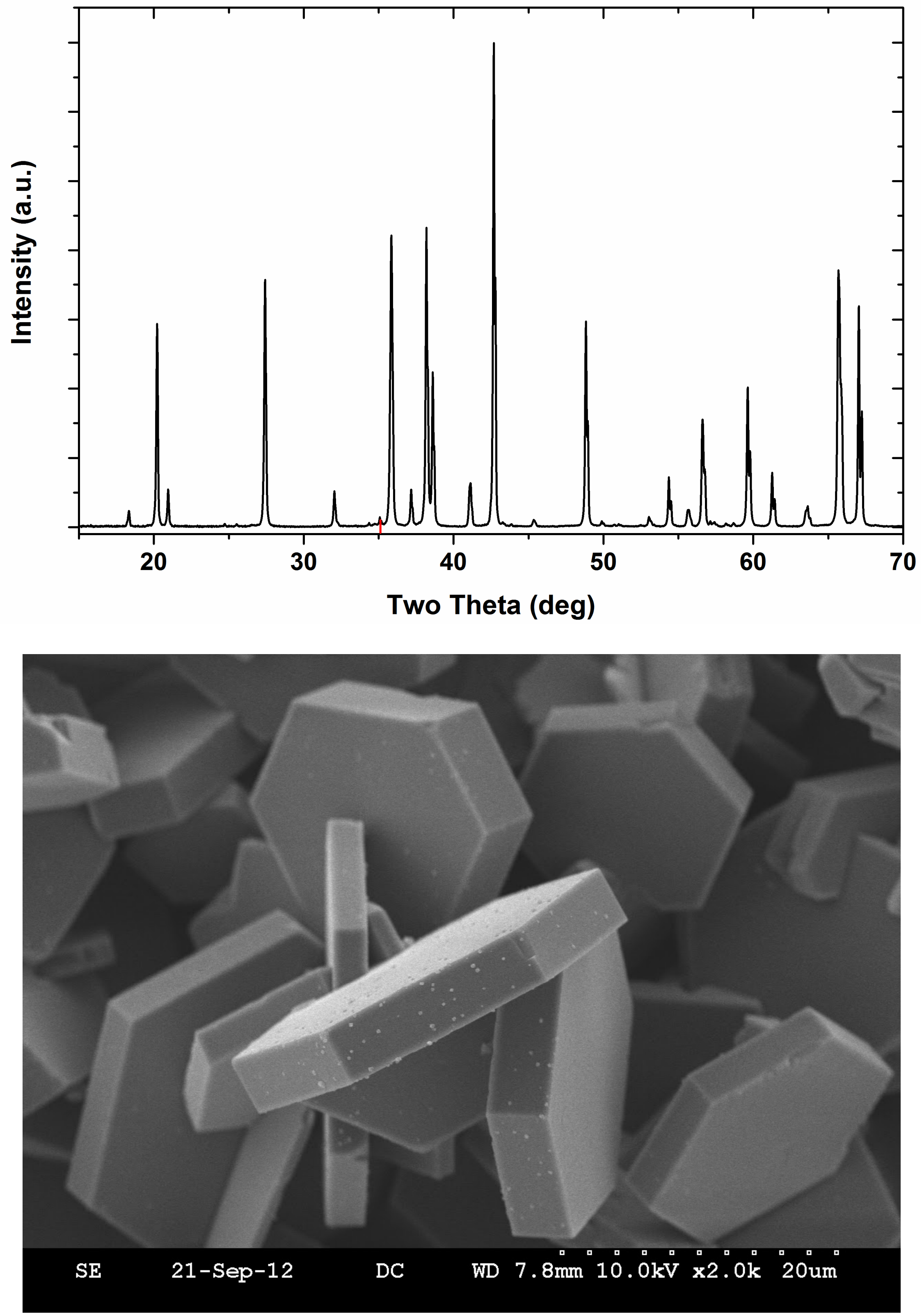

Figure 5. The PXRD pattern (top) and SEM image (bottom) of akdalaite synthesized from boehmite in 2 cm long capsule showing only a minor impurity of corundum (red tick).

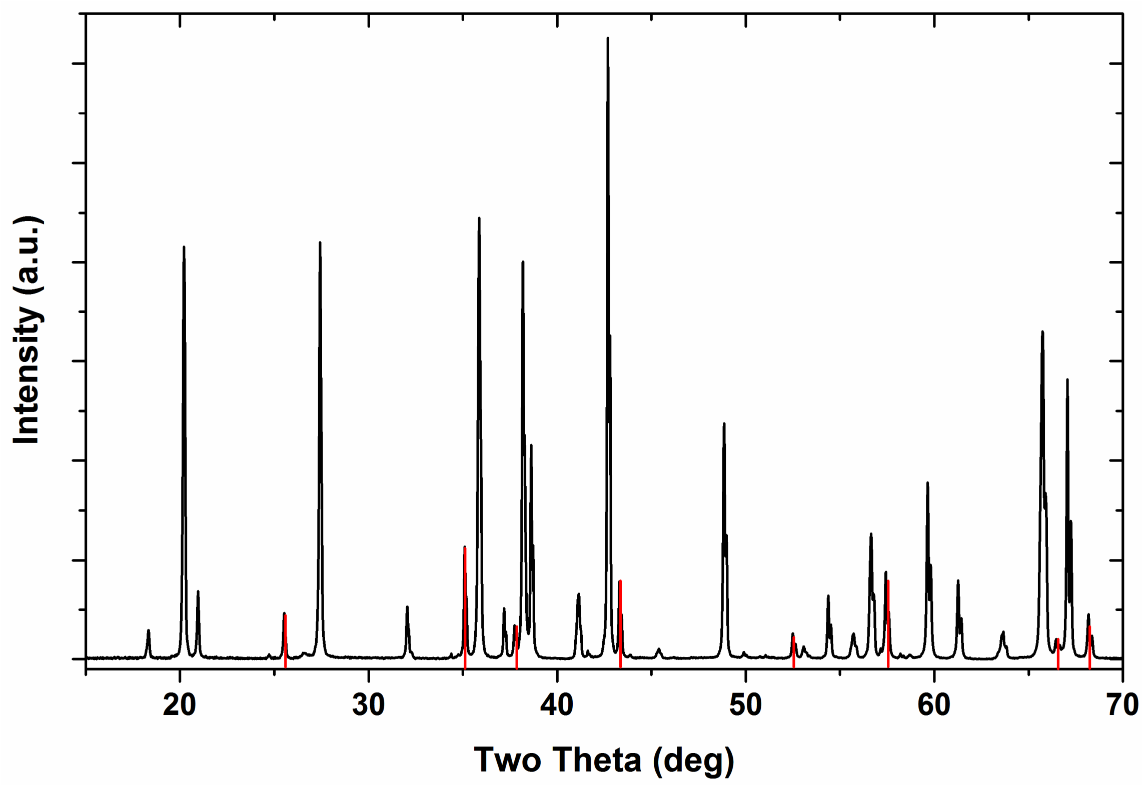

Figure 6. The XRD pattern of akdalaite synthesized from boehmite in 5.5 cm long capsule showing corundum (red tick) present as a minor phase.

Single Crystal X-ray Diffraction

A single crystal of akdalaite with hexagonal plate morphology was selected from the samples prepared from boehmite. The summary of akdalaite crystallographic data and SC-XRD structural refinement details is provided in Table 1 with the structure details and displacement parameters are in Tables 2 and 3. The crystal structure was solved using direct methods (SHELXS)[38] and inspection of the Wilson plot and the intensity weighted reciprocal lattice, including Bijovet pairs suggested the structure was acentric with point group 6mm. *Ab Initio* structure determination followed by least squares-Fourier cycling confirmed the accepted space group assignment and located the non-hydrogen atoms. Displacement parameters for all the non-hydrogen atoms were refined anisotropically. The hydrogen atoms were located from a Fourier difference map and geometrically constrained (DFIX command). The refinement using SC-XRD data confirmed the proposed structure of "tohdite" from 1969 and found residual electron density from hydrogen around site O1. The weak X-ray scattering from hydrogen did not allow a full refinement but did provide an adequate starting site position for neutron powder diffraction Rietveld refinements.

Table 1. Crystal data and structure refinement parameters

Sample	**akdalaite**
Empirical formula	Al_5HO_8
Formula weight	263.91
Collection Temperature (K)	100(2)
Wavelength (Å)	0.41328
Space Group	$P6_3mc$
a (Å)	5.5692(4)
b (Å)	5.5692(4)
c (Å)	8.7579(6)
Volume (Å^3)	235.24(4)
Z	2
Calculated density (g/cm^3)	3.726
Absorption coefficient (mm^{-1})	0.284
F(000)	260.0
Crystal size (mm)	0.02 × 0.02 × 0.005
Θ range of data collection (°)	2.46 - 17.16
Index range	$-7 \leq h \leq 5$
	$-5 \leq k \leq 7$
	$-12 \leq l \leq 12$
Total reflections	2719
Independent reflections	297
R_{int}	0.0492
Completeness to Θ_{max}	0.98
Goodness of fit	0.754
Data/restraints/parameter	305/2/33
R_1(on F_0, $I>2\sigma(I)$)	0.018
wR_2 (on F_0^2, all data)	0.0422

Table 2. Akdalaite structure details from SC-XRD refinement

Atom	Wych Pos.	x	y	z	Occ
Al1	6c	0.83433(4)	0.66866(7)	0.97784(6)	1
Al2	2b	1/3	2/3	0.76994(13)	1
Al3	2b	1/3	2/3	0.16065(10)	1
O1	2a	0	0	0.0971(3)	1
O2	6c	0.9721(2)	0.48606(10)	0.11316(13)	1
O3	6c	0.16594(11)	0.83407(11)	0.87424(14)	1
O4	2b	2/3	1/3	0.8670(2)	1
H1	2a	0	0	0.2073(6)	1

Table 3. Refined akdalaite anisotropic displacement parameters from SC-XRD data (Å^2 x 10^{-2})

Site	U_{11}	U_{22}	U_{33}	U_{23}	U_{13}	U_{12}
Al1	0.258(18)	0.24(2)	0.37(2)	0.016(13)	0.008(6)	0.118(11)
Al2	0.27(2)	0.27(2)	0.36(5)	0.0	0.0	0.133(12)
Al3	0.19(2)	0.19(2)	0.35(5)	0.0	0.0	0.097(12)
O1	0.25(5)	0.25 (5)	0.25(9)	0.0	0.0	0.12(3)
O2	0.23(4)	0.24(4)	0.38(7)	-0.008(19)	-0.02(4)	0.114(19)
O3	0.29(5)	0.27(6)	0.27(6)	-0.033(14)	0.033(14)	0.14(4)
O4	0.35 (7)	0.35(7)	0.28(10)	0.0	0.0	0.18(3)
H1*	Uiso = 2.5(13)					

*The H1 site was refined isotropically.

Neutron Powder Diffraction

Neutron powder diffraction data was collected on akdalaite to resolve the position of hydrogen and generate a complete akdalaite structure model. Hydrogen scatters X-rays very weakly so the position and displacement parameters cannot be sufficiently determined from X-ray diffraction data. However, hydrogen positions can be accurately determined form NPD as deuterium and hydrogen isotopes have favorable neutron scattering lengths (b_D = 6.67 and b_H = -3.74 fm). Hydrogen (^{1}H) is typically avoided in neutron scattering as it has a large incoherent cross section in comparison to deuterium. However, since akdalaite has such a small amount of structural hydrogen, the incoherent neutron scattering contribution is negligible. So as-synthesized hydrogenous akdalaite was used to collect NPD data. Aluminum and oxygen also have favorable neutron scattering contrast (b_O = 5.80 and b_{Al} = 3.45 fm) and thus a complete structural refinement can be conducted using NPD data.

Inspection of the NPD patterns (Figure 7) indicated it could be indexed on the basis of the unit cell determined from SC-XRD data. The cell parameters determined from the NPD data were are slightly larger than those determined from SC-XRD, reflecting the ~200 K difference in data collection temperatures. The final structure model from SC-XRD analysis (H omitted) was used as a starting point for NPD structure refinements with the GSAS/EXPGUI Rietveld software package.[39, 40] After the non-hydrogen atoms were refined aniostropically, a difference Fourier-map located the H atoms on the 3-fold axis in a similar position as assumed in SC-XRD model. However, a subsequent anisotropic refinement of the H-site displacement parameters revealed a distribution of nuclear density smeared in a disk shape perpendicular to the 3-fold axis, indicating the H atoms deviate from the ideal site (Figure 8). This is suggestive of the type of H-site disorder common in hydroxide minerals [portlandite – $Ca(OH)_2$, brucite – $Mg(OH)_2$, and pyrochroite –

$Mn(OH)_2$] where the hydrogen atoms deviate from the three-fold axis creating a split site with partial occupancy.[41-43] The refinement details using a single hydrogen site and a split occupancy site are shown in Table 4. A split site model with H partially occupying (1/3) three equivalent sites around the 3-fold axis slightly improved the fit to the data and produced typical thermal displacement parameters in describing the H motion (Figure 8). The split-site refinement indicates the H atoms deviate from the axis due to hydrogen bonding with the O3 site. The structure of the akdalaite model with the split hydrogen site is detailed in Table 5 with the displacement parameters in Table 6 and the details of the hydrogen bonding environment shown in Figure 9.

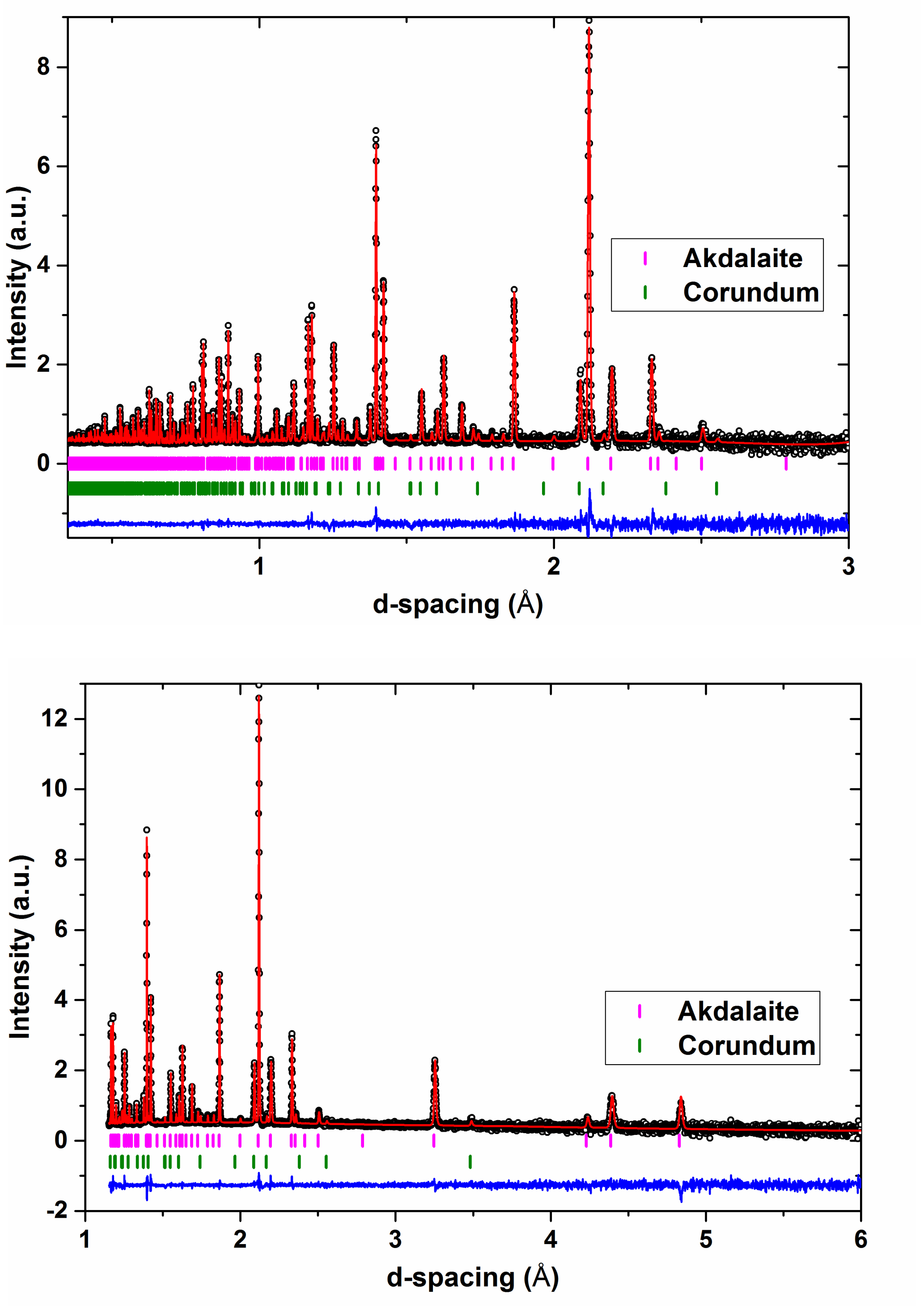

Figure 7. Rietveld refinement results of NPD frame 2 (top) and 5 data (bottom). Akdalaite = 89.15 wt% and corundum = 10.85 wt%.

Table 4. Neutron Rietveld Refinement Results for Akdalaite

	Single H Site	Split H Site
Space Group	$P6_3mc$	$P6_3mc$
a (Å)	5.576377(9)	5.576376(9)
b (Å)	5.576377(9)	5.576376(9)
c (Å)	8.77275(4)	8.77275(4)
Volume (Å^3)	236.2490(10)	236.2490(10)
Frame 2 R_p	0.0701	0.0701
Frame 2 wR_p	0.0401	0.0400
Frame 5 R_p	0.0919	0.0918
Frame 5 wR_p	0.0583	0.0582
$\chi 2$	2.174	2.168

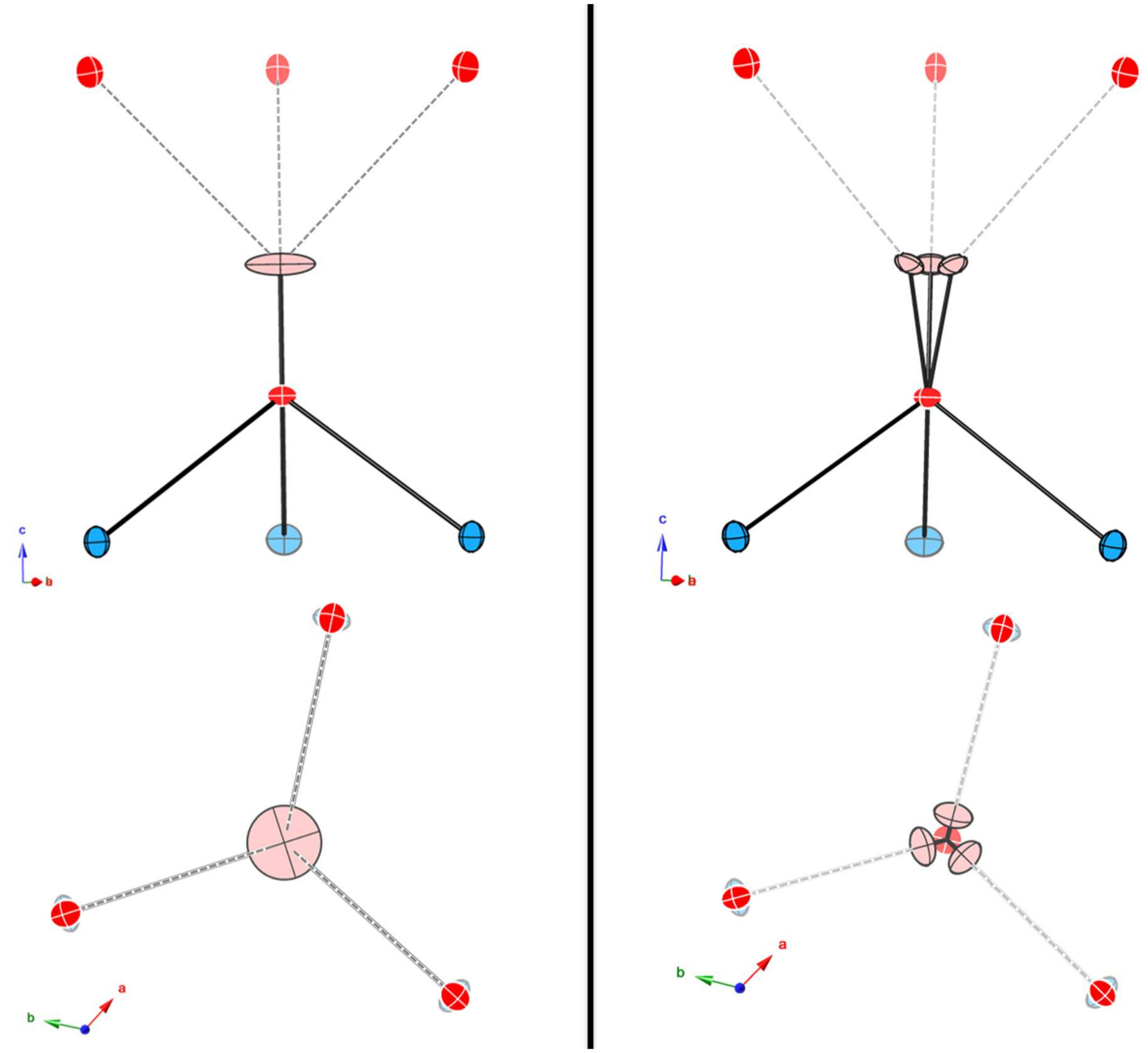

Figure 8. Anisotropic displacement ellipsoids around the hydrogen environments from NPD Rietveld refinements as shown perpendicular to (top) and looking down (bottom) the *c* axis. (left) single site model (right) split-site model. The oxygen ellipsoids are in red, aluminum in blue, and hydrogen in beige. Gray dashed lines represent the hydrogen bonding between H1 and O3 site.

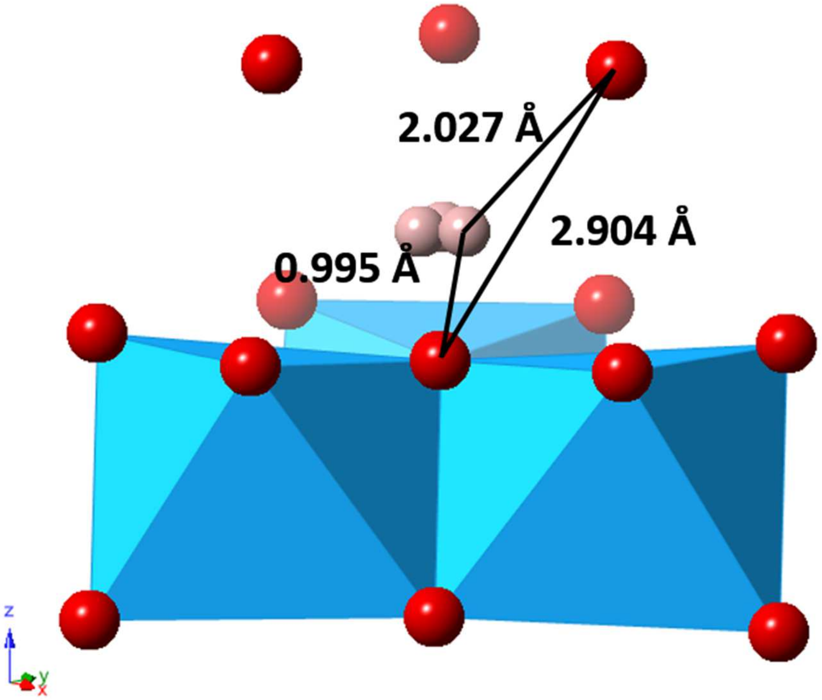

Figure 9. Split hydrogen site of akdalaite with bond distances. Aluminum (Al1) octahedra are blue, oxygen atoms are red, and the hydrogen atoms are beige. The three possible positions of the split hydrogen site are shown. The O-H-O bond angle is 145.78°.

Table 5. Akdalaite structure details from neutron powder diffraction refinement

Atom	Wych Pos.	x	y	z	Occ
Al1	6c	0.83410(16)	0.66820(33)	0.9748(4)	1
Al2	2b	1/3	2/3	0.7665(5)	1
Al3	2b	1/3	2/3	0.1579(4)	1
O1	2a	0	0	0.0958(4)	1
O2	6c	0.97202(15)	0.48601(8)	0.11169(32)	1
O3	6c	0.16665(27)	0.83335(27)	0.87138(32)	1
O4	2b	2/3	1/3	0.8657(4)	1
H1	6c	0.0377(15)	0.0189(8)	0.2073(6)	0.33

Table 6. Refined akdalaite anisotropic displacement parameters from NPD data (Å^2 x 10^{-2})

Site	U_{11}	U_{22}	U_{33}	U_{23}	U_{13}	U_{12}
Al1	0.70(5)	0.31(5)	0.58(6)	-0.06(6)	-0.029(29)	0.155(25)
Al2	0.40(7)	0.40(7)	0.83(13)	0.0	0.0	0.200(35)
Al3	0.64(4)	0.64(4)	0.26(10)	0.0	0.0	0.319(21)
O1	0.58(5)	0.58 (5)	0.32(7)	0.0	0.0	0.288(24)
O2	0.509(30)	0.495(28)	0.70(4)	-0.109(19)	-0.22(4)	0.255(15)
O3	0.440(32)	0.440(32)	0.71(4)	-0.005(16)	0.005(16)	0.13(5)
O4	0.61(6)	0.61(6)	0.22(8)	0.0	0.0	0.304(30)
H1	0.90(29)	1.08(17)	0.34(12)	0.10(6)	0.20(13)	0.45(15)

Solid State Nuclear Magnetic Resonance

Solid-state NMR data give additional insight to the local environments of Al and H in akdalaite and confirm the akdalaite structure solved from SC-XRD and further refined from NPD. The ^{27}Al MAS NMR spectra of synthetic and natural akdalaite (Figure 10) indicate both samples have six and four coordinate Al. For the synthetic sample, the tetrahedral Al gives a signal from +65 to +35 ppm, broadened by second-order quadrupolar effects. The six coordinated Al yields a complex feature from +20 to -10 ppm. The resonances in the synthetic spectrum display sharp features owing to the high crystallinity and purity of the sample while the spectrum of the natural sample contains signal in the same shift regions but is less resolved due to contributions from paramagnetic impurity elements in akdalaite as well as the other accessory phases that comprise the sample (σ-Al_2O_3, fluorite, and mica). Additional minor, narrow peaks for four-coordinate Al occur in the spectrum of the synthetic sample at +72 and +67 ppm that likely arise from impurities, but which cannot be assigned to any known phase based on literature data.

The synthetic sample was further studied with ^{27}Al MQ/MAS to determine the number and proportion of distinct Al sites in akdalaite. The spectra from the ^{27}Al MQ/MAS study revealed three distinct Al sites, 2 octahedral and 1 tetrahedral (Figure 11), with isotropic peaks at 11.5, 23.4, and 77.5 ppm in *F*1 (vertical axis in Figure 11). Simulation of the separate *F*2 cross-sections to second-order quadrupolar peak shapes (Figure 11, right panel) yielded the chemical shift (δ_{iso}), quadrupolar coupling constant (Cq), and asymmetry parameter (η) for each resolved site, compiled in Table 7. These values were then used to fit the quantitative MAS spectrum to a sum of second-order quadrupolar center bands, yielding an Al site distribution of 59% ± 2 for the Al1 octahedral site, 22% ± 2 for the Al2 octahedral site, and 20% ± 2 for the Al3 tetrahedral site, in reasonable agreement with the X-ray and neutron derived models.

The ^{1}H NMR spectrum consists primarily of a single, narrow central peak at +8.6 ppm, with two spinning sidebands in Figure 12. A small shoulder near +6.5 ppm (< 5% intensity) likely arises from an impurity phase and/or surface adsorbed water. The single, well-resolved central peak indicates a single H site and the small peak width (600 Hz) observed at this modest spinning rate (15 kHz) indicates a small homonuclear dipolar coupling characteristic of low hydrogen density.[44, 45] In this chemical shift range, the literature data for ^{1}H indicate a good linear correlation with *d*(O…O) hydrogen bond lengths,[44] although the relationship between chemical shift and hydrogen bond distance can be expected to reflect also other geometrical factors such as H-O distance and O-H…O angle. With that caveat, the observed akdalaite shift is similar to that of diaspore (α-AlOOH) which has a shift at +9.4 ppm and an O···O distance of ~2.65 Å.[44] Therefore, ^{1}H MAS akdalaite spectrum is interpreted to indicate the presence of a single hydrogen site with an O···O distance near 2.65 Å, which is in agreement with the hydrogen location derived from neutron powder diffraction (Figure 9).

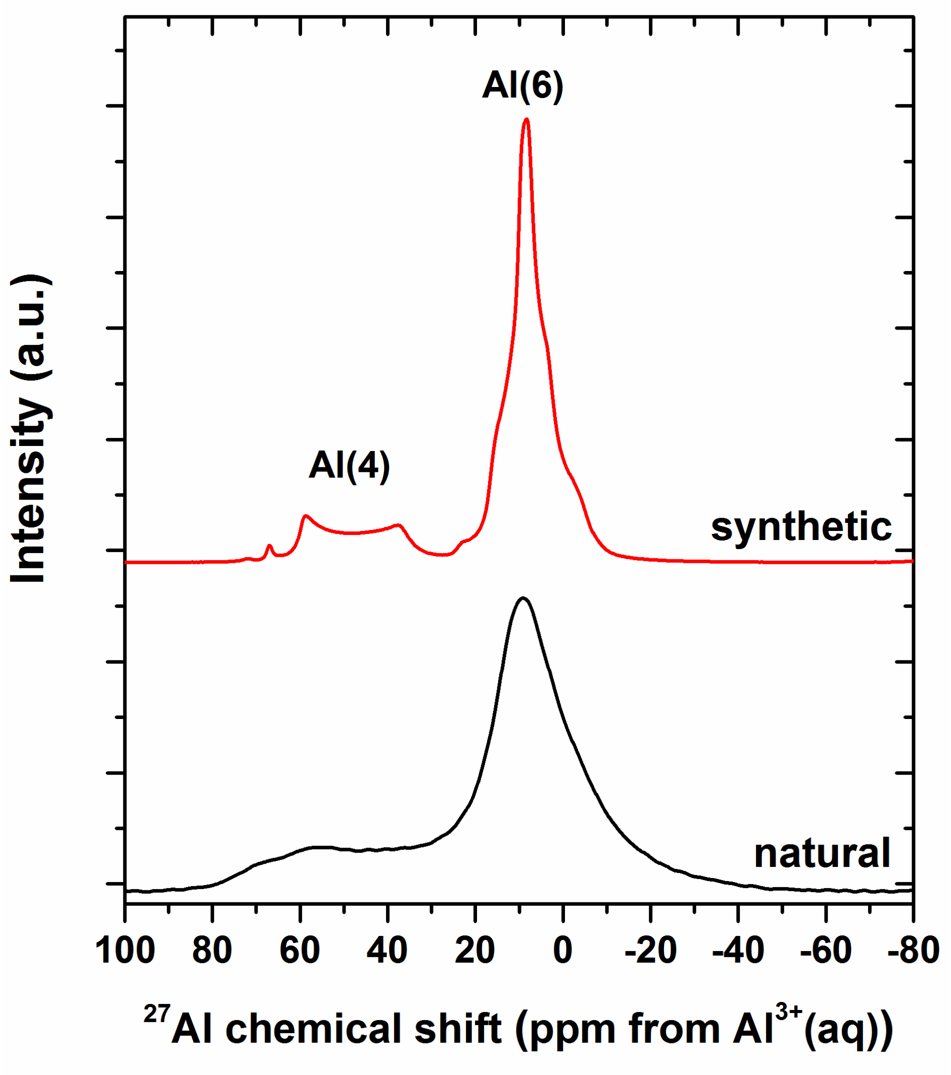

Figure 10. ^{27}Al MAS NMR spectra of synthetic crystalline akdalaite and natural akdalaite (Solnechnoye locality). Peaks for octahedral and tetrahedral aluminum are marked. The Al(4) peak at +70.5 ppm represents a tetrahedral site from an impurity.

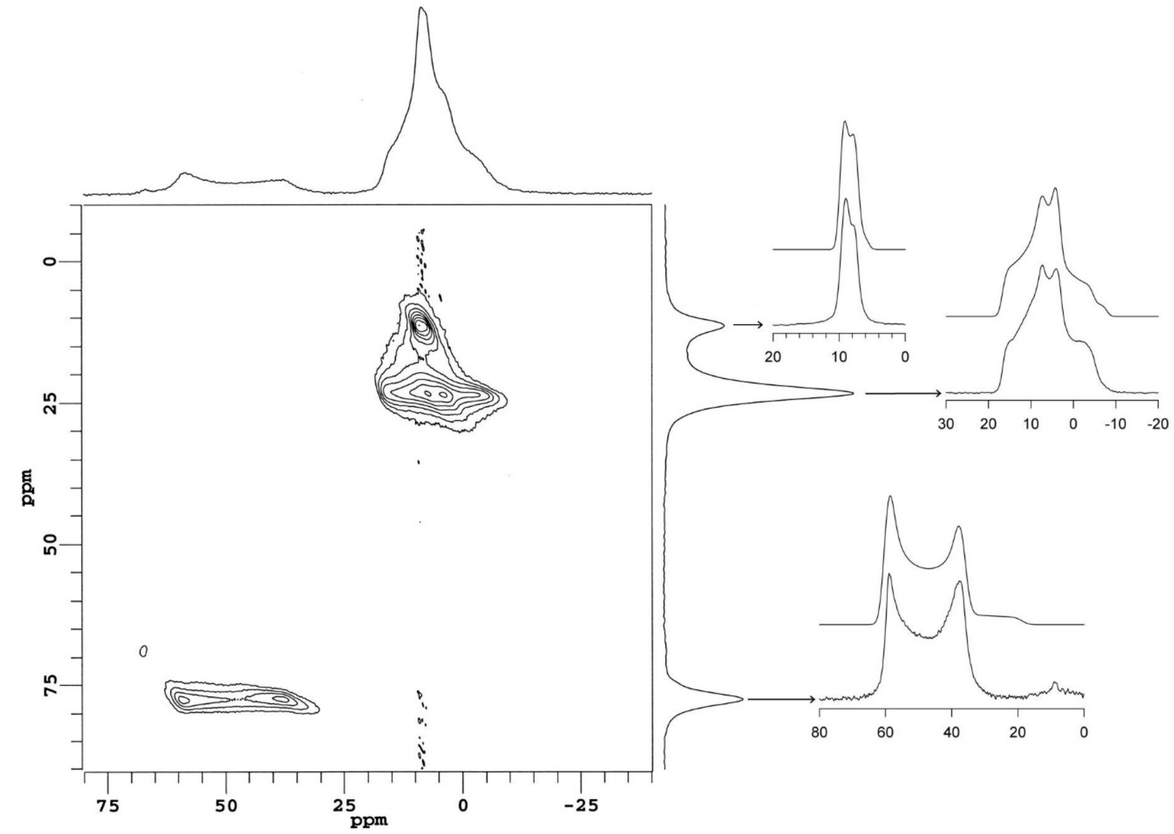

Figure 11. ^{27}Al MQ/MAS NMR spectrum of synthetic akdalaite. The top spectra is the MAS dimension while the right spectra is the isotropic dimension. The individual site spectra are shown on the far right with the simulated spectra above the experimental.

Table 7. ^{27}Al NMR parameters for synthetic akdalaite, obtained from simulation of the *F*2 cross-sections of the ^{27}Al MQ/MAS NMR spectrum (Figure 11). Estimated uncertainties are ±0.2 ppm for the isotropic chemical shift (δ_{iso}), ±0.1 MHz for the quadrupolar coupling constant (Cq), and ±0.1 for the asymmetry parameter (η). $\delta_{F1,obs}$ is the observed peak position in the MQ/MAS *F*1 dimension (vertical spectrum in Figure 11), whereas $\delta_{F1,calc}$ is calculated from the fitted quadrupolar coupling parameters.

Site	Type	δ_{iso} (ppm)	Cq (MHz)	η	$\delta_{F1,calc}$ (ppm)	$\delta_{F1,obs}$ (ppm)
Al1	octahedra	17.0	5.1	0.7	23.3	23.4
Al2	octahedra	10.3	2.3	0.2	11.4	11.5
Al3	tetrahedra	66.5	7.3_5	0	77.7	77.5

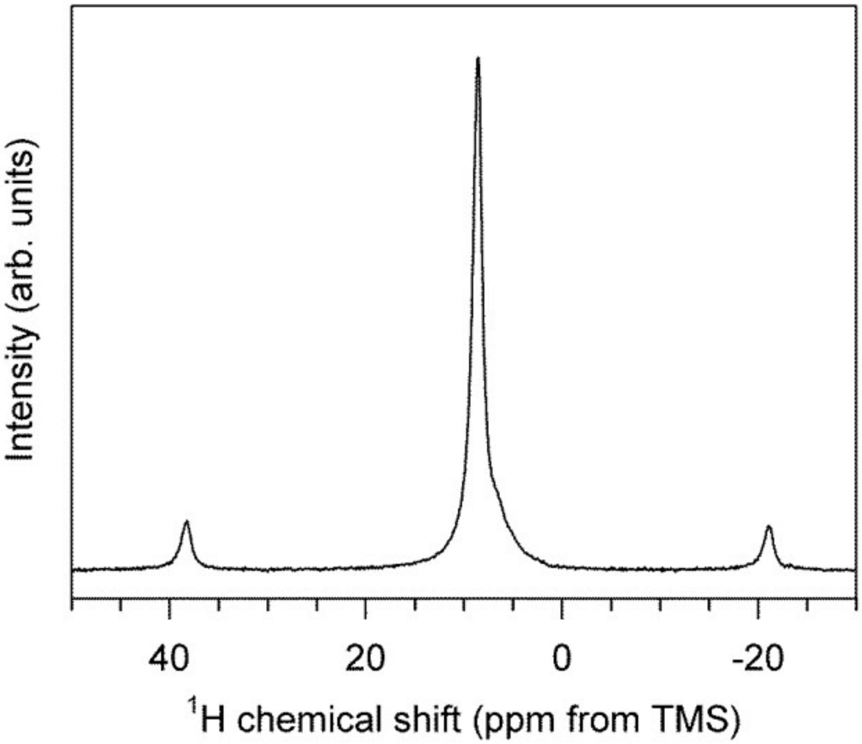

Figure 12. ^{1}H MAS NMR spectra of synthetic akdalaite. The central peak has a chemical shift of +8.6 ppm. Spinning side bands shown outside central peak.

Crystal Chemical Analysis

The results from SC-XRD, NPD, and NMR were used to form a complete structural model of akdalaite that includes the hydrogen positions. The bond valence sums (BVS) were calculated in the same manner as ferrihydrite where the total site valence (V_i) is the sum of valences (S_{ij}) associated with the bond between atoms i and j.[46-48] The individual bond valences are calculated using Equation 1 with the experimentally determined bond lengths (R_{ij}) and the empirical constants R_0 and b which have been determined from valence analysis of known compounds. For Al – O bonds, $R_0 = 1.651$ and b = 0.37.[12, 46]

$$V_i = \sum_j S_{ij} = e^{(R0-Rij)/b} \tag{1}$$

The atom bond lengths and bond valence sum of the aluminum and oxygen site are listed in Tables 8 and 9 and overlaid on the structure in Figure 13. The contribution of hydrogen to the oxygen bond valence was accomplished using different empirical constants for the shorter donor O-H and longer acceptor O•••H bonds (Table 10). Previous studies found that hydrogen bonding is unlike typical cation – anion interactions and the hydrogen bonding interactions have to be treated differently.[47-49] The aluminum sites show signs of under and over bonding as the BVS of the tetrahedral site (Al3) is under bonded at 2.68, below the ideal value of 3 for aluminum. The octahedral aluminum sites of Al1 and Al2 are closer to ideal being 3.07 and 2.89 respectively. This is similar to Fe BVS of the ferrihydrite model (Figure 1) where the octahedral sites are 2.97 while the tetrahedral site is under bonded at 2.74.

The oxygen BVS sums also have a similar trend to the ferrihydrite model as sites O1, O2, and O3 are all under bonded while O4 is over bonded at 2.25. The hydroxyl oxygen (O1) has an understandably low BVS at 1.44 prior to accounting for hydrogen bonding. But while O2 is slightly under bonded at 1.93 like in ferrihydrite, the O3 BVS is smaller at 1.76. After accounting for hydrogen bonding, the O1 BVS jumps to 2.08 as the O3 increases to a more reasonable 1.93 (Table 10).

In addition to non-ideal bond valence sum, some of the Al bonding environments in akdalaite have unexpected characteristics like that observed in the ferrihydrite model (Figure 14). In analyzing the Al – Al bond distances (Table 11), the Al1 – Al1 bond distance between the edge sharing octahedra is 2.775 Å, much shorter than the other edge sharing octahedra where the Al1 – Al2 bond distance is 3.027 Å. The short edge sharing distance between Al1 – Al1 borders on that of the Al octahedral face sharing distance of corundum at 2.654 Å and is ~9% shorter than the other edge sharing Al1 – Al2 distance. In ferrihydrite, the Fe1 – Fe1 bond distance is 2.907 Å, which is ~11% shorter than the other shared edge Fe1 – Fe2 bond distance of 3.261 Å much like the Al sites in akdalaite. However, this Fe1 – Fe1 edge sharing distance is only slightly larger than the Fe octahedra face sharing distance in hematite (2.895 Å).[13, 50]

The Al2 octahedra in akdalaite are also distorted in that the Al is off center so much that three of the Al – O bond distances are only 1.854 Å which are very close to the tetrahedral bond distances of 1.823 Å and 1.791 Å (Figure 14). The ferrihydrite Fe2 octahedral distortion (Figure 14) also results in uncharacteristically short Fe – O distances of 1.881 which in turn are shorter than some of the tetrahedral Fe – O distances (1.931 Å). The atypical bonding at the Al2 site observed in akdalaite is also present at the Fe2 site in the ferrihydrite model, but to the point of violating accepted principles.[14]

Thorough crystal chemical analysis has revealed most of the anomalous aspects of the ferrihydrite model are intrinsic to the akdalaite structure. The only oddity not observed in the akdalaite structure that ferrihydrite model was criticized for is the distorted edge sharing O – O bonding distances between the Fe1 sites where the shared edge was longer than the unshared edge

(Figure 2). The Al1 octahedra have the expected shorter O – O distances on the shared edge (2.543 Å) in comparison to the unshared edge (2.697 Å) in accordance with Pauling's distortion rule (Figure 14).[51] Otherwise, the anomalous crystal chemical trends that are observed in akdalaite are present in the ferrihydrite model, though exacerbated, which is likely due to how the model was refined from PDF data.

It was emphasized in the original single-phase model refinement that, while the structure of ferrihydrite can be described by an idealized periodic model, real-space fitting does not account for "second-order effects such as disorder, surface relaxation, internal strain, defects (e.g., stacking faults), particle shape, and/or interparticle correlations may also contribute to the experimental PDFs."[10] The single-phase ferrihydrite models were refined from X-ray PDF data using the program PDFgui.[7] However, PDFgui only refines a unit cell and treats the particle shape as a sphere regardless of the actual morphology, allowing the refinement of the radius. The PDF patterns of nanoparticles are heavily influenced by the size and morphology of the particles as this will weight some pair correlations more than others.[20, 52, 53] The incorrect treatment of nanoparticle morphology, such as modelling ferrihydrite as a sphere when it is a flat plate, can result in model distortions in order to better fit the data.

As the nanoparticles of ferrihydrite have a high surface area, surface interaction and relaxation will also have a significant impact on the total scattering. In crystals and crystallites, the surface area to volume ratio is so small that surface structure will have a negligible contribution to the scattering. But in the case of nanoparticles like ferrihydrite, the surface comprises a significant portion of the structure and surface contribution to the total scattering is no longer minor. A recent of ferrihydrite surface structure elucidated the Fe sites exposed at the surface are dominantly the Fe1 octahedra.[21] The shorter than expected Fe1 – Fe1 distance and distortion of the Fe1 octahedra is likely due to the strains placed on the sites at the surface of ferrihydrite particles. Thus, surface interactions and relaxation will preferentially distort the Fe1 octahedra and the distortions on the surface will have a significant contribution to the total scattering and PDF. Thus, when a unit cell approach to modeling the total scattering and PDF is used, the bulk Fe1 site will appear distorted due to the contributions of distorted Fe1 octahedra at the surface – the bulk and surface Fe1 sites are average in such an approach. While the previous critiques of the ferrihydrite crystal chemistry were originally valid, crystal chemical analysis has shown that these are inherent characteristics of the akdalaite model and exacerbated distortions likely arise from the non-ideal treatment of PDF data during model refinement.

Table 8. Akdalaite aluminum bond valence sums

Sites	^{VI}Al1			^{VI}Al2			^{IV}Al3			Type
	d(Å)	mult	BV	d(Å)	mult	BV	d(Å)	mult	BV	
O1	1.922	1	0.4807							O-H
O2	1.961	2	0.8652	2.005	3	1.1524	1.791	3	2.0549	
O3	1.845	2	1.1839	1.854	3	1.7332				O···H
O4	1.879	1	0.5400				1.823	1	0.6282	
Al BV Σ			3.07			2.89			2.68	

Table 9. Akdalaite oxygen bond valence sums

Sites	^{VI}Al1			^{VI}Al2			^{IV}Al3			BV Σ	Type
	d(Å)	mult	BV	d(Å)	mult	BV	d(Å)	mult	BV		
O1	1.922	3	0.4807							1.44	O-H
O2	1.961	2	0.8652	2.005	1	0.3841	1.791	1	0.6850	1.93	
O3	1.845	2	1.1839	1.854	1	0.5777				1.76	O···H
O4	1.879	3	1.6200				1.823	1	0.6282	2.25	

Table 10. Akdalaite oxygen bond valence sums with hydrogen contribution

Site	O-H d(Å)	R_0	b	BV	O BV	O BV Σ	Type
O1	0.995	0.569	0.94	0.6356	1.44	2.08	O-H
O2					1.93	1.93	
O3	2.027	0.99	0.59	0.1725	1.76	1.93	O···H
O4					2.25	2.25	

Table 11. Metal – metal distances in akdalaite and ferrihydrite models

Atom Pair	Type	d (Å)
Akdalaite		
Al1 – Al1	Edge	2.775
Al1 – Al2	Edge	3.027
Al1 – Al2	Corner	3.334
Ferrihydrite		
Fe1 – Fe1	Edge	2.907
Fe1 – Fe2	Edge	3.261
Fe1 – Fe2	Corner	3.409

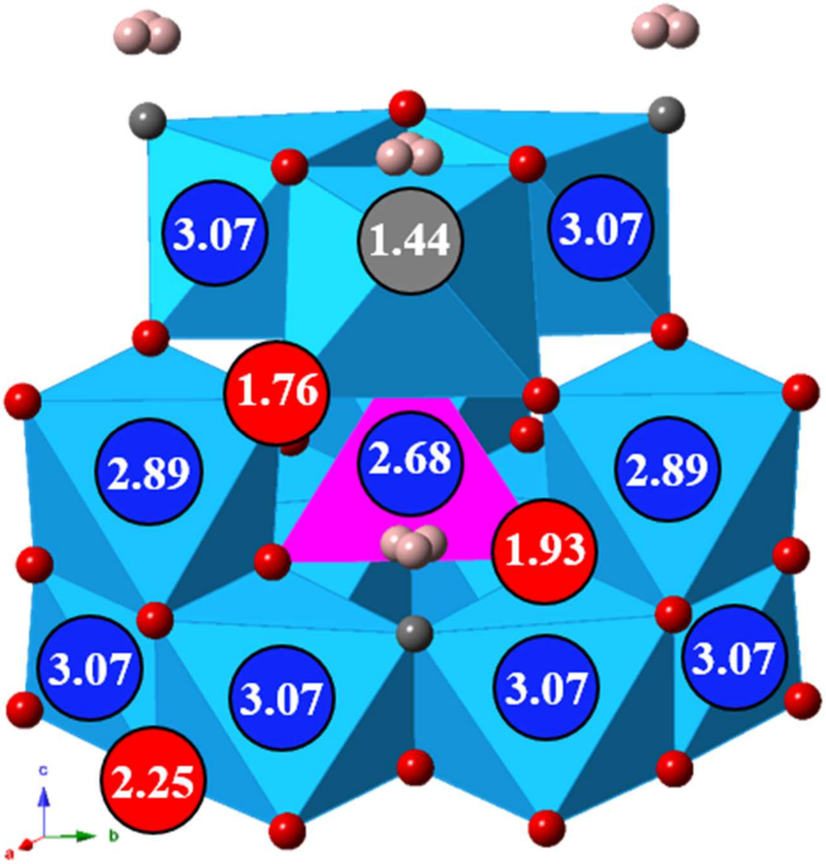

Figure 13. Structure of akdalaite refined from NPD data shown in the δ-Keggin motif with the calculated bond valences sums of each site prior to adding contributions from hydrogen. The Al octahedra are blue, the tetrahedral Al is purple, oxygen atoms are red, hydroxyl is gray, and hydrogen atoms are beige.

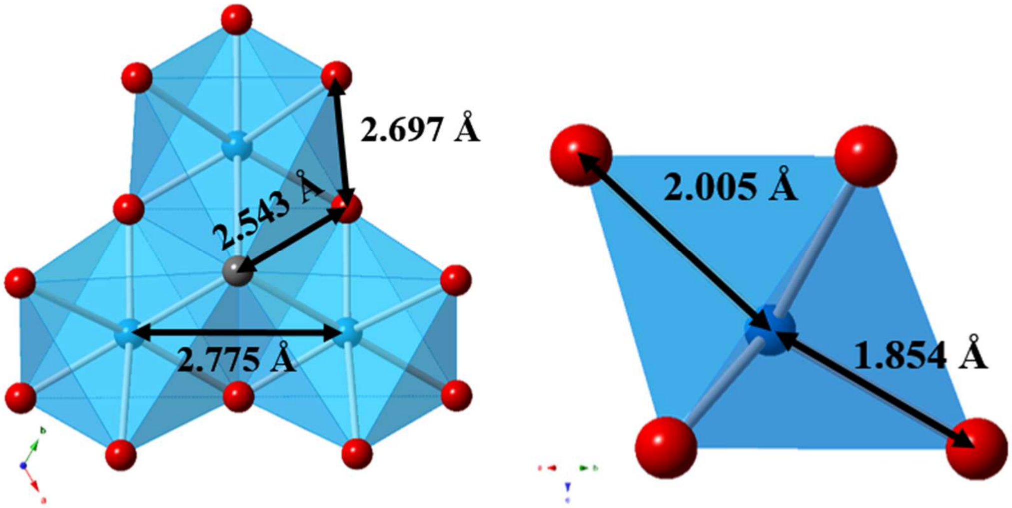

Figure 14. (left) The connectivity of the octahedral Al1in akdalaite site with the Al1 – Al1 distance as 2.775 Å, shared edge O1 – O3 distance of 2.543 Å, and unshared edge O3 – O2 distance of 2.697 Å. (right) The connectivity of the Al2 site. The Al2 site is not centered in the octahedra resulting in Al – O distances of 1.854 Å and 2.005 Å.

X-ray Total Scattering and Pair Distribution Function Analysis

Crystalline akdalaite was studied with X-ray total scattering so as to compare the real space PDF to that of 6-line ferrihydrite (6 nm diameter particles) and evaluate the structural relationship between the two compounds. The PDF of two isostructural compounds cannot be compared directly as the difference in the metal-oxygen (M-O) distances will propagate through the PDF, increasing the off-set of related pairs with distance.

The differences in M-O distance can be accounted for in an empirical manner by comparing the PDFs of known crystalline structural analogs. Corundum (Al_2O_3) and hematite (Fe_2O_3) were chosen to determine the shift in pair correlations between aluminum and ferric iron as the structure has a mix of edge, corner, and face sharing octahedra. There is no ideal Al and Fe analog that has both octahedral and tetrahedral coordination with only +3 metal oxidation states. The PDFs for corundum and hematite were calculated from structure files using the program PDFgui with a Q_{max} of 25 $Å^{-1}$.[7, 50, 54] The overlaid PDFs of corundum and hematite are show in Figure 15. While being structurally analogous, the intensity of the related peaks in the PDFs are very different as the intensity still a function of the scattering power of the atoms. From the PDFs, the r-shift (Fe – Al Δr) for identical peaks is plotted as a function of average distance of those peaks in r (Figure 16). There is a strong linear correlation between the amount of r-shift between equivalent peaks and distance so the equation of the trend line in Figure 16 becomes the r-shift equation (Equation 2) to apply to Al compound PDFs to equate to Fe compounds. The new distance (r_n) is determined after applying the trendline equation as a function of original distance (r_o).

$$r_n = r_o + [(0.0561 * r_o) + 0.0157] \tag{2}$$

The PDF of corundum was shifted using Equation 2 and is shown with the PDF of hematite in Figure 17. It now becomes clear that corundum and hematite are isostructural as the peaks in the PDF now overlay each other. The peak position alignment is not perfect after applying the r-shift to corundum as it is an empirical correction but nonetheless is a powerful approach for comparing structurally analogous compounds.

At a first glance, the PDF patterns of crystalline akdalaite and 6 line (6 nm) ferrihydrite (data from [55]) appear to have nothing in common (Figure 18, top). However, after the akdalaite data is shifted using the empirical Al-Fe r-shift equation (Equation 2) derived from the corundum – hematite data, the peaks in both data sets align (Figure 18, middle). The patterns are easiest to compare when they represent the same size regime as well. The akdalaite data was additionally enveloped to mimic the data of spherical nanoparticle with a diameter (d) of 30 Å using the envelope function (f_e) of Equation 3 which is multiplied to the akdalaite G(r).[56] The $\Theta(d - r)$ term is a step function that eliminates distances outside the particle diameter as it is 1 when r < d, and 0 otherwise.

$$f_e(r,d) = \left[1 - \frac{3}{2}\frac{r}{d} + \frac{1}{2}\left(\frac{r}{d}\right)^3\right]\Theta(d - r) \qquad (3)$$

In comparing the akdalaite data that has been linearly shifted and enveloped to a comparable particle size of ferrihydrite (Figure 18), it becomes obvious that the PDF patterns are extremely similar and share a common structure. These similarities between the adjusted akdalaite and 6 line ferrihydrite PDFs provide new evidence that ferrihydrite and akdalaite are indeed isostructural.

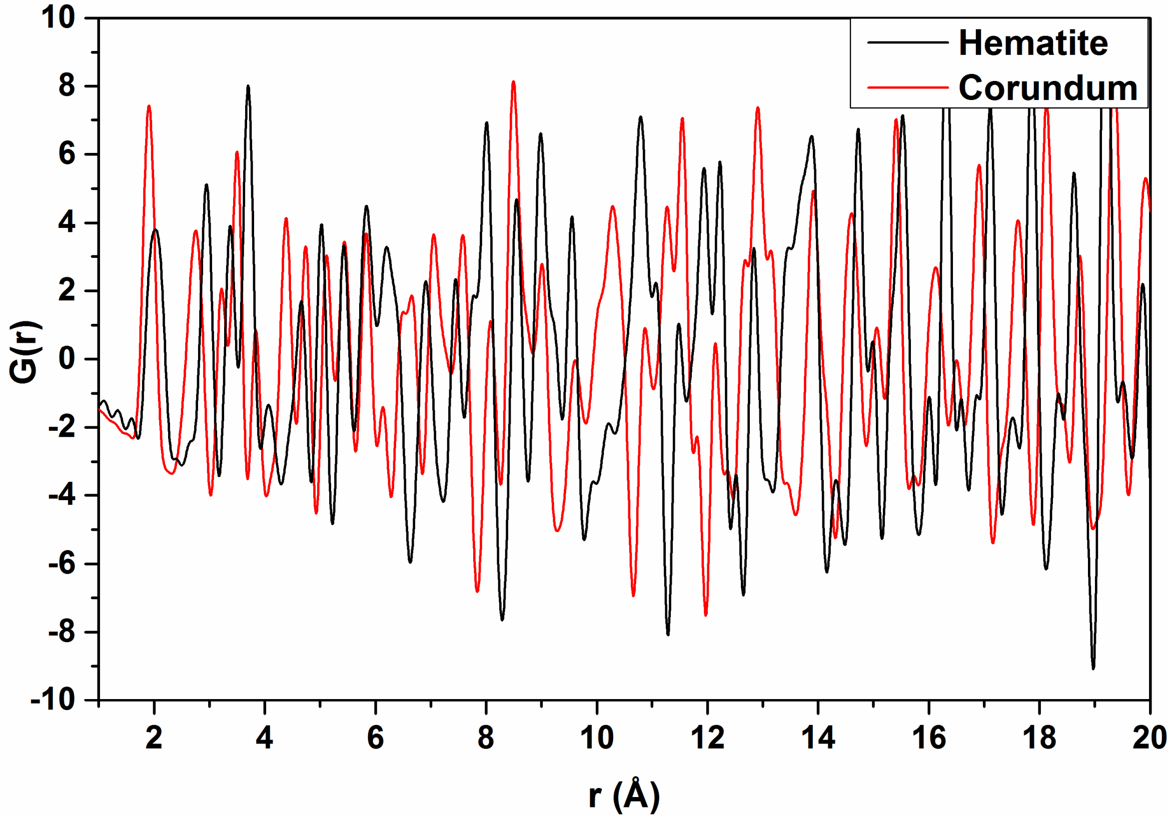

Figure 15. Calculated PDFs of hematite and corundum.

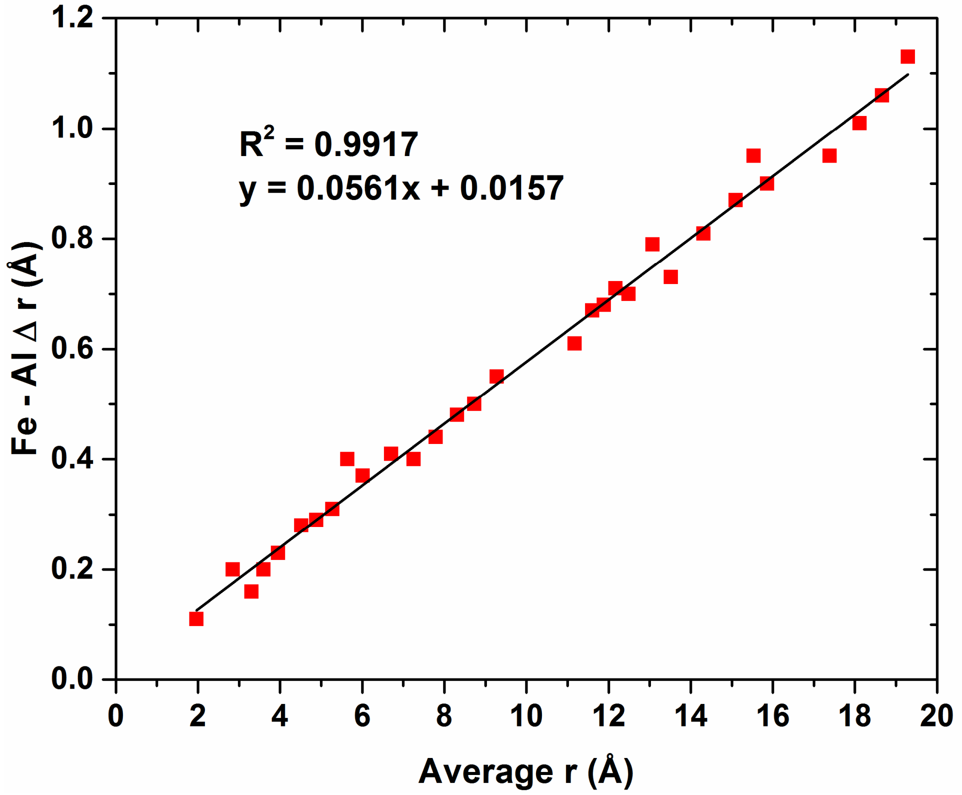

Figure 16. Plot of the r-shift of identical peaks in the calculated PDFs of hematite and corundum.

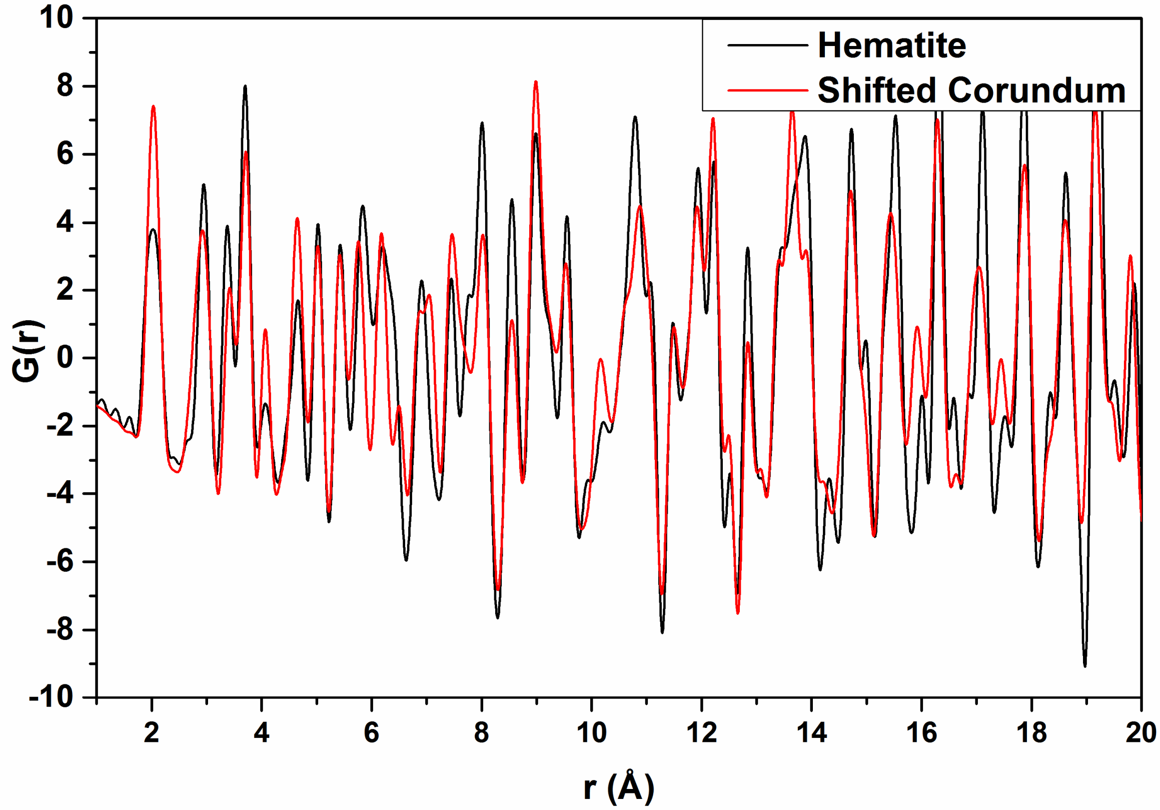

Figure 17. Calculated PDFs of hematite and corundum after the corundum data has been shift to account for the different M-O differences with the fitted linear r-shift equation (Equation 2).

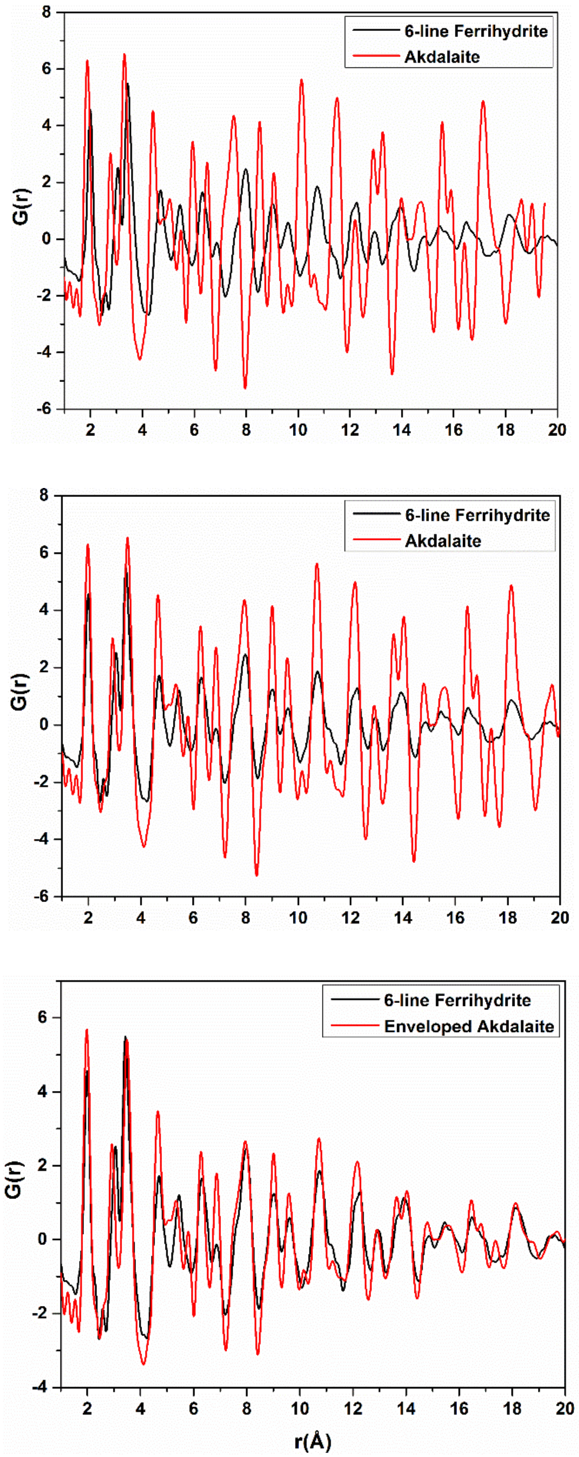

Figure 18. (top) Comparison of X-ray PDF data from crystalline akdalaite and 6-line ferrihydrite. (middle) X-ray PDF data from 6-line ferrihydrite and r-shifted akdalaite which has been adjusted to have approximately equivalent M-O distances as Fe-O. (bottom) Same shifted data as middle but the akdalaite data has had a spherical envelope function applied so intensities are representative of a 3 nm spherical particle.

Conclusions

Through a combined study of akdalaite with SC-XRD, NPD, and NMR a complete structural model of akdalaite has been created. The hydrogen site is best described as a split site about the three-fold axis with 1/3 occupancy. Crystal chemical analysis revealed abnormal bond valences with over and under bonding of atoms within the structure as well as unexpectedly close octahedral edge sharing Al atoms at the Al1 site and distortions at the Al2 site. This revealed the criticized crystal chemical anomalies of the single-phase ferrihydrite model are inherent to akdalaite structure and plausible "violations." Further study with X-ray total scattering provided additional evidence that the akdalaite structure model is appropriate for ferrihydrite. The exacerbation of the akdalaite crystal chemical oddities in the ferrihydrite model is not due to inappropriate use of the model but rather how the model is refined against the PDF data.

Future structural refinements of ferrihydrite will have to branch out from the unit cell / spherical particle treatment of PDFgui and treat the particles as a whole. At the very least, the particle morphology needs to be properly accounted for and, ideally, include surface relaxation in the model refinement and create a whole particle. Essentially deriving a unit cell for the bulk interior and treating the surface separately. Such a sophisticated model refinement can be performed using the program DISCUS, though improvements are still needed in the morphology corrections which can be derived small angle scattering data.[56-58] As software improvements continue, ultimately, the structures of nanocrystalline akdalaite and ferrihydrite need to be investigated using complex nanoparticle modelling. In order to truly resolve the structure of ferrihydrite, the whole particle approach will first need to be evaluated using nanocrystalline akdalaite for which the local structure can be verified with solid-state NMR techniques.

References

1. Hochella, M. F.; Lower, S. K.; Maurice, P. A.; Penn, R. L.; Sahai, N.; Sparks, D. L.; Twining, B. S., Nanominerals, mineral nanoparticles, and Earth systems. *Science* **2008,** 319, (5870), 1631-1635.

2. Banfield, J. F.; Zhang, H. Z., Nanoparticles in the environment. *Nanoparticles and the Environment* **2001,** 44, 1-58.

3. Squires, G. L., *Introduction to the theory of thermal neutron scattering*. Dover Publications: Mineola, N.Y., 1996; p vii, 260 p.

4. Juhas, P.; Cherba, D. M.; Duxbury, P. M.; Punch, W. F.; Billinge, S. J. L., Ab initio determination of solid-state nanostructure. *Nature* **2006,** 440, (7084), 655-658.

5. Egami, T.; Billinge, S. J. L., *Underneath the Bragg peaks : structural analysis of complex materials*. Pergamon: Kiddington, Oxford, UK ; Boston, 2003; p xviii, 404 p.

6. Young, R. A., *The Rietveld method*. International Union of Crystallograhy ;
Oxford University Press: Chester, England
Oxford ; New York, 1993; p x, 298 p.

7. Farrow, C. L.; Juhas, P.; Liu, J. W.; Bryndin, D.; Bozin, E. S.; Bloch, J.; Proffen, T.; Billinge, S. J. L., PDFfit2 and PDFgui: computer programs for studying nanostructure in crystals. *Journal of Physics-Condensed Matter* **2007,** 19, (33).

8. Jambor, J. L.; Dutrizac, J. E., Occurrence and constitution of natural and synthetic ferrihydrite, a widespread iron oxyhydroxide. *Chemical Reviews* **1998,** 98, (7), 2549-2585.

9. Drits, V. A.; Sakharov, B. A.; Salyn, A. L.; Manceau, A., Structural Model for Ferrihydrite. *Clay Minerals* **1993,** 28, (2), 185-207.

10. Michel, F. M.; Ehm, L.; Antao, S. M.; Lee, P.; Chupas, P. J.; Liu, G.; Strongin, D. R.; Schoonen, M. A. A.; Phillips, B. L.; Parise, J. B., The Structure of Ferrihydrite, a Nanocrystalline Material. *Science* **2007,** 316, 1726-1729.

11. Michel, F. M.; Barron, V.; Torrent, J.; Morales, M. P.; Serna, C. J.; Boily, J. F.; Liu, Q. S.; Ambrosini, A.; Cismasu, A. C.; Brown, G. E., Ordered ferrimagnetic form of ferrihydrite reveals links among structure, composition, and magnetism. *Proceedings of the National Academy of Sciences of the United States of America* **2010,** 107, (7), 2787-2792.

12. Manceau, A., Evaluation of the structural model for ferrihydrite derived from real-space modelling of high-energy X-ray diffraction data. *Clay Minerals* **2009,** 44, (1), 19-34.

13. Manceau, A., PDF analysis of ferrihydrite and the violation of Pauling's Principia. *Clay Minerals* **2010,** 45, (2), 225-228.

14. Manceau, A., Critical evaluation of the revised akdalaite model for ferrihydrite. *American*

Mineralogist **2011,** 96, (4), 521-533.

15. Manceau, A.; Skanthakumar, S.; Soderholm, L., PDF analysis of ferrihydrite: Critical assessment of the under-constrained akdalaite model. *American Mineralogist* **2014,** 99, (1), 102-108.

16. Xu, W. Q.; Hausner, D. B.; Harrington, R.; Lee, P. L.; Strongin, D. R.; Parise, J. B., Structural water in ferrihydrite and constraints this provides on possible structure models. *American Mineralogist* **2011,** 96, (4), 513-520.

17. Barron, V.; Torrent, J.; Michel, F. M., Critical evaluation of the revised akdalaite model for ferrihydrite-Discussion. *American Mineralogist* **2012,** 97, (1), 253-254.

18. Casey, W. H., Large aqueous aluminum hydroxide molecules. *Chemical Reviews* **2006,** 106, (1), 1-16.

19. Sadeghi, O.; Zakharov, L. N.; Nyman, M., Aqueous formation and manipulation of the iron-oxo Keggin ion. *Science* **2015,** 347, (6228), 1359-1362.

20. Harrington, R.; Neder, R. B.; Parise, J. B., The nature of x-ray scattering from geo-nanoparticles: practical considerations of the use of the Debye equation and the pair distribution function for structure analysis. *Chemical Geology* **2011,** doi:10.1016/j.chemgeo.2011.06.010.

21. Hiemstra, T., Surface and mineral structure of ferrihydrite. *Geochimica Et Cosmochimica Acta* **2013,** 105, 316-325.

22. Yamaguchi, G.; Yanagida, H.; Ono, S., A New Alumina Hydrate, Tohdite ($5Al_2O_3 \bullet H_2O$). *Bulletin of the Chemical Society of Japan* **1964,** 37, (5), 752-754.

23. Hwang, S. L.; Shen, P. Y.; Chu, H. T.; Yui, T. F., A new occurrence and new data on Akdalaite, a retrograde mineral from UHP Whiteschist, Kokchetav Massif, Northern Kazakhstan. *International Geology Review* **2006,** 48, (8), 754-764.

24. Shpanov, Y. P.; Sidorenko, G. A.; Stolyarova, T. I., Akdalaite, a new hydrated variety of alumina. *International Geology Review* **1971,** 13, (5), 675-680.

25. Tilley, D. B.; Eggleton, R. A., Tohdite ($5Al_2O_3 \bullet H_2O$) in Bauxites from Northern Australia. *Clays and Clay Minerals* **1994,** 42, (4), 485-488.

26. Novgorodova, M. I.; Mamedov, Y. G., Native Aluminum from the Mud Volcano at the Bulla Island, Caspian Sea. *Lithology and Mineral Resources* **1996,** 31, (4), 301-310.

27. Gatehouse, B. M.; Grey, I. E.; Nickel, E. H., The Crystal-Chemistry of Nolanite, (V,Fe,Ti,Al)10o14(Oh)2, from Kalgoorlie, Western-Australia. *American Mineralogist* **1983,** 68, (7-8), 833-839.

28. Hanson, A. W., The Crystal Structure of Nolanite. *Acta Crystallographica* **1958,** 11, (10), 703-709.

29. Holtstam, D.; Gatedal, K.; Soderberg, K.; Norrestam, R., Rinmanite, Zn2Sb2Mg2Fe4O14(OH)(2), a new mineral species with a nolanite-type structure from the Garpenberg Norra mine, Dalarna, Sweden. *Canadian Mineralogist* **2001,** 39, 1675-1683.

30. Yamaguchi, G.; Yanagida, H.; Ono, S., The Crystal Structure of Tohdite. *Bulletin of the Chemical Society of Japan* **1964,** 37, (10), 1555-1557.

31. Yamaguch.G; Okumiya, M., Refinement of Structure of Tohdite $5Al_2O_3 \bullet H_2O$. *Bulletin of the Chemical Society of Japan* **1969,** 42, (8), 2247-+.

32. Sterner, S. M., Precise Pressure Control in Hydrothermal Experiments with Cold-Seal Pressure-Vessels. *American Mineralogist* **1994,** 79, (11-12), 1150-1152.

33. Rosenberg, P. E., Stability relations of aluminum hydroxy-fluoride hydrate, a ralstonite-like mineral, in the system AlF3-Al2O3-H2O-HF. *Canadian Mineralogist* **2006,** 44, 125-134.

34. Furrer, G.; Phillips, B. L.; Ulrich, K. U.; Pothig, R.; Casey, W. H., The origin of aluminum flocs in polluted streams. *Science* **2002,** 297, (5590), 2245-2247.

35. Hammersley, A. P.; Svensson, S. O.; Hanfland, M.; Fitch, A. N.; Hausermann, D., Two-dimensional detector software: From real detector to idealised image or two-theta scan. *High Pressure Research* **1996,** 14, (4-6), 235-248.

36. Qiu, X.; Thompson, J. W.; Billinge, S. J. L., PDFgetX2: a GUI-driven program to obtain the pair distribution function from X-ray powder diffraction data. *Journal of Applied Crystallography* **2004,** 37, (4), 678.

37. Chupas, P. J.; Qiu, X. Y.; Hanson, J. C.; Lee, P. L.; Grey, C. P.; Billinge, S. J. L., Rapid-acquisition pair distribution function (RA-PDF) analysis. *Journal of Applied Crystallography* **2003,** 36, 1342-1347.

38. Sheldrick, G. M., A short history of SHELX. *Acta Crystallographica Section A* **2008,** 64, 112-122.

39. A. C. Larson, R. B. V. D., General Structure Analysis System (GSAS). *Los Alamos National Laboratory* **2000,** Report LAUR 86-748.

40. Toby, B. H., EXPGUI, a graphical user interface for GSAS. *Journal of Applied Crystallography* **2001,** 34, 210-213.

41. Xu, H.; Zhao, Y.; Vogel, S. C.; Daemen, L. L.; Hickmott, D. D., Anisotropic thermal expansion and hydrogen bonding behavior of portlandite: A high-temperature neutron diffraction study. *Journal of Solid State Chemistry* **2007,** 180, (4), 1519-1525.

42. Parise, J. B.; Leinenweber, K.; Weidner, D. J.; Tan, K.; Vondreele, R. B., Pressure-Induced H-Bonding - Neutron-Diffraction Study of Brucite, $Mg(OD)_2$, to 9.3 Gpa. *American Mineralogist* **1994,** 79, (1-2), 193-196.

43. Parise, J. B.; Theroux, B.; Li, R.; Loveday, J. S.; Marshall, W. G.; Klotz, S., Pressure dependence of hydrogen bonding in metal deuteroxides: a neutron powder diffraction study of $Mn(OD)_2$ and beta-$Co(OD)_2$. *Physics and Chemistry of Minerals* **1998,** 25, (2), 130-137.

44. Xue, X. Y.; Kanzaki, M., Proton Distributions and Hydrogen Bonding in Crystalline and Glassy Hydrous Silicates and Related Inorganic Materials: Insights from High-Resolution Solid-State Nuclear Magnetic Resonance Spectroscopy. *Journal of the American Ceramic Society* **2009,** 92, (12), 2803-2830.

45. Yesinowski, J. P.; Eckert, H.; Rossman, G. R., Characterization of Hydrous Species in Minerals by High-Speed H-1 Mas Nmr. *Journal of the American Chemical Society* **1988,** 110, (5), 1367-1375.

46. Brown, I. D.; Altermatt, D., Bond-Valence Parameters Obtained from a Systematic Analysis of the Inorganic Crystal-Structure Database. *Acta Crystallographica Section B-Structural Science* **1985,** 41, (Aug), 244-247.

47. Brown, I. D., Recent Developments in the Methods and Applications of the Bond Valence Model. *Chemical Reviews* **2009,** 109, (12), 6858-6919.

48. Brown, I. D., *The chemical bond in inorganic chemistry : the bond valence model*. Oxford University Press: Oxford ; New York, 2002; p x, 278 p.

49. Yu, D. Q.; Xue, D. F.; Ratajczak, H., Golden ratio and bond-valence parameters of hydrogen bonds of hydrated borates. *Journal of Molecular Structure* **2006,** 783, (1-3), 210-214.

50. Maslen, E. N.; Streltsov, V. A.; Streltsova, N. R.; Ishizawa, N., Synchrotron X-Ray Study of the Electron-Density in Alpha-Fe2o3. *Acta Crystallographica Section B-Structural Science* **1994,** 50, 435-441.

51. Pauling, L., The principles determining the structure of complex ionic crystals. *Journal of the American Chemical Society* **1929,** 51, 1010-1026.

52. Page, K.; Hood, T. C.; Proffen, T.; Neder, R. B., Building and refining complete nanoparticle structures with total scattering data. *Journal of Applied Crystallography* **2011,** 44, 327-336.

53. Parise, J. B.; Woerner, W. R.; Neder, R. B., Synchrotron powder diffraction methods and refinement techniques. In *CMS Workshop Lecture Series Volume 19: Advanced Applications of Synchrotron Radiation in Clay Science*, Waychunas, G. A., Ed. Clay Minerals Society: 2014; Vol. 19, pp 33-68.

54. Maslen, E. N.; Streltsov, V. A.; Streltsova, N. R.; Ishizawa, N.; Satow, Y., Synchrotron X-Ray Study of the Electron-Density in Alpha-Al2o3. *Acta Crystallographica Section B-Structural Science* **1993,** 49, 973-980.

55. Michel, F. M.; Ehm, L.; Liu, G.; Han, W. Q.; Antao, S. M.; Chupas, P. J.; Lee, P. L.; Knorr, K.; Eulert, H.; Kim, J.; Grey, C. P.; Celestian, A. J.; Gillow, J.; Schoonen, M. A. A.; Strongin, D.

R.; Parise, J. B., Similarities in 2-and 6-line ferrihydrite based on pair distribution function analysis of X-ray total scattering. *Chemistry of Materials* **2007,** 19, (6), 1489-1496.

56. Neder, R. B.; Proffen, T., *Diffuse Scattering and Defect Structure Simulations: a cook book using the program DISCUS*. Oxford University Press: Oxford, 2008; Vol. 11, p 228.

57. Proffen, T.; Neder, R. B., DISCUS: a program for diffuse scattering and defect-structure simulation. *Journal of Applied Crystallography* **1997,** 30, 171-175.

58. Farrow, C. L.; Billinge, S. J. L., Relationship between the atomic pair distribution function and small-angle scattering: implications for modeling of nanoparticles. *Acta Crystallographica a-Foundation and Advances* **2009,** 65, 232-239.